Universitat Autònoma de Barcelona

Structural effects on the performance of 2D metal/semiconductor contacts and RRAM devices: first-principles and molecular dynamics studies

María Laura Urquiza Toledo

Structural effects on the performance of 2D metal/semiconductor contacts and RRAM devices: first-principles and molecular dynamics studies

A thesis dissertation submitted by
María Laura Urquiza Toledo

in fullfillment of the requirements for the degree of
Doctor of Philosophy
in Electrical and Telecommunication Engineering
in the

Computational Nanoelectronics Research Group

Departament d'Enginyeria Electrònica

Supervised by Dr. Xavier Cartoixà Soler

December 2020

"I believe that we learn by practice. Whether it means to learn to dance by practicing dancing or to learn to live by practicing living, the principles are the same. In each, it is the performance of a dedicated precise set of acts, physical or intellectual, from which comes shape of achievement, a sense of one's being, a satisfaction of spirit."

Martha Graham

Abstract

During the last decades, the rapid development of fabrication technologies in the electronics industry brought transistor feature sizes down to roughly 10 nm. More recently, the advent of 2D materials, such as graphene and transition metal dichalcogenides, has opened up the possibility of new devices with outstanding properties and innovative concepts. In this context, it is clear that in order to keep promoting the development of naoelectronics, a description at the atomistc level is require to understand and tailor nanodevice properties. Computational simulations are an ideal tool to address these studies from a theoretical point of view. In particular density functional theory (DFT) and molecular dynamics (MD) techniques can be used complementarily to provide a wide description of the mechanisms operating in nanoelectronic devices, with atomic resolution.

The main focus of the work presented in this thesis is to provide atomistic insights of specific structural factors that determine electronic transport in selected information processing and storage devices (i.e., transistors and memories) for "Beyond Moore" technologies.

Finite bias transport properties of 2D MoS_2 lateral metal-semiconductor junctions were studied through non-equilibrium Green's functions calculations, aimed at contacting the 2D channel in a field effect transistor. The obtained results contributed to the understanding of the electrostatics in 2D junctions. Besides, the evaluation of different interface geometries allowed to predict the conditions that provide better contacting properties. From these studies, we contributed with an improved procedure to determine, experimentally or theoretically, emission regimes in 2D metal-semiconducting junctions.

Also, HfO_2-based RRAM cells were studied using MD simulations with an extended charge equilibration method to describe external electric fields, which

allowed to characterize the forming, reset and set processes. The analysis of the migration of oxygen ions and the change in the coordination of Hf atoms in the dielectric was used to describe the formation and dissolution of conductive filaments during the operation of the device with unprecedented detail. These studies were completed with DFT calculations of formation energies and activation barriers for the migration of oxygen vacancies, also obtained under the effect of an external electric field. In order to achieve such purpose, a novel scheme to perform calculations of slabs including a net charge and an electric field was proposed.

Finally, resistive switching phenomena in MoS_2 monolayers sandwiched between Au electrodes was studied through DFT transport calculations, with the intent to elucidate the structure responsable for the high and low resistance states.

Resumen

Durante las últimas décadas, el rápido desarrollo de las técnicas de fabricación asociadas a la industria electrónica hizo posible la reducción del tamaño característico de los transistores a aproximadamente 10 nm. Mas recientemente, el descubrimiento de los materiales 2D, tal como el grafeno y los dicalcogenuros de metales de transición, abrió la posibilidad de nuevos dispositivos con propiedades excepcionales y conceptos innovadores.

En este contexto, está claro que para seguir promoviendo el desarrollo de la nanoelectrónica, es necesario una descripción a nivel atómico de los materiales para comprender y adaptar las propiedades de los nanodispositivos. Las simulaciones computacionales son una herramienta ideal para abordar estos estudios desde un punto de vista teórico. En especial, los métodos basados en la teoría del funcional de la densidad electrónica (DFT-density functional theory) y las simulaciones de dinámica molecular, pueden utilizarse de forma complementaria para proporcionar una descripción más amplia de los mecanismos que operan en los dispositivos nanoelectrónicos con resolución atómica.

El objetivo principal del trabajo presentado en esta tesis es proporcionar una visión atomística de los factores estructurales específicos que determinan el transporte electrónico en elementos de procesado y almacenaje de información (ie, transistores y memorias) basados en tecnología “Beyond Moore”.

Las propiedades de transporte electrónico a voltaje finito, en uniones laterales metal-semiconductor en MoS_2, se estudiaron mediante funciones de Green de no equilibrio, dentro del formalismo de DFT. Los resultados obtenidos contribuyeron a comprender la electrostática en uniones 2D. Además, la evaluación de diferentes geometrías de la interfaz metal-semiconductor permitió predecir las condiciones que proporcionan mejores propiedades de contacto. Estos estudios dieron lugar al

desarrollo de un nuevo procedimiento para determinar los regímenes de emisión en uniones 2D metal-semiconductoras, experimental o teóricamente.

Por otro lado, también se estudiaron dispositivos RRAM basados en HfO_2 por medio de simulaciones de dinámica molecular (MD) implementando un método de equilibración de carga que permite describir el efecto de un campo eléctrico externo, con lo cual se pudo caracterizar el proceso de “forming”, “reset” y “set”. A través del análisis de la migración de iones de oxígeno y el cambio en la coordinación de los átomos de Hf en el dieléctrico se pudo describir la formación y disolución de filamentos conductores durante el funcionamiento del dispositivo a un nivel de detalle sin precedentes. Estos estudios fueron complementados con cálculos DFT de energías de formación y barreras de activación correspondientes a la migración de vacancias de oxígeno bajo el efecto de un campo eléctrico externo. Para obtener estos resultados, se propuso un novedoso esquema con el que es posible realizar cálculos DFT en materiales 2D, introduciendo carga neta y un campo externo.

Finalmente, el fenómeno de "resistive swithching" en celdas RRAM basadas en MoS_2 con electrodos de oro se estudió por medio de cálculos de transporte usando primeros principios, con el objetivo de dilucidar las estructuras responsables de los estados de alta y baja resistividad.

Acknowledgements

I am grateful for having this space to dedicate few words to all the people who have played an important role in shaping this work in many different ways.

First and foremost I would like to thank my supervisor Prof. Xavier Cartoixà for his patience and dedication in my scientific development during the last four years. His guidance and advice has been really inspiring to me.

Thanks to Prof. Alejandro Strachan, who supervised me during my stay at Purdue University, and his research group for their kind hospitality, I learned so much from them. I am grateful to Alejandro who helped with inspiring conversations and contributed to carry out Chapter 6.

This thesis would not have been possible without financial support, so I want to thank the Universitat Autònoma de Barcelona for the PIF program, and the Ministerio de Economía, Industria y Competitividad under grant TEC2015-67462-C2-1-R (MINECO/FEDER), the Ministerio de Ciencia, Innovación y Universidades under Grant No. RTI2018-097876-B-C21 (MCIU/AEI/FEDER, UE), and the EU Horizon2020 research and innovation program under Grants No. GrapheneCore2 785219 and GrapheneCore3 881603.

A special appreciation to my colleagues at UAB, Martí, Ferran, Marta, Devashish, Jordi, Pedro, Carlos and Alba, whom I shared office and lunch time with. Thanks for so many funny moments and for the constant support during bad days. To my closest friends with whom I have shared my studies in Argentina, Natalia, Agustin and Javier. Thanks for being present no matter the distance, and for our inspiring conversations.

A huge thanks to the wonderful friends I made during this journey, specially

Erika and Albert who were my continuous company and did not let me feel alone. To my beach volley team, thanks for their good vibes while I was writing this manuscript.

To my parents, for their love, support and encouragement. For everything you gave me, I dedicate my thesis to both of you.

Contents

Chapter 1

Introduction

Since the discovery of the transistor in 1947 [1, 2], the electronic industry has constantly worked to keep diminishing its dimensions, following the goals proposed by Moore's Law, which forecasted that the number of transistors per unit area would double every 24 months. By now, there has been a reduction of more than 6 orders of magnitude in 6 decades.

The integrated circuits, such as microprocessors and memories, available nowadays are silicon-based FinFET, fabricated with "5 nm" technology (corresponding to the 18 nm according to NTRS/ITRS and IRDS nomenclature, where the length indicates half metallic pitch) [3]. It is expected that feature scaling will reach fundamental limits of around 7-8 nm (half metal pitch) by the end of this decade. Therefore, in order to keep providing at least a functional scaling (this means that the same process is performed with an alternative technology that improves size, power, speed, or cost, without degrading any of the other features), novel materials and device architectures are being explored.

1.1 Emerging materials for memory and logical applications

The advent of graphene in 2004 [4] and related two-dimensional (2D) materials, synthesized [5] and proposed theoretically [6], opened up the possibility of fabricating 2D channel transistors, as well as the opportunity for new device concepts.

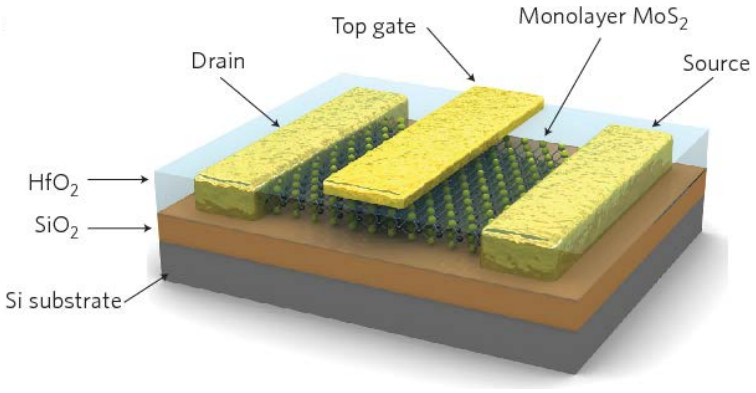

Figure 1.1: Three-dimensional schematic view of a single-layer MoS_2 transistors. Reprinted by permission from Springer, Nature Nanotechnology [10]. Copyright 2011.

Graphene has especially attracted attention because its extremely high mobility, achieving room temperature values close to 40,000 $cm^2/V{\cdot}s$ [7] on SiO_2, or above 100,000 cm^2/Vs [8] on hexagonal boron nitride (hBN). During the last fifteen years many efforts have been dedicated to fabricate graphene-channel transistors, but due to its lack of a bandgap, the ON/OFF current ratios obtained are not high enough for digital applications.

Other 2D materials of great interest for the electronic industry are transition metal dichalcogenide (TMDs). They are a family of materials with general formula MX_2, where M is a transition metal element and X is a chalcogen atom. Among them, molybdenum disulfide, MoS_2, is probably the most popular, whose single layer was isolated for electrical measurements in 2005 [9]. Although single layer MoS_2-based transistors [10] and microprocessors [11] have been successfully fabricated, these devices have still issues to overcome related to the formation of Schottky barriers at the electrodes interfaces. Figure 1.1 shows a scheme of single-layer MoS_2 transistors.

But the use of TMD is not restricted to field effect transistors, junction diodes or tunneling devices, as memristive behavior has been recently observed in their single layers sandwiched between two metallic electrodes [12].

Another material very promising for the development of "Beyond Moore" technologies is hafnium dioxide (HfO_2) that has been widely used as dielectric in MOSFETs, and during the last decade started to be used in the fabrication

of resistive random access memory (RRAM) devices, thanks to its possibility of switching between high and low resistance states. The great potential of RRAM devices is their capability of scaling down to 10 nm, leading at the same time really high switching speed, below few nanoseconds [13].

However, because of the high investment that a change in the fabrication technologies implies, the different problems that these materials face have to be solved before they will be able to replace silicon.

1.2 Why computational simulations?

In the framework of emerging devices, the most difficult challenge for "Beyond Moore" technologies is to control the properties of the materials that will enable their operation at the nanoscale. This strong experimental goal requires continuous support from theoretical modeling, since it allows reducing time and cost during a typical technology development.

Computational simulations cover a wide range of approximation levels that allow modeling materials and its electronic properties from quantum to macroscopic perspective [14]. The work presented in this thesis is based on first-principles and molecular dynamics methods. Density functional theory and extensions, such as Green's function techniques, provide a quantum description free from parameters. However, they are limited to systems with O(1,000) atoms at most, and simulation times on the order of 10^{-15} to 10^{-12} s. At the same time, with molecular dynamic techniques multi-million atom simulations are possible, for timescales from ps to ns, although it depends interatomic potentials developed for specific atomic pairs. Considering all these pros and cons, both techniques can be used complementarily to provide a more complete description of material properties and processes; this is the work performed throughout this thesis.

1.3 Outline of the thesis

The present thesis is organized as follows. Chapters 2, 3 and 4 describe the methodology used in this thesis. Starting by density functional theory and electronic transport through Green functions in Chapters 2 and 3, respectively. Then, the basics of molecular dynamics technique are presented in Chapter 4.

Chapter 5 shows quantum studies of MoS_2 lateral metal/semiconductor contacts, where transport properties of the system are studied with the Green's function formalism.

Chapter 6 includes studies of HfO_2-based RRAM cells with molecular dynamics simulations, where the operating mechanism based on the migration of oxygen ions is described. Further studies of HfO_2 structures are presented in Chapter 7, where quantum calculations of oxygen vacancy formation and migration are carried out.

Chapter 8 presents preliminary studies of MoS_2-based RRAM devices, where NEGF are used to evaluate transport properties of different structures, in order to determine the origin of resistive switching behavior in these cells.

Finally, general conclusions of the thesis are presented in Chapter 9.

Chapter 2

Density functional theory

Density functional theory (DFT) is a quantum mechanical method broadly used to calculate the electronic structure of molecules and condensed matter. It was developed in 1964 by Pierre Hohenberg and Walter Kohn [15], and the latter received the Nobel Prize in Chemistry in 1998 for his contribution to the electronic structure field [16]. DFT is based on the ground state electron density, instead of the Schrödinger wave function, to solve the quantum mechanical many body problem. The most rudimentary form of DFT is the Thomas [17] and Fermi [18] model, proposed in 1927, which expresses the kinetic energy of a homogeneous non-interacting electron gas as a functional of the electron density.

This chapter organizes as follows: it starts with an introduction of the quantum mechanical many-body problem, then the basic theory of DFT, including the Hohenberg-Kohn (HK) theorems, the Kohn-Sham (KS) single-particle equations and the most common approximations used to calculate the exchange-correlation functional. The last three sections are dedicated to discuss several important aspects related to the implementation of DFT: the periodicity of the system, the basis set commonly used to solve the KS equations and calculation of forces. For a more detailed introduction in condensed matter theory and DFT schemes see references [19, 20, 21, 22].

2.1 The quantum mechanical many-body problem

The foundation of the quantum mechanical many-body problem is the solution of the time-independent non-relativistic Schrödinger equation:

$$\hat{H} \mid \Psi(\mathbf{r}, \mathbf{R})\rangle = E \mid \Psi(\mathbf{r}, \mathbf{R})\rangle \ , \tag{2.1}$$

where the Hamiltonian ($\hat{H}$) of a general system of N electrons with positions $r_1, r_2, ..., r_N$, and M nuclei with positions $R_1, R_2, ..., R_M$ is described as:

$$\hat{H} = \hat{T}_n + \hat{T}_e + \hat{V}_{n-n} + \hat{V}_{n-e} + \hat{V}_{e-e} \tag{2.2}$$

Here $\hat{T}$ is the kinetic energy operator, $\hat{V}$ is the potential energy operator and the subscript e and n refers to the electrons and nuclei, respectively. Each term can be replaced by its definition, giving the following expression:

$$\begin{aligned} \hat{H} = &\sum_{\alpha=1}^{M} \frac{-\hbar^2}{2M_\alpha}\nabla^2 + \frac{1}{4\pi\epsilon_0}\sum_{\alpha=1}^{M}\sum_{\beta>\alpha}^{M} \frac{Z_\alpha Z_\beta e^2}{\mid \mathbf{R}_\alpha - \mathbf{R}_\beta \mid} + \sum_{i=1}^{N} \frac{-\hbar^2}{2m_i}\nabla^2 \\ &+ \frac{1}{4\pi\epsilon_0}\sum_{\alpha=1}^{M}\sum_{i=1}^{N} \frac{Z_\alpha e^2}{\mid \mathbf{R}_\alpha - \mathbf{r}_i \mid} + \frac{1}{4\pi\epsilon_0}\sum_{i=1}^{N}\sum_{j>i}^{N} \frac{e^2}{\mid \mathbf{r}_i - \mathbf{r}_j \mid} \end{aligned} \tag{2.3}$$

Note that Eq. (2.3) assumes that the nuclei are point particles, characterized only by mass and constant charge, and neglects any relativistic corrections, such as spin–orbit interaction (SOI). The SOI can be added into the formalism, if needed, at a computational cost.

The first step towards the solution of Eq. (2.3) consists of applying the Born-Oppenheimer approximation [23] and decouple the motion of nuclei and electrons. Since the nuclei are much heavier than electrons, they can be considered fixed, which implies that $\hat{T}_n$ is zero, and $\hat{V}_{n-n}$ becomes constant. With this assumption, the electronic part is calculated for fixed nuclei coordinates according to:

$$\hat{H}_e = \sum_{i=1}^{N} \frac{-\hbar^2}{2m_i}\nabla^2 + \sum_{i=1}^{N} V_{ext}(\mathbf{r}_i) + \frac{1}{4\pi\epsilon_0}\sum_{i=1}^{N}\sum_{j>i}^{N} \frac{e^2}{\mid \mathbf{r}_i - \mathbf{r}_j \mid} \ , \tag{2.4}$$

where the external potential, V_{ext}, is the attractive potential between nucleus and electrons. In order to reduce the computational cost, in DFT the external potential is normally described by a pseudopotential which accounts for the nuclei

and the inner (core) shells of electrons. This external potential might also include the effect of an external electric field.

Finally, the problem reduces to solve the Schrödinger equation for the electronic part:

$$\hat{H}_e \mid \Psi_e(\mathbf{r}, \mathbf{R})\rangle = E_e \mid \Psi_e(\mathbf{r}, \mathbf{R})\rangle \ , \tag{2.5}$$

2.2 The Hohenberg-Kohn theorems

The theorems formulated by Hohenberg and Kohn (HK) in 1964 [15] are the basis of the DFT and apply to any system of interacting particles in an external potential V_{ext}, including the problem of electrons moving around a lattice with fixed nuclei as described above.

The first HK-theorem proves that the electronic density (ρ_0) of a non-degenerate system in the ground state is uniquely determined by the external potential (V_{ext}). It also stands that this relation is injective, so V_{ext} is also uniquely determined by ρ_0. Hence, there is a one-to-one correspondence between the external potential, that determines $\hat{H}_e$, the non-degenerate ground state ($\mid \Psi_0\rangle$) resulting from solving the Schrödinger Eq. (2.5), and the associated ground state density:

$$V_{ext}(\mathbf{r}) \iff |\Psi_0\rangle \iff \rho_0(\mathbf{r}) = \langle\Psi_0|\hat{\rho}(\mathbf{r})|\Psi_0\rangle \quad . \tag{2.6}$$

Because of this correspondence, it is possible to write the ground state as a functional of the ground state density. The existence of the functional $|\Psi[\rho_0]\rangle$ leads to the statement that any ground state observable is functional of the ground state density. In particular, this is true for the ground state energy ($E[\rho_0]$).

The second HK-theorem proves that, for a non degenerate system under a particular V_{ext}, the exact ground state energy, $E[\rho_0]$, is a global minimum when $\rho(\mathbf{r})$ is the correct ground state density, $\rho_0(\mathbf{r})$:

$$E[\rho_0] = \min E[\rho] \quad \text{or} \quad E[\rho_0] < E[\rho_0'], \tag{2.7}$$

where ρ_0 denotes the correct density and ρ_0' is any other ground state density.

2.3 The Kohn-Sham equations

The HK-theorems left us the idea that it is possible to determine the ground state energy ($E_0[\rho]$) finding the correct ground state density, which can be obtained through the variational method. However, they do not give any clue of the explicit form of the functional $E_0[\rho]$.

In 1965, one year after the publication of the HK-theorems, Walter Kohn and Lu J. Sham (KS) introduced a scheme to solve the complex interacting N-particle problem in terms of N single-particle problems [16]. The idea behind this scheme consists of finding a potential for which the ground state density of the interacting system is simultaneously the ground state density of a non-interacting system, with a well known single-particle potential v_{KS}. The Hamiltonian for this auxiliary non-interacting system can be described as:

$$\hat{H}_{KS} = \hat{T}_{KS} + \hat{V}_{KS} = \sum_{i=1}^{N} -\frac{\hbar^2}{2m}\nabla_i^2 + \sum_{i=1}^{N} v_{KS}(\mathbf{r}) \tag{2.8}$$

The corresponding non-interacting N-particle states $|\Phi\rangle$ that solves the Schrödinger equation $\hat{H}_{KS}|\Phi\rangle = E|\Phi\rangle$, is a Slater determinant constructed with the orbitals φ_i, which are the solutions of the single-particle Schrödinger equation:

$$\left\{-\frac{\hbar^2}{2m}\nabla^2 + v_{KS}(\mathbf{r})\right\}\varphi_i = \epsilon_i\varphi_i \tag{2.9}$$

The resulting eigenvalues ϵ_i are assumed to be ordered as:

$$\epsilon_1 < \epsilon_2 < ... < \epsilon_N = \epsilon_F < \epsilon_{N+1} < ... \tag{2.10}$$

where the Fermi energy, denoted as ϵ_F, is the highest occupied single-particle level. Hence, the total energy (E) and the electronic density (ρ) for this non-interacting system are given by:

$$E = \sum_{i=1} \Theta_i \epsilon_i \tag{2.11}$$

$$\rho(\mathbf{r}) = \sum_{i=1} \Theta_i \mid \varphi_i(\mathbf{r}) \mid^2 \tag{2.12}$$

Where Θ_i is an occupational function, normally described with a step function. This formulation can be extended to a system at finite temperature by simply

replacing Θ_i for a Fermi distribution.

Applying the first HK theorem, the total energy of the non-interacting system in the ground state can be written as the following functional:

$$E_0^{KS}[\rho] = \langle \Phi[\rho_0] \mid \hat{T}_{KS} + \hat{V}_{KS} \mid \Phi[\rho_0] \rangle = T_{KS}[\rho_0] + \int v_{KS}(\mathbf{r})\rho_0(\mathbf{r})dr \tag{2.13}$$

where the non-interacting kinetic energy has been defined:

$$T_{KS}[\rho_0] := \langle \Phi[\rho_0] \mid \hat{T}_{KS} \mid \Phi[\rho_0] \rangle \tag{2.14}$$

Notice that $T_{KS}[\rho_0]$ is not equal to the true kinetic energy of the system.

Applying the second HK theorem, the energy can be minimized with respect to $\rho(\mathbf{r})$ using the Lagrange multipliers method under the restriction $\int \rho(\mathbf{r})d\mathbf{r} = N$:

$$\frac{\delta}{\delta\rho(\mathbf{r})}\left[E_0^{KS}[\rho] - \mu\int \rho(\mathbf{r})d\mathbf{r}\right] = 0 \tag{2.15}$$

$$\frac{\delta T_{KS}[\rho]}{\delta\rho(\mathbf{r})} + v_{KS}(\mathbf{r}) - \mu = 0 \tag{2.16}$$

Now, we can repeat the same procedure to build an energy functional for the interacting system in the ground state:

$$E_0[\rho] = T_{KS}[\rho] + E_H[\rho] + E_{ext}[\rho] + E_{xc}[\rho] \tag{2.17}$$

Here, the functional $E_H[\rho]$ is the Hartree term expressed as Coulomb integral, that consider the interaction between the N particles with density ρ, including their self-interaction energy:

$$E_H[\rho] = \frac{1}{2}\iint \frac{\rho(\mathbf{r})\rho(\mathbf{r'})}{\mid \mathbf{r} - \mathbf{r'} \mid} d\mathbf{r}d\mathbf{r'} \quad . \tag{2.18}$$

The term $E_{ext}[\rho]$ introduces the interaction between the electron density and the potential generated by the fixed nuclei or any other external potential:

$$E_{ext}[\rho] = \int v_{ext}(\mathbf{r})\rho(\mathbf{r})d\mathbf{r} \quad . \tag{2.19}$$

Finally, since for the interacting system there are exchange and beyond effects not contained in $E_H[\rho]$, we include the exchange-correlation energy functional, $E_{xc}[\rho]$,

to account for this difference and other missing terms, such as the difference between $T_{KS}[\rho]$ and the real $T[\rho]$.

Applying the second HK theorem and minimizing the energy with respect to the electronic density, using again the Euler-Lagrange method under the restriction $\int \rho(\mathbf{r})d\mathbf{r} = N$, we arrive to the following expression:

$$\frac{\delta}{\delta\rho(\mathbf{r})}\left[E_0[\rho] - \mu\int\rho(\mathbf{r})d\mathbf{r}\right] = 0 \tag{2.20}$$

$$\frac{\delta T_{KS}[\rho]}{\delta\rho(\mathbf{r})} + \int\frac{\rho(\mathbf{r}')}{\mid\mathbf{r}-\mathbf{r}'\mid}d\mathbf{r}' + v_{ext}(\mathbf{r}) + \frac{\delta E_{xc}[\rho]}{\delta\rho(\mathbf{r})} - \mu = 0 \tag{2.21}$$

$$\frac{\delta T_{KS}[\rho]}{\delta\rho(\mathbf{r})} + v_{eff}(\mathbf{r}) - \mu = 0 \tag{2.22}$$

Where the last three terms in left side were grouped in the potential v_{eff} and μ is the Lagrange undetermined multiplier. Since Eq. (2.22), for the interacting system, has the same form that Eq. (2.16), for the auxiliary non-interacting system, we deduce that their resolution must lead to the same $\rho(\mathbf{r})$ when $v_{KS} = v_{eff}$. Therefore, the ground state density of the interacting system can be obtained in terms of the single-particle orbitals φ_i according to:

$$\begin{aligned}\left\{-\frac{\hbar^2}{2m}\nabla^2 + v_{eff}(\mathbf{r})\right\}\varphi_i(\mathbf{r}) &= \epsilon_i\varphi_i(\mathbf{r}) \\ \left\{-\frac{\hbar^2}{2m}\nabla^2 + v_{ext}(\mathbf{r}) + v_H[\rho](\mathbf{r}) + v_{xc}[\rho](\mathbf{r})\right\}\varphi_i(\mathbf{r}) &= \epsilon_i\varphi_i(\mathbf{r})\end{aligned} \tag{2.23}$$

The set of the N equation expressed in (2.23)[1] are known as the Kohn-Sham (KS) equations, whose solutions $\varphi_i(\mathbf{r})$ and the corresponding eigenvalues ϵ_i have no physical meaning, but they must be solved in order to compute the ground state density, $\rho_0(\mathbf{r})$, and calculate the total energy, $E_0[\rho]$ in an iterative process.

2.4 Exchange-Correlation Energy Functional

The exchange-correlation functional is defined as:

$$E_{xc}[\rho] = \langle\Phi|\hat{T}_e|\Phi\rangle - T_{KS}[\rho] + \langle\Phi|\hat{V}_{e-e}|\Phi\rangle - E_H[\rho] \tag{2.24}$$

[1] Although $v_{xc}[\rho](\mathbf{r})$ has been written as local, it can be implicitly nonlocal.

Where $\hat{V}_{e-e}$ is the electronic interaction and $|\Phi\rangle$ is the total wave function of the non-interacting system with the same density of the interacting system, constructed as a Slater determinant of the single particle states φ_i.

The expression for exchange-correlation functional is still unknown so it has to be approximated according to a reasonable form. The simplest and most used forms are the local density approximation (LDA) and the generalized gradient approximation (GGA).

Local density approximation (LDA)

In the LDA the exchange correlation energy per particle and volume of a system with density $\rho(\mathbf{r})$ is locally approximated by the exchange correlation energy of an homogeneous electron gas (HEG) with ground state density $\rho(\mathbf{r})$:

$$E_{xc}^{LDA} = \int \epsilon_{xc}^{HEG}(\rho(\mathbf{r}))\ \rho(\mathbf{r})\ d\mathbf{r} \tag{2.25}$$

Since ϵ_{xc} depends on the local density, the main disadvantage of this method is that it has an extremely short range, and as a consequence, it usually underestimates the dissociation energies.

Generalized Gradient Approximation (GGA)

In the GGA the E_{xc} is approximated as a function that depends on the density and its gradient at each point:

$$E_{xc}^{GGA} = \int f(\rho(\mathbf{r}), \nabla\rho(\mathbf{r}))\ d\mathbf{r} \tag{2.26}$$

This approximation improves total energies, atomization energies and structural energy differences. However, it expands and makes softer bonds, this effect sometimes corrects and sometimes overcorrects the LDA predictions.

There are many forms for the function f, in this thesis the most used is the one developed by Perdew, Burke and Ernzerhof in 1996 (PBE) [24].

2.5 Forces

The base for the calculation of forces and the the equilibrium geometries in DFT is the Hellmann-Feynman theorem [25]. Considering an eigenvalue problem, where

the expectation value depends on a parameter λ:

$$\langle\ \Psi_{0,\lambda}\mid \hat{H}_\lambda \mid \Psi_{0,\lambda}\ \rangle \quad \text{with} \quad \hat{H}_\lambda \mid \Psi_{0,\lambda}\ \rangle = E_\lambda \mid \Psi_{0,\lambda}\ \rangle \quad , \tag{2.27}$$

the theorem demonstrates that the derivative of the energy with respect to the parameter λ can be expressed as the derivate of the operator $\hat{H}$, as long as the eigenstates $\mid \Psi_{0,\lambda}\rangle$ are orthogonal and normalized for all the λ values:

$$\frac{\partial E_\lambda}{\partial \lambda} = \frac{\partial}{\partial \lambda}\ \langle \Psi_{0,\lambda}|\hat{H}_\lambda|\ \Psi_{0,\lambda}\rangle \tag{2.28}$$

$$\frac{\partial E_\lambda}{\partial \lambda} = \Big\langle \frac{\partial \Psi_{0,\lambda}}{\partial \lambda}\Big|\ \hat{H}_\lambda \Big|\Psi_{0,\lambda}\Big\rangle + \Big\langle \Psi_{0,\lambda}\Big|\frac{\partial \hat{H}_\lambda}{\partial \lambda}\Big|\Psi_{0,\lambda}\Big\rangle + \Big\langle \Psi_{0,\lambda}\ \Big|\hat{H}_\lambda\Big|\frac{\partial \Psi_{0,\lambda}}{\partial \lambda}\Big\rangle \tag{2.29}$$

$$\frac{\partial E_\lambda}{\partial \lambda} = E_\lambda \frac{\partial}{\partial \lambda}\Big\langle \Psi_{0,\lambda}\ \Big|\Psi_{0,\lambda}\Big\rangle + \Big\langle \Psi_{0,\lambda}\Big|\frac{\partial \hat{H}_\lambda}{\partial \lambda}\Big|\Psi_{0,\lambda}\Big\rangle \tag{2.30}$$

$$\frac{\partial E_\lambda}{\partial \lambda} = \Big\langle \Psi_{0,\lambda}\Big|\frac{\partial \hat{H}_\lambda}{\partial \lambda}\Big|\Psi_{0,\lambda}\Big\rangle \tag{2.31}$$

If the nuclear positions ($\mathbf{R}_\alpha$) play the role of λ, one has a relation between the forces on the nuclei, and the dependence of the electronic energy with ($\mathbf{R}_\alpha$):

$$F_\alpha = \frac{\partial E}{\partial \mathbf{R}_\alpha} = \frac{\partial}{\partial \mathbf{R}_\alpha}\left(E_e[n] + \frac{1}{2}\ \sum_{\beta\neq\alpha}\ \frac{Z_\beta Z_\alpha e^2}{\mid \mathbf{R}_\alpha - \mathbf{R}_\beta\mid}\right) \tag{2.32}$$

where $E_e[n] = T_s[n] + E_H[n] + E_{ext}[n] + E_{xc}[n]$.

The electronic part is reduced to calculate the gradient of the term $\langle \Psi_0 \mid \hat{V}_{ext} \mid \Psi_0\rangle$, since this is the only therm with an explicit dependence on $\mathbf{R}_\alpha$. The derivative of E_e expressed in terms of the ground state $\rho(\mathbf{r})$ is given by:

$$\frac{\partial E_{ext}[\rho]}{\partial \mathbf{R}_\alpha} = \frac{\partial}{\partial \mathbf{R}_\alpha}\int -\ \frac{Z_\alpha e^2}{\mid \mathbf{R}_\alpha - \mathbf{r}\mid}\ \rho(\mathbf{r})\ d\mathbf{r} = \int \frac{Z_\alpha e^2(\mathbf{R}_\alpha - \mathbf{r})}{\mid \mathbf{R}_\alpha - \mathbf{r}\mid^3}\ \rho(\mathbf{r})\ d\mathbf{r} \tag{2.33}$$

On the other hand, the nuclear term gives:

$$\frac{\partial}{\partial \mathbf{R}_\alpha}\ \left(\frac{1}{2}\ \sum_{\beta\neq\alpha}\ \frac{Z_\beta Z_\alpha e^2}{\mid \mathbf{R}_\alpha - \mathbf{R}_\beta\mid}\ \right) = -\frac{1}{2}\ \sum_{\beta\neq\alpha}\ \frac{Z_\beta Z_\alpha e^2}{\mid \mathbf{R}_\alpha - \mathbf{R}_\beta\mid^3}\ (\mathbf{R}_\alpha - \mathbf{R}_\beta) \tag{2.34}$$

Finally, we arrive to the following expression for the forces:

$$\frac{\partial E}{\partial \mathbf{R}_\alpha} = \int \frac{Z_\alpha e^2(\mathbf{R}_\alpha - \mathbf{r})}{\mid \mathbf{R}_\alpha - \mathbf{r}\mid^3}\ \rho(\mathbf{r})\ d\mathbf{r} - \frac{1}{2}\ \sum_{\beta\neq\alpha}\ \frac{Z_\beta Z_\alpha e^2}{\mid \mathbf{R}_\alpha - \mathbf{R}_\beta\mid^3}\ (\mathbf{R}_\alpha - \mathbf{R}_\beta) \tag{2.35}$$

Equation (2.35) shows that the gradient of the total energy, i.e. the forces on the nuclei, are completely determined by the explicit dependence of electronic energy with R_α.

2.6 Periodicity

Considering the problem of independent electrons in a solid, the effective potential v_{eff}, used to solve the KS equations, must have the periodicity of the corresponding Bravais lattice. As a result, the eigenstates of such operator must be invariant to any translation defined as:

$$\mathbf{T}(n) = n_1\mathbf{a}_1 + n_2\mathbf{a}_2 + n_3\mathbf{a}_3 \tag{2.36}$$

where $\mathbf{a}_i$ are the lattice vectors of the primitive cell, and n_i are integers. We can also define a translation operator $\hat{\mathbf{T}}$ that act on the eigenfunction by displacing the argument according to:

$$\hat{\mathbf{T}}\varphi(\mathbf{r}) = \varphi(\mathbf{r}+\mathbf{T}) = \varphi(\mathbf{r} + n_1\mathbf{a}_1 + n_2\mathbf{a}_2 + n_3\mathbf{a}_3) \tag{2.37}$$

The Bloch theorem [26] states that for any translation $\mathbf{T}$, the eigenfunctions resulting from a one-electron Hamiltonian, such as the one described in Eq. (2.23), can be written as plane waves multiplied by a function ($\mathbf{u_k}$) with the same periodicity that the Bravais lattice:

$$\varphi_\mathbf{k}(\mathbf{r}) = e^{i\mathbf{k}\cdot\mathbf{r}}\mathbf{u_k}(\mathbf{r}) \quad , \tag{2.38}$$

with $\mathbf{u_k}(\mathbf{r}) = \mathbf{u_k}(\mathbf{r}+\mathbf{T})$ so we can write:

$$\hat{\mathbf{T}}\varphi_\mathbf{k}(\mathbf{r}) = \varphi_\mathbf{k}(\mathbf{r}+\mathbf{T}) = e^{i\mathbf{k}\cdot(\mathbf{r}+\mathbf{T})}\mathbf{u_k}(\mathbf{r}) \quad . \tag{2.39}$$

Distributing the exponential function and replacing by Eq. (2.38), we arrive to an alternative expression for the theorem:

$$\varphi_\mathbf{k}(\mathbf{r}+\mathbf{T}) = e^{i\mathbf{k}\cdot\mathbf{T}}e^{i\mathbf{k}\cdot\mathbf{r}}\mathbf{u_k}(\mathbf{r}) = e^{i\mathbf{k}\cdot\mathbf{T}}\varphi_\mathbf{k}(\mathbf{r}) \tag{2.40}$$

The reciprocal lattice vectors can be obtained imposing that $e^{i\mathbf{G}\cdot\mathbf{T}} = 1$, which gives:

$$\mathbf{G}\cdot\mathbf{T} = 2\pi m \tag{2.41}$$

$$\mathbf{G}\cdot n_i\mathbf{a}_i = 2\pi m \tag{2.42}$$

and it is found that

$$\mathbf{G} = m_1\mathbf{b}_1 + m_2\mathbf{b}_2 + m_3\mathbf{b}_3 \tag{2.43}$$

with $\mathbf{b}_i$ corresponding to the primitive vectors of the reciprocal lattice:

$$\mathbf{b}_1 = 2\pi\frac{\mathbf{a}_2 \times \mathbf{a}_3}{|\mathbf{a}_1 \cdot (\mathbf{a}_2 \times \mathbf{a}_3)|} \tag{2.44}$$

The other vectors can be derived by doing cyclical permutations.

The eigenstates ($\varphi_{\mathbf{k}}$), and their corresponding eigenvalues ($\epsilon_{\mathbf{k}}$), can be found separately for each $\mathbf{k}$ in one primitive cell of the reciprocal lattice.

2.7 Basis sets

In the practice, the Kohn–Sham single-particle equations (2.23) are solved by performing a linear expansion of the orbitals φ_i. There are three different methods that are normally used to perform such expansion: the plane wave method, the localized atomic orbitals (LCAO) method and the atomic sphere method [19]. Each approach leads to a complementary way to understand electronic structure, and each one has their advantages and disadvantages. Here, we will describe briefly the first two methods, since plane waves expansion is the base of VASP [27] code and LCAO is the base of SIESTA [28] and CP2K [29] codes, all of them used in throughout this thesis.

Plane wave method

Using Eq. (2.38), and expanding the periodic functions $\mathbf{u}_k(r)$ as Fourier series:

$$\mathbf{u}_{\mathbf{k}} = \sum_m c_m(\mathbf{k}) e^{i\mathbf{G}_m\cdot\mathbf{r}} = \sum_m c_m(\mathbf{k}) e^{i\mathbf{G}_m\cdot(\mathbf{r}+\mathbf{T})} \quad , \tag{2.45}$$

one can write the eigenfunctions as:

$$\varphi_{i,\mathbf{k}}(\mathbf{r}) = \sum_m c_m(\mathbf{k}) \times \frac{1}{\sqrt{\Omega}}\, e^{i(\mathbf{k}+\mathbf{G}_m)\cdot\mathbf{r}} \tag{2.46}$$

where Ω is the total volume of the cell, c_m are the expansion coefficients and the sum goes over all the possible reciprocal vectors:

$$\mathbf{G}_m = m_1\mathbf{b}_1 + m_2\mathbf{b}_2 + m_3\mathbf{b}_3 \tag{2.47}$$

Although the sum over m should in principle extend to infinity, one can define a cutoff energy for the plane wave that ensures the proper convergence of the DFT calculation.

One of the advantages of this basis set is that they have naturally the periodicity of the lattice, besides they are orthonormal and convergence is achieved by simply extending the cutoff energy. On the other hand, disadvantages are the volume dependence with the volume, that increaases the number of functions with the size of the cell and that, sometimes, localized functions are difficult to represent.

Localized atomic orbitals method

Alternatively, the KS orbitals (φ_i) can be linearly expanded in a series of predefined basis functions:

$$\varphi_{i,\mathbf{k}}(\mathbf{r}) = \sum_{\mu}^{N} c_\mu(\mathbf{k})\phi_{\mu,\mathbf{k}}(\mathbf{r}) \quad , \tag{2.48}$$

attached to nuclear positions, i.e: $\phi_{\mu,\mathbf{k}}(\mathbf{r}) \rightarrow \sum_{\mathbf{R}} \phi_\mu(\mathbf{r} - \mathbf{R}_i)$.

With this expansion,the KS Eq. (2.23) writes:

$$\left\{ -\frac{\hbar^2}{2m}\nabla^2 + v_{eff}(\mathbf{r}_i) \right\} \sum_{\mu}^{N} c_\mu(\mathbf{k})\phi_{\mu,\mathbf{k}}(\mathbf{r}) = \epsilon_i \sum_{\mu}^{N} c_\mu(\mathbf{k})\phi_{\mu,\mathbf{k}}(\mathbf{r}) \tag{2.49}$$

$$\hat{H}^{KS} \sum_{\mu}^{N} c_\mu(\mathbf{k})\phi_{\mu,\mathbf{k}}(\mathbf{r}) = \epsilon_i \sum_{\mu}^{N} c_\mu(\mathbf{k})\phi_{\mu,\mathbf{k}}(\mathbf{r}) \tag{2.50}$$

Multiplying from the left by an arbitrary basis function ψ_ν and integrating over space, we get N equations:

$$\sum_{\mu}^{N} c_\mu(\mathbf{k}) \int \phi^*_{\nu,\mathbf{k}}(\mathbf{r})\hat{H}^{KS}\phi_{\mu,\mathbf{k}}(\mathbf{r})d\mathbf{r} = \epsilon_i \sum_{\mu}^{N} c_\mu(\mathbf{k}) \int \phi^*_{\nu,\mathbf{k}}(\mathbf{r})\phi_{\mu,\mathbf{k}}(\mathbf{r})d\mathbf{r} \tag{2.51}$$

The integral in the left side gives the elements of the KS matrix F^{KS}:

$$F^{KS}_{\nu\mu}(\mathbf{k}) = \int \phi^*_{\nu,\mathbf{k}}(\mathbf{r})\hat{H}^{KS}\phi_{\mu,\mathbf{k}}(\mathbf{r})d\mathbf{r} \tag{2.52}$$

On the other hand, the integral in the right side is the overlap matrix, S, whose matrix elements are given by:

$$S_{\nu\mu}(\mathbf{k}) = \int \phi^*_{\nu,\mathbf{k}}(\mathbf{r})\phi_{\mu,\mathbf{k}}(\mathbf{r})d\mathbf{r} \tag{2.53}$$

Using these two definitions, Eq. (2.51) writes as:

$$\mathbf{CF}^{KS} = \epsilon \mathbf{CS} \quad , \tag{2.54}$$

which is the basis of the tight-binding method.

The basis functions ϕ can be represented as a set of numerical atomic-like functions centered on the atom sites. For each site k j, the basis functions can be written as radial functions multiplied by spherical harmonics:

$$\phi_{nlm}(\mathbf{r} - \mathbf{R}_\alpha) = \chi_{nl}(|\mathbf{r} - \mathbf{R}_\alpha|)\, Y_{lm}\left(\frac{\mathbf{r} - \mathbf{R}_\alpha}{|\mathbf{r} - \mathbf{R}_\alpha|}\right) \tag{2.55}$$

Other type of localized basis functions are the Gaussian-type-orbitals (GTOs) and the Slater-type-orbitals (STO) [19].

Chapter 3

Electronic transport

In the previous chapter we demonstrated how DFT calculations can be used to describe the electronic structure of systems in equilibrium, such as molecules, atomic clusters or infinite periodic solids. In all these cases, the dimension of the problem is finite, i.e. there is a finite number of Kohn-Sham equations to solve. However, if we are interested in describing the electronic structure and transport properties of systems out of equilibrium, where an external potential is applied and a current is flowing, these equations cannot be used.

This chapter is dedicated to introducing the formalism used to perform ballistic transport calculations. It starts with the description of the Landauer formula, which expresses the conductance of a quantum system as a scattering problem. Then, we will briefly describe the Green's functions formalism, which is the basis to compute the charge density in a non-equilibrium condition. Finally, we will show how combining DFT with the Green's function techniques one can obtain the transport properties of a system.

3.1 Conductance from the Landauer Formula

In macroscopic systems not far from equilibrium, the electrical current flowing through a conductor can be calculated through Ohm's law, where the current is proportional to the applied voltage. The constant that relate the current with the voltage is the conductance:

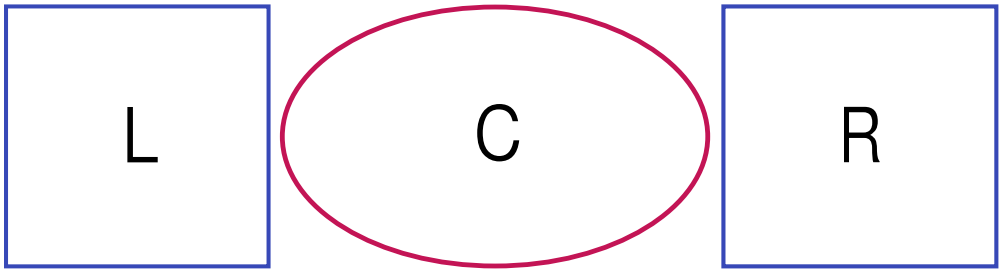

Figure 3.1: Transport setup, where the system is divided into three parts: a central region C, where the scattering events occurs, and the two semi-infinite electrodes, L and R.

$$G = \frac{\sigma A}{L}, \tag{3.1}$$

where σ represents the conductivity of the material, L the length of the conductor and A is its cross section area.

When the size of the system reduces, and W is about the size of the Fermi wavelenght (λ_F), quantum effects arise and Eq. (3.1) is not valid any more. In such conditions, the conductance can be calculated through the Landauer formula [30]:

$$G = \frac{2e^2}{h} M(E)T(E), \tag{3.2}$$

where $T(E)$ represents the average probability that an electron will be transmitted and $M(E)$ is the number of transverse modes (related to the conductor width). If the transmission of a single mode is perfect, the transmission probability will be 1, and it will contribute exactly one quantum unit of conductance, $G_0 = 2e^2/h$. Here, the factor 2 accounts for the spin degeneracy.

Considering the situation shown in Figure 3.1, where a nanoscaled sample (scattering region) is connected to one or more semi-infinite electrodes, that act as ideal electron reservoirs injecting current and fixing potential, we can use the scattering approach to relate the transport properties to the transmission and reflection probabilities for carriers incident on the sample. Using this framework, the total current $I(V) = I_{L\longrightarrow R} - I_{R\longrightarrow L}$ can be calculated as:

$$I = \frac{2e}{h} \int_{-\infty}^{\infty} T(E)[f_L(E) - f_R(E)]\, dE \tag{3.3}$$

where $f_L(E)$ and $f_R(E)$ are the Fermi distribution of the left and right electrodes, respectively.

Therefore, the Landauer formalism tell us that in order to obtain current vs. voltage characteristics, we need to calculate the transmission coefficients of the system. This can be done by using Green's functions technique applied to tight-binding Hamiltonian.

3.2 Equilibrium Green's functions

In this section we will briefly review Green's function theory, we will start defining the single particle Green's function for a system in equilibrium. Then, the bulk Green's functions will be derived by including a single-particle perturbation. Finally, will see how to apply the Green's functions to tight binding Hamiltonian, in particular when the Hamiltonian is obtained from DFT calculations. A complete description of this topic can be found in Ref. [31] and [32].

3.2.1 Single particle Green's function

Consider the problem of an electron in a one dimensional system under an external potential $V(x)$, described by the Srödinger equation $\hat{H}|\Psi\rangle = E|\Psi\rangle$, the single-particle Green's function for this system is defined as:

$$[E - \hat{H}(x)]G(x, x') = \delta(x - x') \ , \tag{3.4}$$

where

$$\hat{G} = \left[E - \hat{V}(x) + \frac{\hbar^2}{2m}\frac{\partial^2}{\partial x^2}\right]^{-1} \tag{3.5}$$

One can understand the Green's functions $G(x, x')$ as the wavefunction amplitude of an electron traveling with energy E from the position x' to x. In the case of a constant potential $\hat{V}(x) = U_0$, the problem can be solved exactly finding two solutions:

$$\begin{aligned} G^R(E, x - x') &= -\mathrm{i}\ \frac{m}{\hbar^2 k}\ e^{\mathrm{i}k|x-x'|} \\ G^A(E, x - x') &= \mathrm{i}\ \frac{m}{\hbar^2 k}\ e^{-\mathrm{i}k|x-x'|} \end{aligned} \tag{3.6}$$

where $k = 2m\sqrt{E - U_0}/\hbar$. This equation is valid for all x values, except when $x = x'$.

The solution $G^R(x,x')$ corresponds to a wave that originates at the point of excitation x', traveling to the right $(x-x'>0)$ or to the left $(x-x'<0)$. On the other hand, $G^A(x,x')$ is the time-reserved solution, corresponding to incoming waves (from left or right) that disappear at the point of excitation. Both solutions satisfy the same equation, but they correspond to different boundary conditions. It is possible to include the boundary conditions implicitly in Eq. (3.4) by introducing an infinitesimal imaginary part in the energy, thus, we would have:

$$\begin{aligned}\lim_{\eta\to 0}\ [E+i\eta-\hat{H}(x)]G^R(x,x') &= \delta(x-x')\\ \lim_{\eta\to 0}\ [E-i\eta-\hat{H}(x)]G^A(x,x') &= \delta(x-x')\end{aligned} \tag{3.7}$$

This definition can be generalized to any three dimensional problem, which will give the retarded and advanced single-particle Green's function, expressed in the matricial form:

$$\lim_{\eta\to 0}\ [(E\pm i\eta)\mathbf{I}-\mathbf{H}]\ \mathbf{G}^{R/A}(E)=\mathbf{I} \tag{3.8}$$

where $\mathbf{I}$ is the identity matrix, and $\mathbf{H}$ has been generalized to a three dimensional problem. Note that $\mathbf{G}^{R/A}$ has been written as an operator, independent of the representation.

Considering $\mathbf{H}|\psi_i\rangle=\epsilon_i|\psi_i\rangle$, and using the relation $\sum_i|\psi_i\rangle\langle\psi_i|=\mathbf{I}$, It is possible to rewrite the Eq. (3.8) in terms of the eigenvalues ϵ_i.

$$\mathbf{G}^{R/A}(E)=\sum_i\frac{|\psi_i\rangle\langle\psi_i|}{E\pm i\eta-\epsilon_i} \tag{3.9}$$

This definition can be used to derive an expression for the local density of states (LDOS): $\rho(\mathbf{r},E)=\sum_i|\langle\mathbf{r}|\psi_i\rangle|^2\ \delta(E-\epsilon_i)$. Sandwiching (3.9) by $\langle\mathbf{r}|\ldots|\mathbf{r}\rangle$:

$$\mathbf{G}^{R/A}(E)=\sum_i\frac{\langle\mathbf{r}|\psi_i\rangle\langle\psi_i|\mathbf{r}\rangle}{E\pm i\eta-\epsilon_i} \tag{3.10}$$

$$=\sum_i\frac{|\langle\mathbf{r}|\psi_i\rangle|^2}{E\pm i\eta-\epsilon_i} \tag{3.11}$$

Using the relation $[E - \epsilon_i \pm i\eta]^{-1} = P\,\frac{1}{E-\epsilon_i} \mp i\pi\delta(E-\epsilon_i)$, where P is the Cauchy principal value for contour integrals, the Green's function can be written as:

$$\mathbf{G}^{R/A}(E) = \sum_i |\langle \mathbf{r}|\psi_i\rangle|^2 \left[P\,\frac{1}{E-\epsilon_i} \mp i\pi\delta(E-\epsilon_i)\right] \tag{3.12}$$

Taking the imaginary part of $\mathbf{G}^{R/A}(E)$:

$$\mathrm{Im}\{\mathbf{G}^{R/A}(E)\} = \mp\pi \sum_i |\langle \mathbf{r}|\psi_i\rangle|^2 \delta(E-\epsilon_i)\ , \tag{3.13}$$

we finally arrive to:

$$\rho(\mathbf{r}, E) = \sum_i |\langle \mathbf{r}|\psi_i\rangle|^2\ \delta(E-\epsilon_i) = \mp\frac{1}{\pi}\,\mathrm{Im}\{\mathbf{G}^{R/A}(E)\} \tag{3.14}$$

If we use a discrete basis of atomic orbitals, the LDOS writes:

$$\rho(\mathbf{r}, E) = \mp\frac{1}{\pi}\,\mathrm{Im}\{\mathbf{G}^{R/A}_{ii}(E)\} \tag{3.15}$$

where i indicates that the density of states has been projected onto the atom i. From here, we can also calculate the density of states (DOS) by summing over all the atomic sites i:

$$\rho(E) = \sum_{i=1}^{N} \mp\frac{1}{\pi}\,\mathrm{Im}\{\mathbf{G}^{R/A}_{ii}(E)\} = \mp\frac{1}{\pi}\,\mathrm{Tr}[\mathrm{Im}\{\mathbf{G}^{R/A}(E)\}] \tag{3.16}$$

with N equal to the total number of orbitals. Note that integrating the DOS in the full energy spectrum will always give a normalized quantity, N, as can be inferred from the identity $\sum_i |\psi_i\rangle\langle\psi_i| = \mathbf{I}$. The total occupied orbitals can be obtained by integrating a product of the Fermi function, $f(E)$, and the density of states, $\rho(E)$.

3.2.2 Bulk Green's function

Consider now the problem of an infinite system, the Green's function derived in Eq. (3.8) can't be evaluated explicitly because it would imply inverting an infinite matrix. A possible solution to this issue consists in describing the Hamiltonian as:

$$\mathbf{H} = \mathbf{H}_0 + \mathbf{V} \tag{3.17}$$

where $\mathbf{H}_0$ is an unperturbed Hamiltonian whose single-particle Green's functions are known, and $\mathbf{V}$ is a single-particle perturbation. The corresponding perturbed ($\mathbf{G}^{R/A}$) and unperturbed Green's functions ($\mathbf{g}^{R/A}$) will be:

$$\mathbf{G}(E) = [(E \pm i\eta)\mathbf{I} - \mathbf{H}_0 - \mathbf{V}]^{-1} \tag{3.18}$$

$$\mathbf{g}(E) = [(E \pm i\eta)\mathbf{I} - \mathbf{H}_0]^{-1} \tag{3.19}$$

Here, for practicality, we have dropped the superindex R/A. The objective is to express the Green's function of the whole system in terms of the unperturbed Green's function:

$$[(E \pm i\eta)\mathbf{I} - \mathbf{H}_0 - \mathbf{V}]\mathbf{G}(E) = \mathbf{I} \tag{3.20}$$

$$[(E \pm i\eta)\mathbf{I} - \mathbf{H}_0]\mathbf{G}(E) - \mathbf{V}\mathbf{G}(E) = \mathbf{I} \tag{3.21}$$

$$[(E \pm i\eta)\mathbf{I} - \mathbf{H}_0]\mathbf{G}(E) = \mathbf{I} + \mathbf{V}\mathbf{G} \tag{3.22}$$

$$\mathbf{G}(E) = \mathbf{g}(E) + \mathbf{g}(E)\mathbf{V}\mathbf{G}(E) \tag{3.23}$$

where Eq. (3.23), known as Dyson's equation, is used to calculate the Green's function.

Application to tight-binding Hamiltonian

The objective now is to demonstrate how the Dyson's equation can be used to calculate Green's function for a tight-binding Hamiltonian. Consider the problem of a semi-infinite atomic chain with coupling only between nearest neighbors. The corresponding tight-binding Hamiltonian will be:

$$\mathbf{H} = \begin{bmatrix} \epsilon & t & 0 \\ t & \epsilon & \ddots \\ 0 & \ddots & \ddots \end{bmatrix} \tag{3.24}$$

To solve the problem, the first step consists of choosing the unperturbed and the corresponding perturbation. One could define the unperturbed system as the atomic chain and the interaction between atoms as the perturbation, but this would lead an infinite algebraic system. To avoid this problem, there is an alternative way that consists of splitting the chain into the first atom, placed at

the beginning of the chain, and the rest of chain. Therefore, the perturbation will be defined as the coupling between these two systems.

$$\mathbf{H}_0 = \begin{bmatrix} \mathbf{H}_{11} & 0 \\ 0 & \mathbf{H}_{22} \end{bmatrix} \quad \mathbf{V} = \begin{bmatrix} 0 & V_{12} \\ V_{21} & 0 \end{bmatrix} \tag{3.25}$$

where $\mathbf{H}_{11} = \epsilon$, $\mathbf{H}_{22} = \mathbf{H}$, because removing an atom doesn't change the fact that the chain is still semi-infinite, and $V_{12} = V_{21} = t$, because we consider coupling only between first neighbors. With this selection, the unperturbed Green's function will be:

$$\mathbf{g}(E) = \begin{bmatrix} g_{11} & 0 \\ 0 & g_{22} \end{bmatrix} \tag{3.26}$$

where $g_{11} = [E \pm i\eta - \epsilon]^{-1}$, and g_{22} is nothing but the Green's function of the whole chain $\mathbf{G}$. The perturbed Green's function obtained from the matrix product in the Dyson's equation (3.23) is:

$$\mathbf{G} = \begin{bmatrix} g_{11} + g_{11}V_{12}G_{21} & g_{11}V_{12}G_{22} \\ g_{22}V_{21}G_{11} & g_{22} + g_{22}V_{21}G_{12} \end{bmatrix} \tag{3.27}$$

Suppose we want to calculate the perturbed Green's function G_{11}, corresponding to the first atom in the chain:

$$G_{11}(E) = g_{11}(E) + g_{11}(E)V_{12}G_{21}(E) \tag{3.28}$$

Replacing G_{21} by the result obtained in Eq. (3.27) :

$$G_{11}(E) = g_{11}(E) + g_{11}(E)V_{12}g_{22}(E)V_{21}G_{11}(E) \tag{3.29}$$

Now, we can define the self-energy as $\Sigma_{11}(E) = V_{12}g_{22}(E)V_{21} = t^2 g_{22}(E)$, which describes how the properties of the atom 1 are modified via the interaction with the second atom.

$$G_{11}(E) = g_{11}(E) + g_{11}(E)\Sigma_{11}(E)G_{11}(E) \tag{3.30}$$

$$G_{11}(E) - g_{11}(E)\Sigma_{11}(E)G_{11}(E) = g_{11}(E) \tag{3.31}$$

$$G_{11}(E) = g_{11}(E)[1 - g_{11}(E)\Sigma_{11}(E)]^{-1} \tag{3.32}$$

$$G_{11}(E) = [1/g_{11}(E) - \Sigma_{11}(E)]^{-1} \tag{3.33}$$

$$G_{11}(E) = [E \pm i\eta - \epsilon - \Sigma_{11}(E)]^{-1} \tag{3.34}$$

From Eq. (3.34) we can extract a couple of conclusions about the self-energy i) its real part can be understood as a re-normalization of the energy ($\tilde{\epsilon} = \epsilon - \mathrm{Re}\{\Sigma_{11}(E)\}$) due to presence of the chain, ii) its imaginary part describes the broadening of the energy due to the interaction between the particle 1 and the rest of the chain. This equation also shows that the solution of an infinite system defined as a finite system under an external perturbation, can be solved using a one-particle basis and the self energy of the perturbation. Of course we still have to calculate the self energies of an infinite system.

Non-orthogonal basis set

The equations described above can be generalized for non-orthogonal basis set, such as the localized orbitals centered in different atoms. In this case, instead of the identity matrix ($\mathbf{I}$), we will have an overlap matrix ($\mathbf{S}$), whose matrix elements are calculated as:

$$\mathbf{S}_{ij} = \langle \phi_i | \phi_j \rangle \tag{3.35}$$

The corresponding single particle Green's function will be:

$$\mathbf{G}^{R/A} = [(E \pm i\eta)\mathbf{S} - \mathbf{H}]^{-1} \tag{3.36}$$

3.3 Combining DFT with Green's functions

In the first section it was shown that the current through a microscopic conductor can be calculated using the Landauer formula, which only requires the transmission coefficients of the conductor. The aim of this section is to show how combining Green's function techniques with DFT, it is possible to describe the electronic properties and transmission coefficients of an open quantum system in a non-equilibrium situation.

To perform electronic transport with NEGF, the system must be separated into a scattering region and two (or more) semi-infinite electrodes, as shown in Figure 3.1. For simplicity, the equation will be derived for two electrodes, and then generalized for the case of N electrodes.

Using the same scheme performed in section 3.2.2, the Hamiltonian of the whole system can be described in terms of the unperturbed Hamiltonian of the

three regions and the perturbation caused by the interaction between them:

$$\mathbf{H} = \mathbf{H}_0 + \mathbf{V} = \begin{bmatrix} \mathbf{H}_L & \mathbf{V}_{LC} & 0 \\ \mathbf{V}_{CL}^{\dagger} & \mathbf{H}_C & \mathbf{V}_{CR}^{\dagger} \\ 0 & \mathbf{V}_{RC} & \mathbf{H}_R \end{bmatrix} \tag{3.37}$$

The retarded/advanced Green's function of the central, $\mathbf{G}(E)$, part can be calculated through the Dyson's equation:

$$\mathbf{G}^{R/A}(E) = [(E \pm i\eta)\mathbf{S}_C - \mathbf{H}_C - \Sigma_L(E) - \Sigma_R(E)]^{-1} \tag{3.38}$$

where $\mathbf{S}_C$ is the overlap matrix of the central part and $\Sigma(E)$ are the electrode self-energies defined previously:

$$\Sigma_L^{R/A}(E) = \mathbf{V}_L \mathbf{g}_L^{R/A}(E)\mathbf{V}_L^{\dagger} \quad \text{and} \quad \Sigma_R^{R/A}(E) = \mathbf{V}_R \mathbf{g}_R^{R/A}(E)\mathbf{V}_R^{\dagger} \tag{3.39}$$

Here, we used $\mathbf{V}_L \equiv \mathbf{V}_{LC} = \mathbf{V}_{CL}^{\dagger}$ and $\mathbf{V}_R \equiv \mathbf{V}_{RC} = \mathbf{V}_{CR}^{\dagger}$. The unperturbed Green's function of the left and right electrodes are given by:

$$\mathbf{g}_{L/R}^{R/A}(E) = [(E \pm i\eta)\mathbf{S}_{L/R} + \mathbf{H}_{L/R}]^{-1} = \sum_{l/r} \frac{|\psi_{l/r}^0\rangle\langle\psi_{l/r}^0|}{E \pm i\eta - \epsilon_{l/r}} \tag{3.40}$$

where the index l/r runs over all the states in the left/right electrode, and $|\psi^0\rangle$ are the unperturbed eigenstates.

As it was seen in the previous chapter, in section 2.7, within the LCAO approach the states can be expressed in terms of the atomic orbitals : $|\psi_{l/r}\rangle = \sum_\mu c_{\mu,l/r}|\phi_\mu\rangle$, so the unperturbed Green's functions can be referred to the local basis functions μ and ν:

$$\{\mathbf{g}_{L/R}^{R/A}(E)\}_{\mu\nu} = \sum_{l/r} \frac{c_{\mu,l/r}^0 c_{\nu,l/r}^{0\,*}}{E \pm i\eta - \epsilon_{l/r}} \tag{3.41}$$

Note that during the division of the system we assume that the electrodes are not perturbed by the central part. Therefore, the unperturbed Hamiltonian of the electrodes, $\mathbf{H}_{L/R}$, and their corresponding Green's function, $\mathbf{g}_{L/R}^{r,a}$, can be obtained from a separate bulk-like calculation. This assumption implies that the potential at the electrodes must be equal to their bulk potential. In the practice, this requirement defines the size of the central part, and depends on the screening capability of the electrodes.

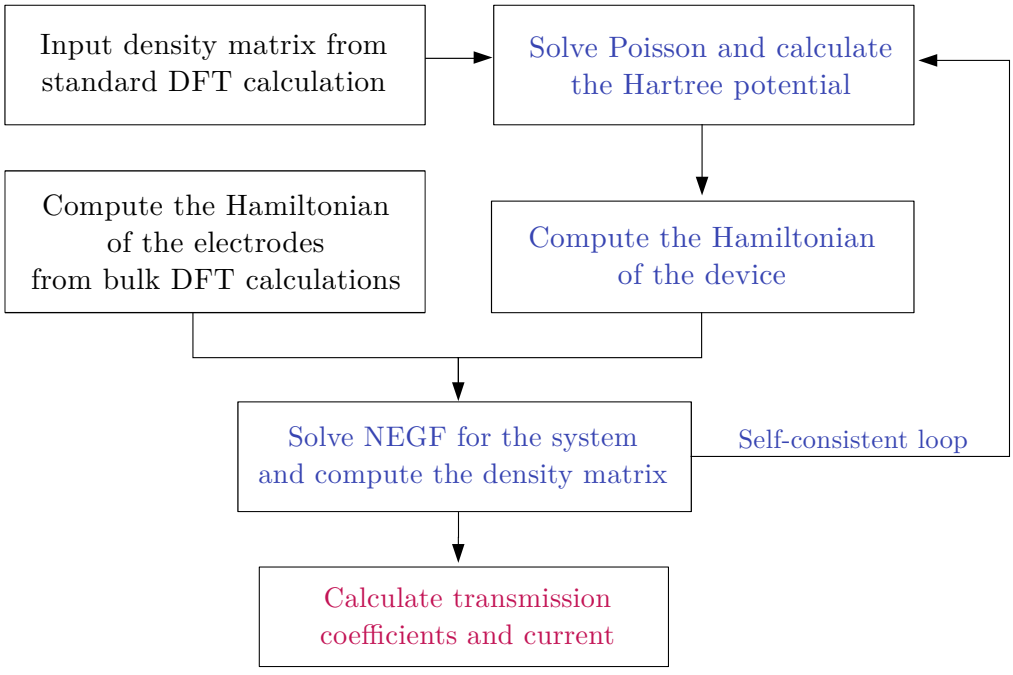

Figure 3.2: Flowchart of the self-consistent scheme used to calculate the electronic density and the transport properties from NEGF. The process in black can be performed with conventional DFT calculations, as explained in Chapter 2, while the ones in blue must be done using NEGF formalism. The output of NEGF calculations are written in purplish red.

Finally, the problem reduces to obtain a self-consistent description for the electronic density and the Kohn-Sham Hamiltonian of a scattering region coupled to two (or more) semi-infinite electrodes. The complete process is described in Figure 3.2.

3.3.1 Density matrix from Green's functions

The density matrix in the scattering region can be calculated from the incoming states of the left and right electrodes, filled up to their corresponding electrochemical potential:

$$\rho(E) = \sum_l |\psi_l\rangle\langle\psi_l| f(\epsilon_l - \mu_l) + \sum_r |\psi_r\rangle\langle\psi_r| f(\epsilon_r - \mu_r) \tag{3.42}$$

where the perturbed left/right states ($|\psi_{l/r}\rangle$) can be expressed in term of the unperturbed states according to:

$$|\psi_{l/r}\rangle = |\psi^0_{l/r}\rangle + \mathbf{G}\mathbf{V}_{L/R}\ |\psi^0_{l/r}\rangle \quad . \tag{3.43}$$

Here, for simplicity reasons, we have dropped the explicit energy dependence of the Green's function.

Similarly, the elements of the density matrix can be calculated from the scattering coefficients:

$$\rho_{\mu\nu} = \sum_l c_{\mu,l} c^*_{\nu,l}\ f(\epsilon_l - \mu_l) + \sum_r c_{\mu,r} c^*_{\nu,r}\ f(\epsilon_r - \mu_r) \tag{3.44}$$

with the perturbed coefficients calculated as:

$$c_{\mu,l/r} = c^0_{\mu,l/r} + (\mathbf{G}\mathbf{V}_{L/R})_{\mu\nu}\ c^0_{\nu,l/r} = (\mathbf{G}\mathbf{V}_{L/R})_{\mu\nu}\ c^0_{\nu,l/r} \quad , \tag{3.45}$$

since unperturbed coefficients $c^0_{\mu,l/r}$ vanish in the scattering region because they are purely electrode states.

Now, we will introduce the spectral density of the electrodes, $A_{l/r}$, whose matrix elements are calculated as:

$$\begin{aligned} A_{\mu\nu,l/r} &= \sum_{l/r} c_{\mu,l/r} c^*_{\mu,l/r}\ \delta(E - \epsilon_{l/r}) \\ A_{\mu\nu,l/r} &= \sum_{l/r} (\mathbf{G}\mathbf{V}_{L/R})_{\mu\nu}\ c^0_{\mu\nu} c^{0\ *}_{\mu,l/r}\ (\mathbf{V}^\dagger_{L/R}\mathbf{G}^\dagger)_{\mu\nu}\ \delta(E - \epsilon_{l/r}) \end{aligned} \tag{3.46}$$

Using the relation that we already know: $\frac{1}{E \pm i\eta - \epsilon_{l/r}} = P\frac{1}{E - \epsilon_{l/r}} \mp i\pi\delta(E - \epsilon_{l/r})$, and the Eq. (3.41) for the unperturbed Green's function, we arrive to:

$$A_{\mu\nu,l/r} = \left\{ \mathbf{G}\mathbf{V}_{L/R} \frac{\mathrm{Im}[\mathbf{g}_{L/R} - \mathbf{g}^\dagger_{L/R}]}{-2i\pi} \mathbf{V}^\dagger_{L/R}\mathbf{G}^\dagger \right\}_{\mu\nu} \tag{3.47}$$

$$A_{\mu\nu,l/r} = \left\{ \mathbf{G}\ \frac{i\left[\Sigma_{L/R} - \Sigma^\dagger_{L/R}\right]}{2\pi}\ \mathbf{G}^\dagger \right\}_{\mu\nu} \tag{3.48}$$

$$A_{\mu\nu,l/r} = \frac{1}{\pi}\left\{ \mathbf{G}\Gamma_{L/R}\mathbf{G}^\dagger \right\}_{\mu\nu} \tag{3.49}$$

Where it was defined the broadening matrix $\Gamma = i[\Sigma - \Sigma^\dagger]/2$. Using the spectral function, the density matrix can be expressed as:

$$\rho = \int_{-\infty}^{\infty} dE \, \Big[A_l(E) \; f(E - \mu_l) + A_r(E) \; f(E - \mu_r) \Big] \tag{3.50}$$

$$\rho = \frac{1}{\pi} \int_{-\infty}^{\infty} dE \, [\mathbf{G}\Gamma_L \mathbf{G}^\dagger f(E - \mu_l) + \mathbf{G}\Gamma_R \mathbf{G}^\dagger f(E - \mu_r)] \tag{3.51}$$

For a general case with N electrodes (e), the density matrix writes:

$$\rho = \frac{1}{\pi} \int_{-\infty}^{\infty} dE \; \sum_{e}^{N_e} \mathbf{G}\Gamma_e \mathbf{G}^\dagger f(E - \mu_e) \tag{3.52}$$

Equilibrium density

In the case that the system is in equilibrium, and all chemical potentials are equal, Eq. (3.52) rewrites:

$$\rho = \frac{1}{\pi} \int_{-\infty}^{\infty} dE \sum_{e}^{N_e} \mathbf{G}\Gamma_e \mathbf{G}^\dagger \; f(E) \tag{3.53}$$

$$\rho = \frac{i}{2\pi} \int_{-\infty}^{\infty} dE \; \mathbf{G}[\Sigma_e - \Sigma_e^\dagger]\mathbf{G}^\dagger \; f(E) \tag{3.54}$$

Isolating the self energies from Eq. (3.38), we arrive to the following expression:

$$\rho = \frac{i}{2\pi} \int_{-\infty}^{\infty} dE \; \mathbf{G}[-(\mathbf{G})^{-1} + (\mathbf{G}^\dagger)^{-1} + 2i\eta\mathbf{S}]\mathbf{G}^\dagger \; f(E) \tag{3.55}$$

$$\rho = \frac{i}{2\pi} \int_{-\infty}^{\infty} dE \; [-\mathbf{G}^\dagger + \mathbf{G} + 2i\eta\mathbf{G}\mathbf{S}\mathbf{G}^\dagger] \; f(E) \tag{3.56}$$

Considering that $\eta \to 0$, we rewrite:

$$\rho = \frac{i}{2\pi} \int_{-\infty}^{\infty} dE \; [\mathbf{G} - \mathbf{G}^\dagger] f(E) \tag{3.57}$$

For the Γ point, we have $i[\mathbf{G} - \mathbf{G}^\dagger] = -2\,\mathrm{Im}\,\mathbf{G}$ and the equilibrium density reduces to:

$$\rho = -\frac{1}{\pi} \int_{-\infty}^{\infty} dE \; \mathrm{Im}[\mathbf{G}] f(E) \quad , \tag{3.58}$$

which is the expression obtained in Eq. (3.14).

3.3.2 Calculation of transmission coefficients

The transmission functions can be calculated using the scattering formalism through the Fisher-Lee relation [33], where the scattering elements are calculated as:

$$s_{ee'} = -\delta_{ee'} + i\Gamma_e^{1/2}(E)\mathbf{G}(E)\Gamma_{e'}^{1/2}(E) \tag{3.59}$$

Hence, the transmission coefficients from electrode e to e' is given by:

$$T(E) = \mathrm{Tr}[s_{ee'}s_{ee'}^{\dagger}] \qquad \text{with} \quad e \neq e' \tag{3.60}$$

$$T(E) = \mathrm{Tr}[\Gamma_e(E)\mathbf{G}(E)\Gamma_{e'}(E)\mathbf{G}^{\dagger}(E)] \tag{3.61}$$

Chapter 4

Molecular dynamics

Density functional theory calculations, explained in Chapter 2, are widely used to obtain equilibrium structures and energies of molecules and solids. However, as they come at the expense of a high computational cost, they are restricted to systems with few thousands of atoms. Molecular dynamics (MD) is a classical technique used to compute thermodynamics and dynamic properties of large-scale atomistic systems (in the range of 10^6 to 10^9 atoms, depending on the force field used) with significantly reduced computational cost.

This method integrates Newton's equations of motion to determine the system evolution in time, where the forces are calculated from interatomic potentials, often referred to as force fields. The result of a MD simulation is a set of atomic positions and velocities for each timestep, which can be transformed into macroscopic information (temperature, internal energy, pressure, etc.) using statistical mechanics. Figure 4.1 shows a schematic describing the fundamental loop that allows time evolution in a molecular dynamics simulation.

This chapter describes general aspects of the MD, starting with the description of the force field used in the thesis, then the explanation of the most common integration algorithms for the equations of motion, and finally, the basic statistical ensemble concepts that relate the microscopic information with macroscopic properties of interest.

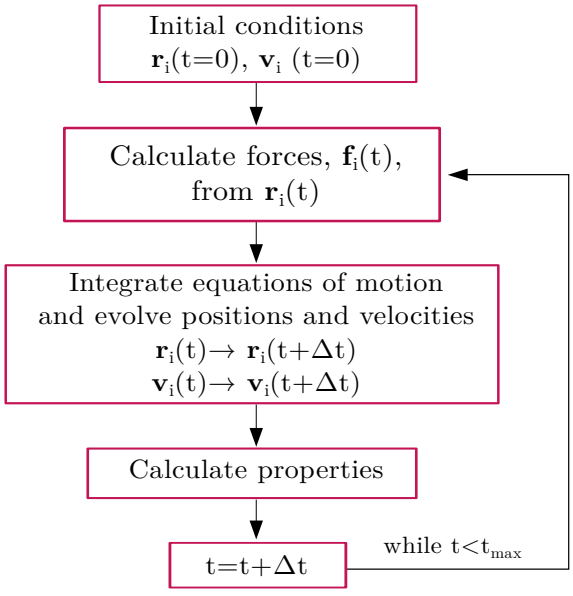

Figure 4.1: Description of the standard molecular dynamics simulation algorithm.

4.1 Force fields

The force field is the core of a MD simulation, because it defines how the particles interact each other. Force field parameters are usually estimated from experimental data or quantum mechanics calculations, and optimized to reproduce materials properties.

Pair potentials, such as Lennard-Jones [34] or Buckingham [35, 36, 37], describe all bonds between the same atomic pair equally, and can be used to study systems near equilibrium with fixed properties. Although these potentials are computationally cheap, they have limited transferability, i.e. the parameters determined for specific types of crystals (or molecules) can not be used to describe range of crystal structures. As result, they are not suitable for the study of chemical reactions where the materials modify their reactivity and charges during the simulation.

On the other hand, many-body force fields normally introduce the concept of bond order (BO), that depends on the local chemical environment, to describe different bonding states of an atom. Hence, they are much more transferable

and can be used to study formation and dissociation of chemical bonds. Some examples are REBO [38], Tersoff [39, 40], COMB [41] and ReaxFF [42]. Besides the use of BO to describe covalent interactions [], some potentials, such as COMB and ReaxFF, also include charge equilibration schemes [] to evolve the atomic charges according the local environment at each step of the simulation.

In this thesis, we perform MD simulations to study resistive switching process in HfO_2-based memories, that occurs through a redox mechanism. We have chosen the ReaxFF because it allows us to reproduce chemical reactions under the effect of an external potential thanks to the addition of electrochemical dynamics with implicit degrees of freedom (EChemDID) [43].

ReaxFF

The general formula of ReaxFF [42] counts the following therms in the force calculation:

$$E_{system} = E_{bond} + E_{over} + E_{angle} + E_{tors} + E_{vdw} + E_{coul} \tag{4.1}$$

Where E_{bond} is a function of the interatomic distance that describes the energy associated with the formation of bonds between atoms. E_{angle} and E_{tors} are three and four-body energy therms, associated to the valence angle strain and torsional angle strain, respectively. E_{over} is an energy penalty that prevents the over coordination of atoms. E_{coul} and E_{vdw} are Coulomb and Van deer Waals therms, respectively. A detailed explanation of each energy therm can be found in Ref. [42].

The bond order (BO'_{ij}) between two atoms i, j is calculated from the interatomic distance (r_{ij}) according to the following empirical equation:

$$\begin{aligned} BO' &= BO^{\sigma}_{ij} + BO^{\pi}_{ij} + BO^{\pi\pi}_{ij} \\ BO' &= \exp\left[p_1\left(\frac{r_{ij}}{r^{\sigma}_{o}}\right)^{p_2}\right] + \exp\left[p_3\left(\frac{r_{ij}}{r^{\pi}_{o}}\right)^{p_4}\right] + \exp\left[p_5\left(\frac{r_{ij}}{r^{\pi\pi}_{o}}\right)^{p_6}\right] \end{aligned} \tag{4.2}$$

where r_o are equilibrium bond lengths for each kind of bonding and p_n are empirical parameters. The final bond orders (BO) are obtained by multiplying the BO' from Eq. (4.2) by correction factors [42]. Once the BO are computed, E_{bond} is calculated according to:

$$E_{bond} = -D_e \; BO_{ij} \exp\left[p_{be,1}(1 - BO^{p_{be,1}}_{ij})\right] \quad , \tag{4.3}$$

with D_e being a bond dissociation energy.

The nonbonded Coulomb interactions are calculated for all atomic pairs as:

$$E_{Coulomb} = C \frac{q_i q_j}{[r_{ij}^3 + \gamma_{ij}^{-3}]^{1/3}} \tag{4.4}$$

where C is the Coulomb constant and γ_{ij} is a shield parameter, to avoid collapse between attractive charges [44]. The atomic charges $q_{i,j}$ are calculated using the electron equilibration method (EEM) approach [44, 45, 46].

EchemDID

As mentioned above, we simulate the effect of an external electrochemical potential required for forming, set and reset of HfO_2-based RRAM cells via EChemDID [43]. The modifies the electronegativity of the atoms in one electrode to $\chi_0 - \Phi/2$ and $\chi_0 + \Phi/2$ on the other, with χ_0 corresponding to the force field value, and Φ being the potential applied. The electronegativity propagates and equilibrates through the metallic ions in contact with electrodes according to:

$$\dot{\Phi} = k\nabla\Phi \ . \tag{4.5}$$

where k is a diffusive constant. This equation is solved numerically on-the-fly using atoms as a grid through the following expression:

$$\dot{\Phi}_i = k \sum_{k \neq i} \frac{\Phi_i(t) - \Phi_j(t)}{|R_{ij}|^2} w(R_{ij}) - \eta F(W_i)\Phi_i \ , \tag{4.6}$$

where η is the relaxation rate, $F(W)$ is a switch function that turns on when a metallic ion detaches from the other metallic atoms contacting the electrode, W_i is the total coordination of the atom i, and $w(R_{ij})$ is a weight function, calculated as:

$$w(R_{ij}) = \begin{cases} N\left[1 - \left(\frac{R_{ij}}{R_C}\right)^2\right]^2 & \text{if } R_{ij} < R_C, \\ 0 & \text{otherwise} \end{cases} \ . \tag{4.7}$$

Here N is a normalization constant, and R_C is a cut-off radius below which two atoms are considered part of the same metallic cluster, and therefore, have the same electronegativity. The calculated potential Φ_i is then added to the atomic electronegativity of the metallic ions, $\chi_i(t) = \chi_0 + \Phi_i(t)$, used in charge equilibration to adjust the energy of valence electrons.

4.2 Equations of motion

The equations of motion [47] are expressed as:

$$\begin{aligned} \dot{\mathbf{r}}_i &= \frac{\mathbf{p}_i}{m} \\ \dot{\mathbf{p}}_i &= \mathbf{f}_i = -\nabla V_i(\mathbf{r}) \end{aligned} \tag{4.8}$$

Where the forces are calculated from the interatomic potential (V) described in the previous section.

One of the simplest and most used methods to integrate Eq. (4.8) is the Verlet algorithm. It can be derived by doing Taylor expansion of the atomic position around a given time:

$$\mathbf{r}_i(t+\Delta t) = \mathbf{r}_i(t) + \mathbf{v}_i(t)\Delta t + \frac{\mathbf{f}_i(t)}{m}\frac{\Delta t^2}{2} + \dddot{\mathbf{r}}_i(t)\frac{\Delta t^3}{3!} + \mathcal{O}(\Delta t^4) \tag{4.9}$$

and

$$\mathbf{r}_i(t-\Delta t) = \mathbf{r}_i(t) - \mathbf{v}_i(t)\Delta t + \frac{\mathbf{f}_i(t)}{m}\frac{\Delta t^2}{2} - \dddot{\mathbf{r}}_i(t)\frac{\Delta t^3}{3!} + \mathcal{O}(\Delta t^4) \tag{4.10}$$

Summing these two equations, we obtain:

$$\mathbf{r}_i(t-\Delta t) + \mathbf{r}_i(t+\Delta t) = 2\mathbf{r}_i(t) + \frac{\mathbf{f}_i(t)}{m}\Delta t^2 + \mathcal{O}(\Delta t^4) \tag{4.11}$$

Therefore, we can compute the position for an advanced time as:

$$\mathbf{r}_i(t+\Delta t) \approx -\mathbf{r}_i(t-\Delta t) + 2\mathbf{r}_i(t) + \frac{\mathbf{f}_i(t)}{m}\Delta t^2 \quad . \tag{4.12}$$

As can be seen in Eq. (4.12), the Verlet algorithm estimates a new position using the positions at two previous timesteps (Δt), and involves an error on the order of $\mathcal{O}(\Delta t^4)$. Although the Verlet algorithm does not use the velocity to compute the new position, it can derive by doing:

$$\mathbf{r}_i(t-\Delta t) - \mathbf{r}_i(t+\Delta t) = 2\mathbf{v}_i(t)\Delta t + \mathcal{O}(\Delta t^3) \tag{4.13}$$

$$\mathbf{v}_i(t) \approx \frac{\mathbf{r}_i(t-\Delta t) - \mathbf{r}_i(t+\Delta t)}{2\Delta t} \tag{4.14}$$

Besides Verlet, there are other algorithms that are also based on a truncated Taylor expansion, such as the Leap Frog algorithm and the velocity Verlet algorithm [47, 48]. The Euler algorithm is similar to Verlet, but it uses the

forward difference approximation instead of central difference. As consequence, it requires a single position evaluation per timestep, instead of two, increasing the error. For this reason, this approximation is not used in MD, besides, it can be numerically unstable.

4.3 Statistical Ensembles

The thermodynamic state of a macroscopic system can be defined by a small set of parameters, such as temperature (T), pressure (P), volume (V), energy (E) and number of particles (N). The collection of all possible systems with different microscopic states (microstates), that correspond to the same thermodynamic state is defined as an statistical ensemble. From statistical mechanics, it is possible to calculate a macroscopic observable (A_{obs}) by averaging the value of such observable over the ensemble:

$$A_{obs} = \langle A \rangle_{ens} \quad . \tag{4.15}$$

In MD, the sequence of atomic positions and velocities (or momenta), that defines the phase space with $6N$ dimensions, belongs to the same statistical ensemble. For a particular point in the phase space, denoted as $\Gamma(\mathbf{r}(t), \mathbf{v}(t))$, we can write an instantaneous value of a property $A(\Gamma(t))$. Since in MD the system evolves in time, the property will also change throughout the simulation. Hence, it is reasonable to assume that the macroscopic observable A_{obs} can be calculated from the time average of the property A, taken over a long time interval:

$$A_{obs} = \langle A \rangle_{time} = \lim_{t_{obs} \to \infty} \frac{1}{t_{obs}} \int_{t=0}^{t_{obs}} A(\Gamma(t)) \; dt \tag{4.16}$$

Which can be alternatively expressed in a discrete form:

$$A_{obs} = \langle A \rangle_{time} = \lim_{\tau_{obs} \to \infty} \frac{1}{\tau_{obs}} \sum_{\tau=1}^{\tau_{obs}} A(\Gamma(\tau)) \tag{4.17}$$

where τ is a timestep, instead a continue variable.

Some of the ensembles are: i) **microcanonical ensemble**, characterized by a fixed number of atoms, energy and volume (NVE), where the systems are isolated and evolve independently; ii) **canonical ensemble** characterized by a fixed number of atoms, temperature and volume (NVT), where the system

exchange energy with a thermostat to maintain the temperature constant; and iii) **isobaric/isothermal ensemble** which fixes the number of atoms, the pressure and temperature (NPT). The simulations performed in the thesis are in the NVT and NPT ensembles. We used Nosé-Hoover [49, 50] thermostat and barostat since it allows to perform simulations at constant the temperature and pressure, reproducing at the same time the fluctuations of the corresponding ensemble.

Chapter 5

MoS_2 lateral metal-semiconductor junctions

Adapted from:

M Laura Urquiza and Xavier Cartoixà, *"Schottky barriers, emission regimes and contact resistances in 2H-1T' MoS_2 lateral metal-semiconductor junctions from first-principles"*, 2D Mater. **7** 045030, DOI:10.1088/2053-1583/ aba449.

Ultrathin transition metal dichalcogenides (TMDs) have emerged as promising semiconductors to overcome the short channel effects that arise with the miniaturization of field effect transistors (FETs) [10]. Due to their 2D geometry and wide bandgap (in the range of 1-2 eV), these materials would reduce the direct source-drain tunnelling current and could improve the transport properties of the channel [51]. Moreover, the absence of dangling bonds outside the 2D plane gives a perfect interface with the gate and the substrate, which, together with the atomically thin structure, allows an excellent electrostatic gate control. TMDs are also very promising for the new generation of flexible electronics; in fact, flexible and transparent FETs have been already demonstrated using semiconducting MoS_2 channel [52]. But TMDs in electronics are not restricted to single devices, as complex circuitry such as a MoS_2 microprocessors has also been reported [11].

Despite the novel properties of these materials, the performance of TMD-based FETs is normally limited by the formation of Schottky barriers at the

interfaces between the 2D channel and the metallic electrodes, which translates into a high contact resistance (R_c), in the range of 10^4 to 10^6 $\Omega \cdot \mu$m [53]. Some of the attempts to reduce the negative effects of the Schottky barrier include the use of metals with low work function [54], metals with high chalcogenide (S, Se, Te) affinity, able to provide a strong hybridization between the channel and the electrode [55, 56], and the use of substitutional doping [57].

So far, the most promising solution for the contact resistance issue seems to be the use of phase engineering to build contacts between the semiconducting (2H) and the metallic phase of TMDs [58]. This metallic phase can be either the 1T, where one of the chalcogenide planes is rotated 60 degrees and the structure acquires inversion symmetry; or the 1T', which is a distortion/structural relaxation of the 1T phase with a lower energy [59, 60, 61]. Experimentally, the presence of the 1T' phase has been observed by Eda *et al.* [62] and Lin *et al.* [63]. The 1T' phase is used to connect the 2H channel to the metallic pads, in the same way that p^+ or n^- doped regions are implemented in the traditional silicon-based FETs to connect the Si channel to the metallic electrodes. With this strategy, it was possible to achieve record low R_c values of 200-300 $\Omega \cdot \mu$m in MoS_2-based FETs [64]. These FETs also demonstrated good performance, with mobility values of 50 $cm^2/V{\cdot}s$, subthreshold swing values of 90–100 mV and on/off ratios greater than 10^7 [64].

In this chapter, the finite bias transport properties of MoS_2 lateral metal-semiconductor junction are studied using density functional theory (DFT) and non-equilibrium Green's functions calculations, where the effect of the electrostatic gating on the semiconducting phase was emulated including electrostatic doping. The chapter is organized as follow: it starts explaining the methods used to perform the calculations and the model for emulating the electrostatic doping. Then it introduces the transport properties of 2H-1T and 2H-1T' interfaces, including the effect of the doping, and the study of the emission regimes through the Schottky barriers formed at the interface. It finishes with the study of Schottky barrier heights, and contact resistances under different doping concentrations and external voltages.

5.1 Methods

5.1.1 System description and computational details

Electronic structure and transport calculations are performed within the DFT (Chapter 2) and NEGF (Chapter 3) formalisms, as implemented in the SIESTA [28] and TRANSIESTA [65] codes.

The exchange correlation functional was approximated with the Generalized Gradient Approximation (GGA) using the Perdew-Burke-Ernzerhof (PBE) parametrization [24]. Although for 2D materials the GGA gaps often match experimental optical gaps despite the well known DFT underestimation of band gaps, this is because the experimental gaps are subject to strong excitonic effects that reduce the single particle gaps [66]. Since band alignments and carrier injection are expected to depend on the single particle band structure, the limitation of plain LDA/GGA still stands. This might affect the overall value of the Schottky barrier heights (SBHs) provided, but relative differences in SBHs should be more accurate [67].

We use norm-conserving pseudopotentials [68] to describe the core electrons and a double-ζ polarized basis set for the valence electrons. The Brillouin zone was sampled using a grid of 9x16x1 **k**-points for the 6-atom orthogonal unit cell of the 2H phase, and its equivalent for supercell calculations. The real space grid cutoff was set to 250 Ry.

Ionic positions were relaxed using a force tolerance of 0.03 eV/Å for the SIESTA calculation and 0.05 eV/Å for TRANSIESTA calculations. In the case of structures with interfaces, the cell was also optimized until the strains were lower than 0.1 GPa (1 kbar).

MoS_2 heterostructures

The interfaces studied consist of a single layer MoS_2 heterostructure, where the semiconducting phase (2H) is contacted laterally to the metallic or semimetallic phase (1T or 1T'). Figure 5.1 shows the band structure of the three phases: 2H, 1T and 1T'. In order to avoid interactions between images in the non-periodic direction, a vacuum of 20 Å was included. Two different orientations for the semiconducting-metallic interface, armchair (ac) and zigzag (zz), were considered.

Figure 5.2 shows the device setup for transport calculations. The scattering

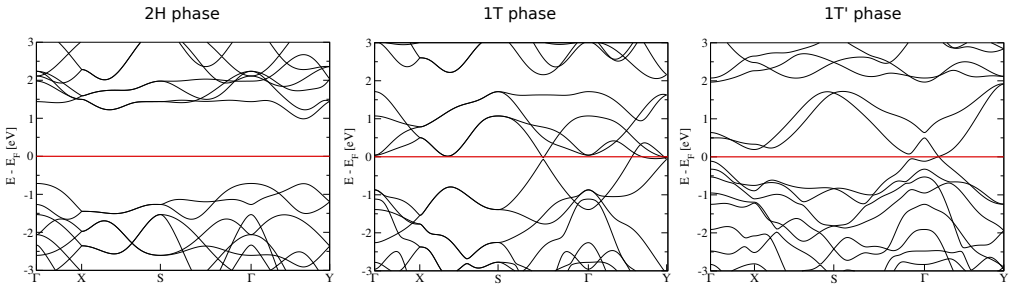

Figure 5.1: Band structure of the fully relaxed MoS_2 2H, 1T and 1T' phases

region is 13 nm (16.5 nm) long for the armchair (zigzag) device. We also performed preliminary calculations to decide the optimal MoS_2 heterostructures, where we used structures with scattering regions of 1.6 nm (2.7 nm) for ac (zz) interfaces. Since the system has dissimilar electrodes, we added buffer regions of pristine 2H and 1T/1T' structures after each electrode to provide a bulk-like environment to the electrode atoms.

Electrostatic doping

The charge density induced by a gate voltage (V_g) was simulated by adding a specific fixed charge in the 2H region, with the total number of electrons chosen to satisfy global charge neutrality. The electrons in the system will then self-consistenly respond to the dopant-like fixed charges when Poisson's

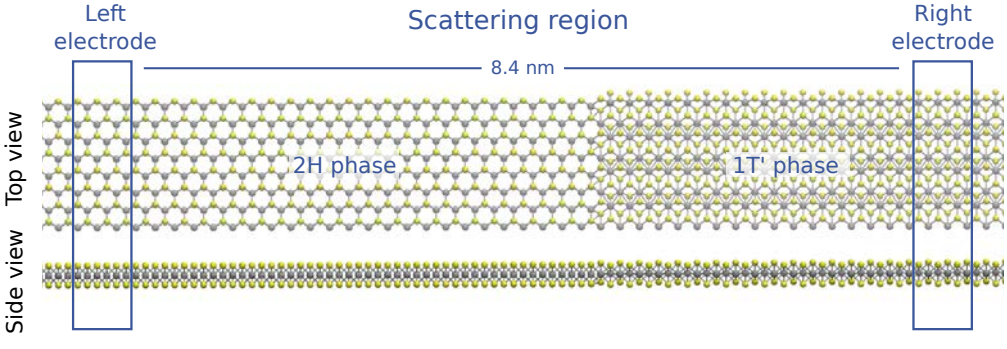

Figure 5.2: Device set-up for transport calculations, the structure shown corresponds to armchair 2H-1T' interface. Yellow and grey spheres represent sulphur and molybdenum atoms, respectively.

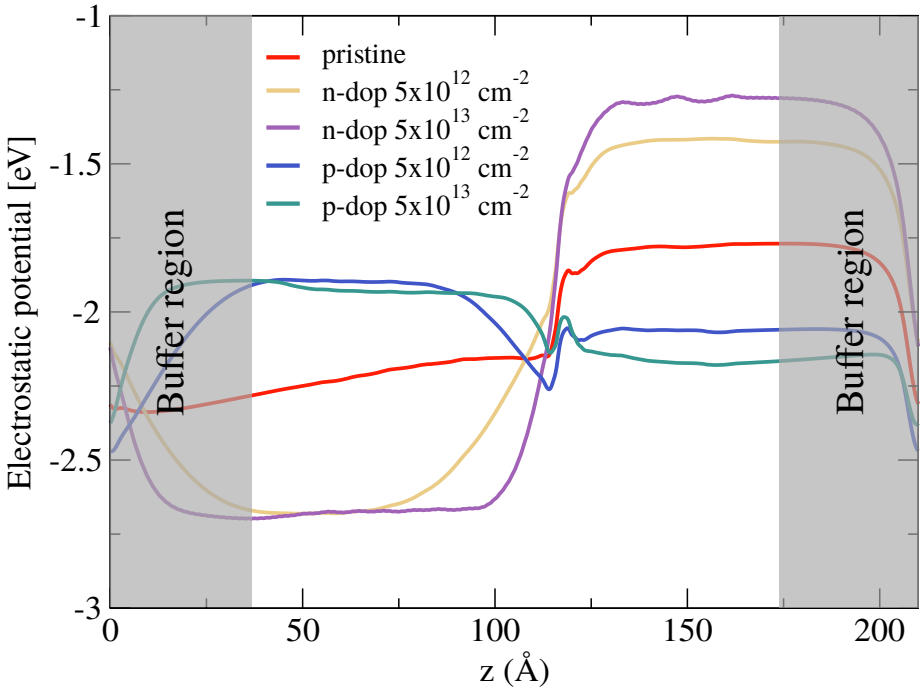

Figure 5.3: Electrostatic potential along the transport coordinate (z) for armchair interface with different doping concentration in the semiconducting phase.

equation is solved. This scheme is very similar to the one used by Stradi *et al.* [69], with the difference that they used compensation charges localized around the semiconductor atoms to ensure overall charge neutrality, while here the compensation is uniformly distributed over a rectangular box tightly surrounding the semiconducting region. The overall effect is that there is a drive for the Fermi level to be rigidly shifted, as sometimes imposed in electronic transport calculations mimicking dopant effects [70]. On the other hand, while this approach cannot account for the capacitive effects induced by the gate, or the gate-induced electric field perpendicular to the channel [71], it does have the advantage of not depending on the particular distribution of the atomistic impurities or the geometry of the system [69]. In this work, we considered channel charge densities of $5{\times}10^{12}$ cm^{-2} and $5{\times}10^{13}$ cm^{-2}. We refer to p-doped (n-doped) system when the mobile charge added into the channel is positive (negative).

For an accurate description of the electrostatics with NEGF, it is required

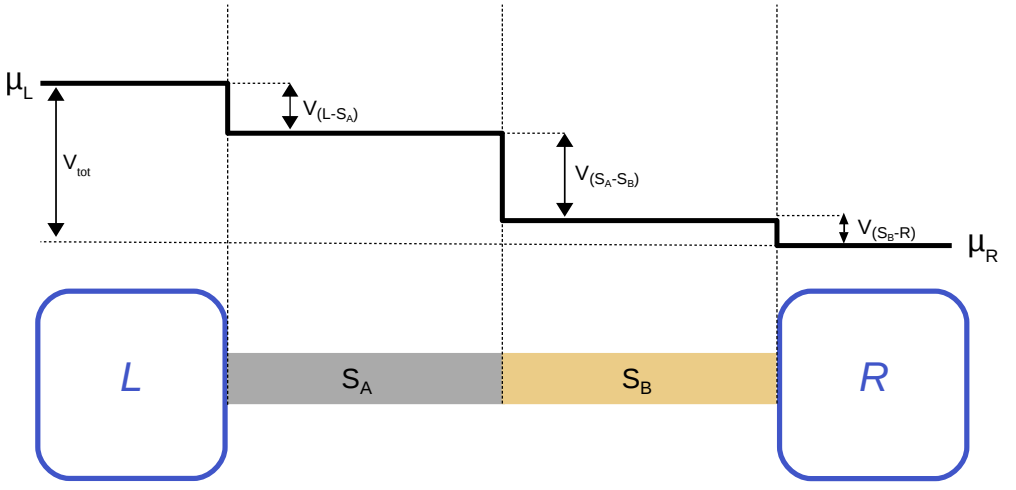

Figure 5.4: Voltage drop scheme for the device set-up. Here, L and R represent the left and right contacts, and S_i represents the different phases present in the scattering region.

that the electrodes behave as bulk, meaning that the electrostatic potential should have reached its bulk behavior at the boundary between the scattering region and the semi-infinite bulk electrodes. Therefore, we plotted the potential profile along the transport direction for devices with different doping concentration, as shown in Figure 5.3. Here, it can be seen that for the undoped structure, the dipole formed at the interface is not screened in the 2H phase, as a consequence, we did not carry out transport calculations for this case.

5.1.2 Contact resistance extraction

The large signal contact resistance of an interface can be obtained from the ratio between the voltage drop across the junction and the current flowing through it. Using NEGF it is possible to calculate the current that flows through a device when a potential is applied at the semi-infinte contacts. In these calculations, however, the applied voltage (V_{tot}) is distributed between the interface present in the scattering region, ($V_{S_A-S_B}$), and the interface between the semi-infinite contacts with the device (V_{L-S_A} and V_{S_B-R}), as shown in Figure 5.4. Therefore,

the total applied voltage can be expressed as:

$$V_{tot} = V_{L-S_A} + V_{S_A-S_B} + V_{S_B-R}, \tag{5.1}$$

from where

$$R_{tot} = R_{L-S_A} \; + \; R_{S_A-S_B} \; + \; R_{S_B-R}. \tag{5.2}$$

Here R_{tot} represents the total series resistance, and it can be obtained from the I–V curves of the whole device. On the other hand, R_{L-S_A} and R_{S_B-R} are the resistances between the contacts and the electrodes, which are obtained from I–V reference curves of pristine devices, all of the same phase. Since pristine devices include two electrode-contact junctions, the value extracted for each reference calculation must be divided by two to consider the contribution of a simple electrode-contact interface:

$$R_{L-S_A} = \frac{1}{2}\,\frac{V_{S_A-S_A}}{I} \quad \text{and} \quad R_{S_B-R} = \frac{1}{2}\,\frac{V_{S_B-S_B}}{I}, \tag{5.3}$$

where $V_{S_A-S_A}$ and $V_{S_B-S_B}$ are the potentials applied in the pristine devices to obtain the same current value as in the whole device.

Finally, $R_{S_A-S_B}$, which is the resistance corresponding to the junction between the two phases, can be calculated from the other terms by replacing Eq. (5.3) into Eq. (5.2) and reordering:

$$R_{S_A-S_B} = \frac{V_{tot}}{I} \; - \; \frac{1}{2}\,\frac{V_{S_A-S_A}}{I} \; - \; \frac{1}{2}\,\frac{V_{S_B-S_B}}{I}. \tag{5.4}$$

A similar analysis can be performed to obtain the small signal contact resistance, but in this case, instead of taking the ratio between voltage and current at each point, we take the derivative of the voltage with respect to the current to compute the resistance. Carrying this process out we have

$$R^{small}_{S_A-S_B}\Big|_{I_0} = \frac{\partial V_{tot}}{\partial I}\Big|_{I_0} - \frac{1}{2}\,\frac{\partial V_{S_A-S_A}}{\partial I}\Big|_{I_0} - \frac{1}{2}\,\frac{\partial V_{S_B-S_B}}{\partial I}\Big|_{I_0}, \tag{5.5}$$

where derivatives are evaluated at the bias that provides a current I_0, corresponding to the bias V_0 of interest for the whole device.

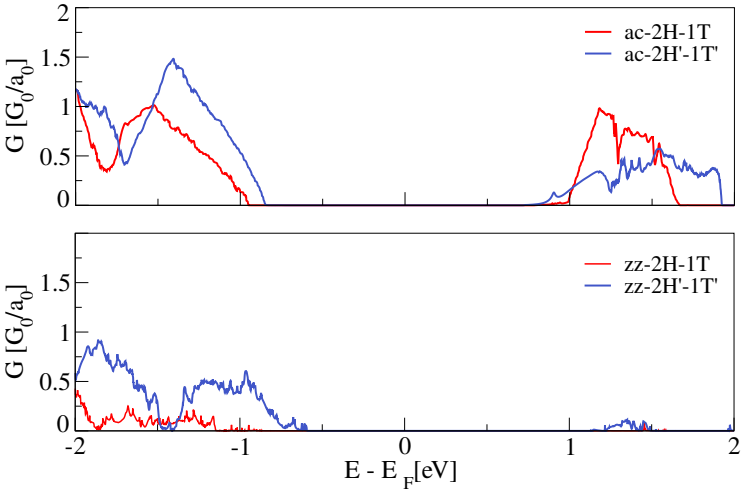

Figure 5.5: Specific conductance, in units of G_0 over the transverse lattice parameter (a_0), for 2H-1T and 2H'-1T' MoS_2 structures with armchair and zigzag interfaces.

5.2 Transport properties of MoS_2 heterojunctions

To understand the transport properties of MoS_2 heterojunctions, we calculated the specific conductance (i.e. conductance per unit of channel width) using the Landauer formula [30], explained in Sec. 3.1:

$$G(E)a_t = \frac{2e^2}{h}\, T(E) = G_0\, T(E)\ , \tag{5.6}$$

where $T(E)$ are the transmission coefficients averaged over all the $\mathbf{k}_{\|}$, obtained from the NEGF calculations, and a_t is the width of the computational cell along the direction perpendicular to transport.

Conductance of 2H-1T and 2H'-1T' interfaces

Although DFT calculations have predicted that the 1T phase is unstable and undergoes a distortion that naturally leads the 1T' phase [59], experimental results report that the 1T phase can be stabilized by the presence of adsorbates, vacancies defects, or under specific environmental conditions [64].

In our calculations the 1T phase could not be stabilized without including external constraints. However, in order to predict which phase of MoS_2 could

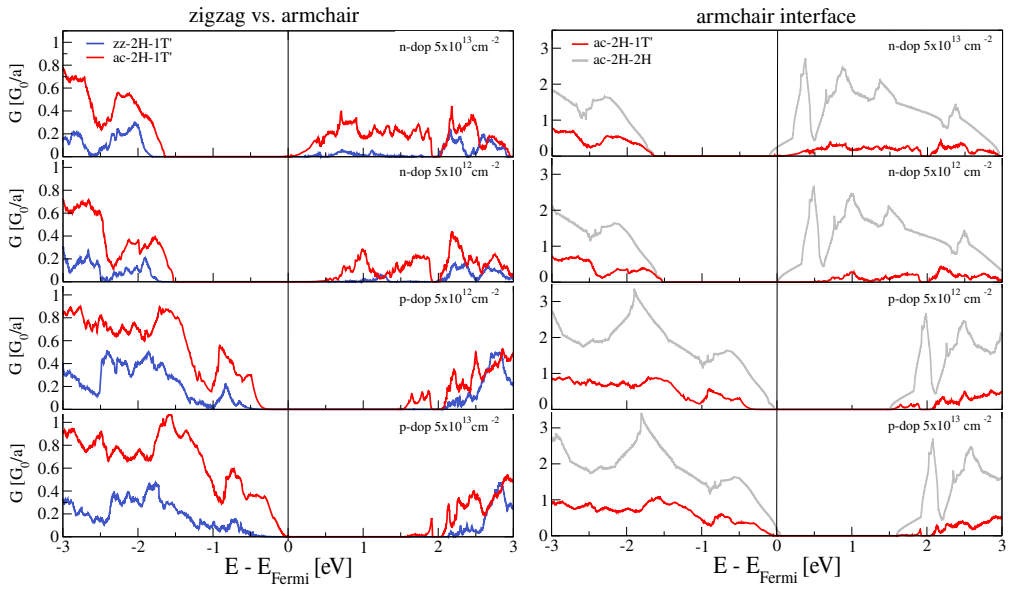

Figure 5.6: Specific conductance at zero bias, in units of G_0 over the transverse lattice parameter (a_0), for armchair and zigzag 2H-1T' interfaces with different doping concentration (left), and armchair 2H-1T' and 2H-2H MoS_2 interfaces with different doping concentration (right).

be more convenient for contacting the semiconducting 2H phase, we performed preliminary calculations to compare the conductance of 2H-1T and 2H'-1T' structures (2H' means 2H distorted to match the cell parameter of the 1T'). Figure 5.5 shows the results for armchair (ac) and zigzag (zz) geometries, where we observe superior conductance when using the 1T' phase. Although these results are not enough data to support the statement that 1T' should make a better contact than 1T, the higher conductance, plus the superior structural stability of the 1T' phase, led us to use 2H'-1T' interfaces for our study. From now, it will be referred as 2H-1T' to avoid confusing the reader with the notation of the phases.

Conductance of armchair and zigzag interfaces

We compared the transport properties of zigzag and armchair structures in order to predict which is the most promising configuration for transport. In Figure 5.6 (left) we show the specific conductance as a function of the energy of the incoming

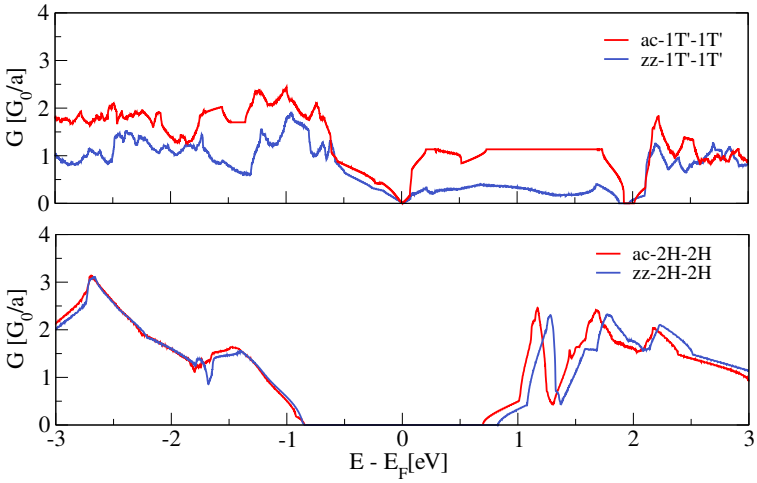

Figure 5.7: Conductance of pristine 2H and 1T' phases. The orientation in the legend corresponds to the transport direction.

particle, for armchair and zigzag 2H-1T' interfaces. The results show that the ac interface has an enhanced transmission for the injection of both holes and electrons. The difference in the transport across the ac and zz interfaces comes essentially from the asymmetrical behaviour of the 1T' phase, as can be seen in Figure 5.7, which has higher conductance when transport direction is perpendicular to the ac interface. As for the 2H phase, it can be noticed that there is a small difference in the bandgap of the zz and ac structures, which is caused by the different strains induced along the armchair and zigzag directions to lattice match with the 1T' phase.

In Figure 5.6 (right) we show the specific conductance for armchair 2H-1T' and 2H-2H interfaces with p and n-doping concentration of $5{\times}10^{12}$ cm^{-2} and $5{\times}10^{13}$ cm^{-2}. Comparing the transmission for the 2H-1T' device to the 2H-2H reference device, which provides the maximum attainable transmission, a notable reduction of the conductance is observed, mainly for the structures with intermediate doping concentration. The results also show that the injection of holes is slightly favored due to the higher number of transmission channels in the valence band.

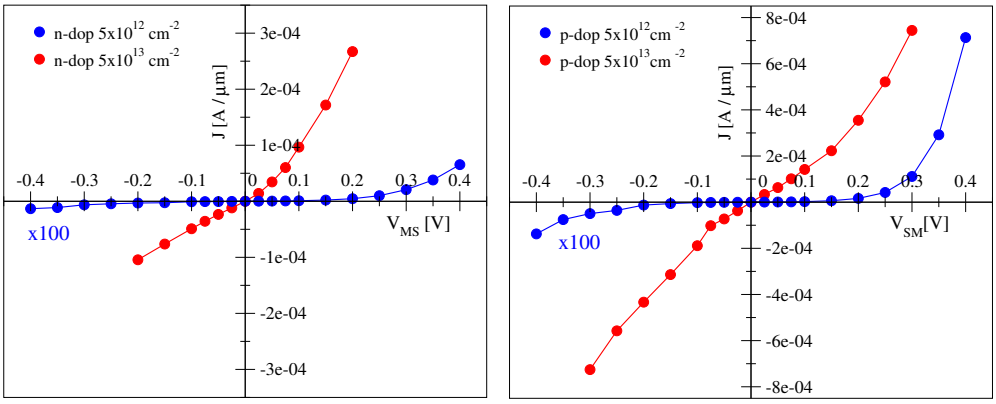

Figure 5.8: Current vs. voltage curve of n-doped (left) and p-doped (right) 2H-1T' armchair structures.

5.3 Emission regimes

For armchair interfaces, we also performed NEGF calculations at finite bias, showing the resulting current vs. voltage (I–V) characteristics in Figure 5.8. For the highly doped structures, we observe a slight asymmetry at forward and reverse biases, specially in the n-doped structure, but overall there is an ohmic behavior in the I–V curve. For intermediate doping concentrations, we observe an exponential increase of the current at forward bias, indicative of a Schottky regime, and a poor rectifying behavior, also typical of Schottky contacts. In this regime, the transport mechanism can be (a) thermionic emission (TE) over the Schottky barrier (SB), (b) field emission (FE) with electrons around the Fermi level tunneling through the SB, or (c) thermionic-field emission (TFE), where the tunneling electrons contributing to the current are quite above the semiconductor Fermi level, but still below the top of the SB [72].

In order to determine which of these mechanisms dominates in 2H-1T' junctions, we performed a temperature study of the forward I–V characteristics. The results are shown in Figure 5.9. Plots a) and c) show the forward bias I–V characteristic for n and p-doped structures, respectively, at different temperatures, while plots b) and d) show the energy E_0 extracted from a fit of the I–V curves to $J \propto \exp(qV/E_0)$. When FE or TFE dominate, we have $E_0 = E_{00}\coth(E_{00}/kT)$ [72], where E_{00} is an energy related to how fast the trans-

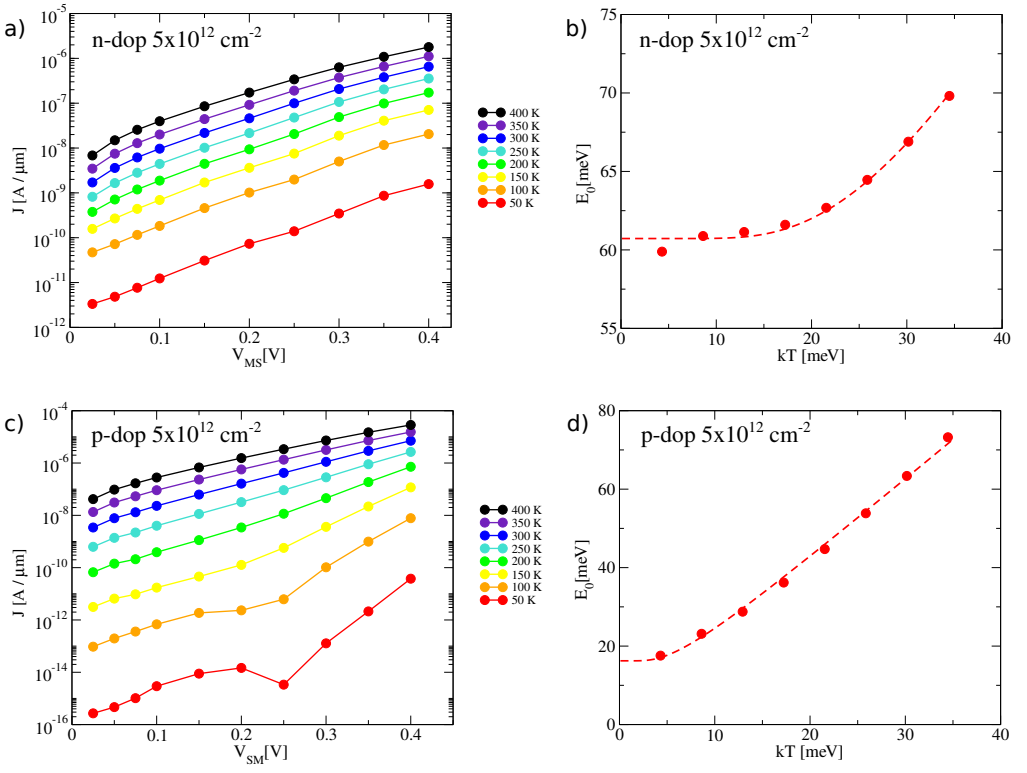

Figure 5.9: Forward I–V curves of a) n-doped and c) p-doped structures at different electronic temperatures, and E_0 values as a function of the temperature for b) n-doped and d) p-doped structures.

mission coefficient through the barrier increases as the forward bias is increased. If $kT \ll E_{00}$, then FE will dominate, while when $kT \sim E_{00}$ TFE is the main mechanism [73]. On the other hand, if $kT \gg E_{00}$ then TE dominates, and we will have $E_0 \sim \eta kT$, where η is an ideality factor accounting for the variation of the SBH with the applied bias.

All these considerations can be summarized into the following prescription, which can also be applied to experimental measurements, allowing the determination of the dominating transport mechanism: for a range of temperatures T, fit the I–V curves to $J \propto \exp[qV/E_0(T)]$; then fit $E_0(T)$ to

$$E_0(T) = E_{00} \coth(E_{00}/\eta kT) \tag{5.7}$$

and finally compare E_{00} to kT to determine whether FE, TFE or TE dominates,

obtaining the ideality factor η as a by-product. Performing this analysis prior to an activation-energy study should be required in order to ensure that TE dominates transport across the junction, since that is the regime assumed in the activation-energy study. Otherwise, a too strong dependence of the SBH with the metal-semiconductor bias might ensue, even leading to unphysical negative values for the SBH [74]. Further information within the tunneling regime can be obtained with the analysis by Mouafo *et al.* [75].

We have fitted the n-doped structure in Figure 5.9.b) to Eq. (5.7), obtaining $E_{00} = 60.72$ meV and $\eta = 1.33$. So, for this case we are in the FE regime, with a small temperature assistance. The p-doped case is more complicated. We see in Figure 5.9.c) how, specially at low temperatures, the curves present two regions with separate temperature dependence; at small bias the T dependence is weak, becoming stronger at bias $\gtrsim 0.25$ V. Figure 5.9.d) shows E_0 extracted from a fit in the forward bias [0.3, 0.4] V range, where we see that, at low T, we have some contribution of TFE current, overwhelmed by TE current at medium and large temperatures (the fitted parameters are $E_{00} = 16.25$ and $\eta = 2.04$).

It is desireable to find E_{00} by other means in order to check the consistency of the treatment and have further validation for the claimed transport regime. In the case of a 3D structure and a parabolic barrier, E_{00} can be easily evaluated from the metal-semiconductor (MS) junction parameters, finding that $E_{00} = q\sqrt{N_D\hbar^2/4\varepsilon_s m^*}$ [72], where N_D is the 3D dopant concentration, ε_s is the semiconductor dielectric constant and m^* is its effctive mass, under the parabolic dispersion assumption. For the 2D MS junction, the barrier profile is no longer parabolic [76], difficulting the obtaining of an analytical expression. However, E_{00} can be numerically estimated noting that the transmission coefficient for carriers coming at the Fermi level E_F may be written as [77]:

$$T(E_F) = \exp\left[-q(V_B - E_F - V)/E_{00}\right], \tag{5.8}$$

where V_B is the Schottky barrier height in the semiconductor side and V is the applied bias. We have carried out this approach, plotting the transmission coefficient as a function of the applied bias in Figure 5.10 for the $n, p = 5 \times 10^{12}$ cm^{-2} doping at an incoming electron energy of $E_F + \delta E$ eV[1] and fitting to

[1]The incoming energy with respect to the Fermi level must be increased (decreased) for

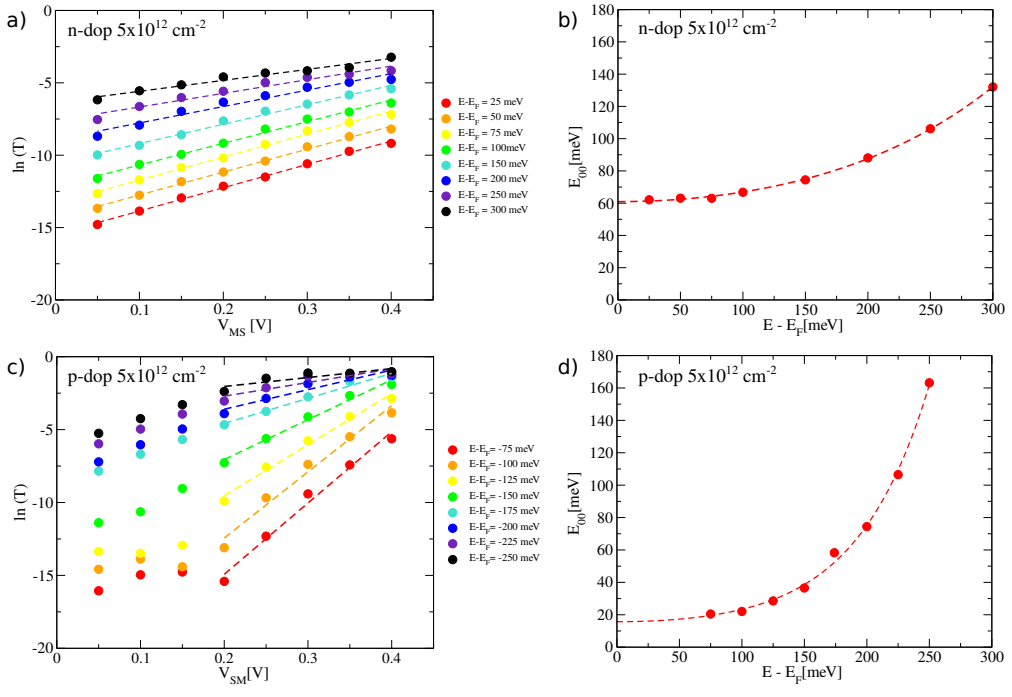

Figure 5.10: Logarithm of the transmission coeficients (T), at the indicated carrier incoming energies, as a function of the applied bias (dots), and linear regression with slope $S = 1/E_{00}$ (dashed lines), for a) n-doped and c) p-doped structures. Plots b) and d) show the slope as a function of the excess energy δE and its extrapolation to $\delta E = 0$.

Eq. (5.8), for several δE. The obtained slopes have been extrapolated to $\delta E = 0$ with a cosh function, and from there we have obtained for the $n = 5 \times 10^{12}$ cm^{-2} case $E_{00} = 61.0$ meV, in excellent agreement with the value obtained from the temperature analysis, thus corroborating the assignation to the FE regime. For the $p = 5 \times 10^{12}$ cm^{-2} case we have obtained $E_{00} = 15.7$ meV, which, being quite smaller than kT at room temperature, corroborates the assignment to the TE regime.

electrons (holes) to ensure that the incoming carriers have allowed energies.

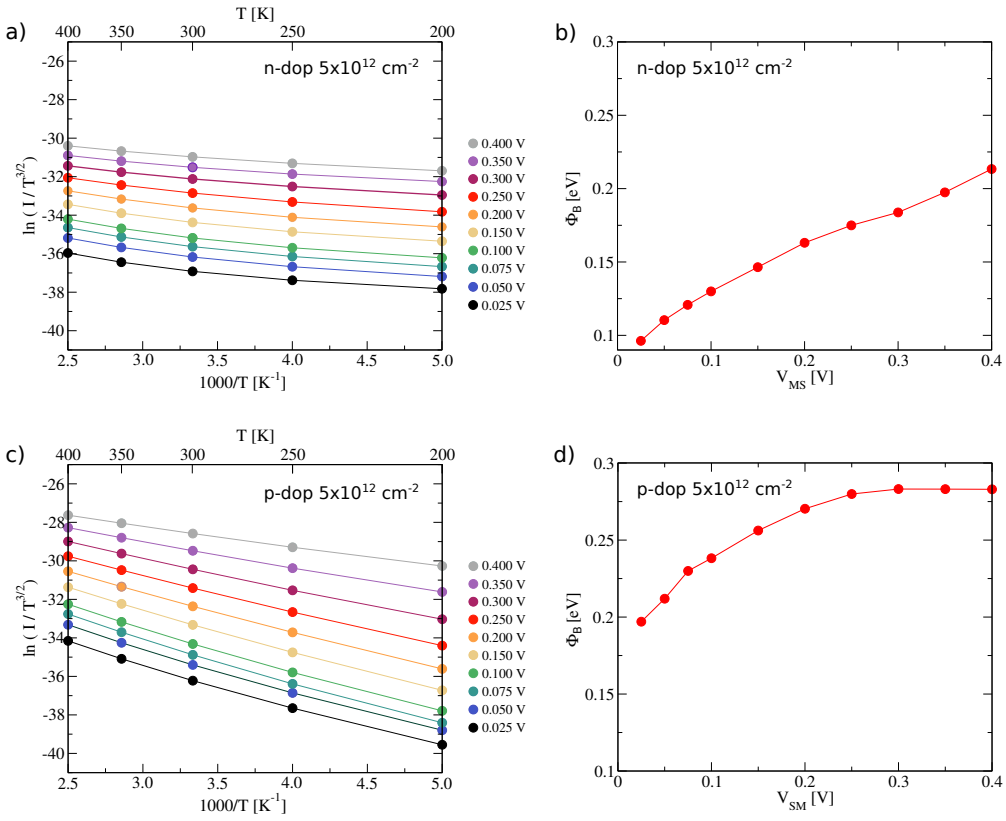

Figure 5.11: Arrhenius plots of $\ln(I_{ds}/T^{3/2})$ vs. 1/T at different gate voltages for a) n-doped and c) p-doped ac-2H-1T' suctures, and Schottky barrier height (Φ_B) for b) n-doped and d) p-doped structures extracted from the activation energy method at different bias.

5.4 Schottky barriers of 2H-1T' interfaces

In this section we discuss two different approaches used to obtain Schottky barriers in metal-semiconducting junctions. One of them is the standard activation energy method (AEM) performed on I–V curves calculated with NEGF formalism, and the other uses energy resolved local density of state to describe the band alignment and extract the barrier height.

Activation energy method

In experiments, Schottky barrier heights (Φ_B) are normally obtained through the activation-energy method (AEM), which uses the thermionic emission equation to extract Φ_B from the $\ln(I/T^\alpha)$ vs. $1/T$ plot. Here α is an scaling exponent equal to 2 for 3D systems and 3/2 for lateral 2D lateral heterostructures [78].

While this method can be applied to the intermediate p-doped case at high bias, it is not suitable for the intermediate n-doped and low bias p-doped cases because the doping concentrations we considered are high enough to observe transport governed by FE or TFE. Nevertheless, we applied the activation energy method to illustrate its failure to provide a definite value for the Schottky barrier height in the intermediate doping structures. The results are shown in Figure 5.11, from which we extract $\Phi_B = 0.28$ eV for the p–$5{\times}10^{12}$ cm^{-2} structure.

Local density of states

As an alternative to the AEM, we studied the effect of the gate bias on the Schottky barriers using local density of states (LDOS) plots. Although penetration of the metallic states into the semiconductor gap renders the direct determination of the SBH difficult, we can use the macroscopic average of the Hartree portential, which traces quite closely the conduction and valence band profile [69], to extract the n-doped and p-doped barrier according to:

$$\Phi_{B,n} = q(V_i - V_{bulk}) + (E_{CBE} - E_F^{2H}) - (E_F^{1T'} - E_F^{2H}) \tag{5.9}$$

$$\Phi_{B,p} = q(V_{bulk} - V_i) + (E_F^{2H} - E_{VBE}) - (E_F^{2H} - E_F^{1T'}), \tag{5.10}$$

where V_{bulk} is the average Hartree potential at the semiconductor side far from the influence of the interface, V_i is the average Hartree potential at the interface, and E_{CBE} and E_{VBE} are the conduction band and valence band edges, respectively, extracted from the LDOS. Finally, in order to take into account the case of an applied bias across the junction, we define $E_F^{1T'}$ and E_F^{2H} as the respective Fermi levels.

The LDOS plot for 2H-1T' armchair (zigzag) interfaces at zero bias and different doping concentrations are shown in Figure 5.12 (5.13). The barrier heights and the depletion layer width (W) extracted from the LDOS plots are presented in Table 5.1. From the plots for the undoped structures, it can be seen that Φ_B

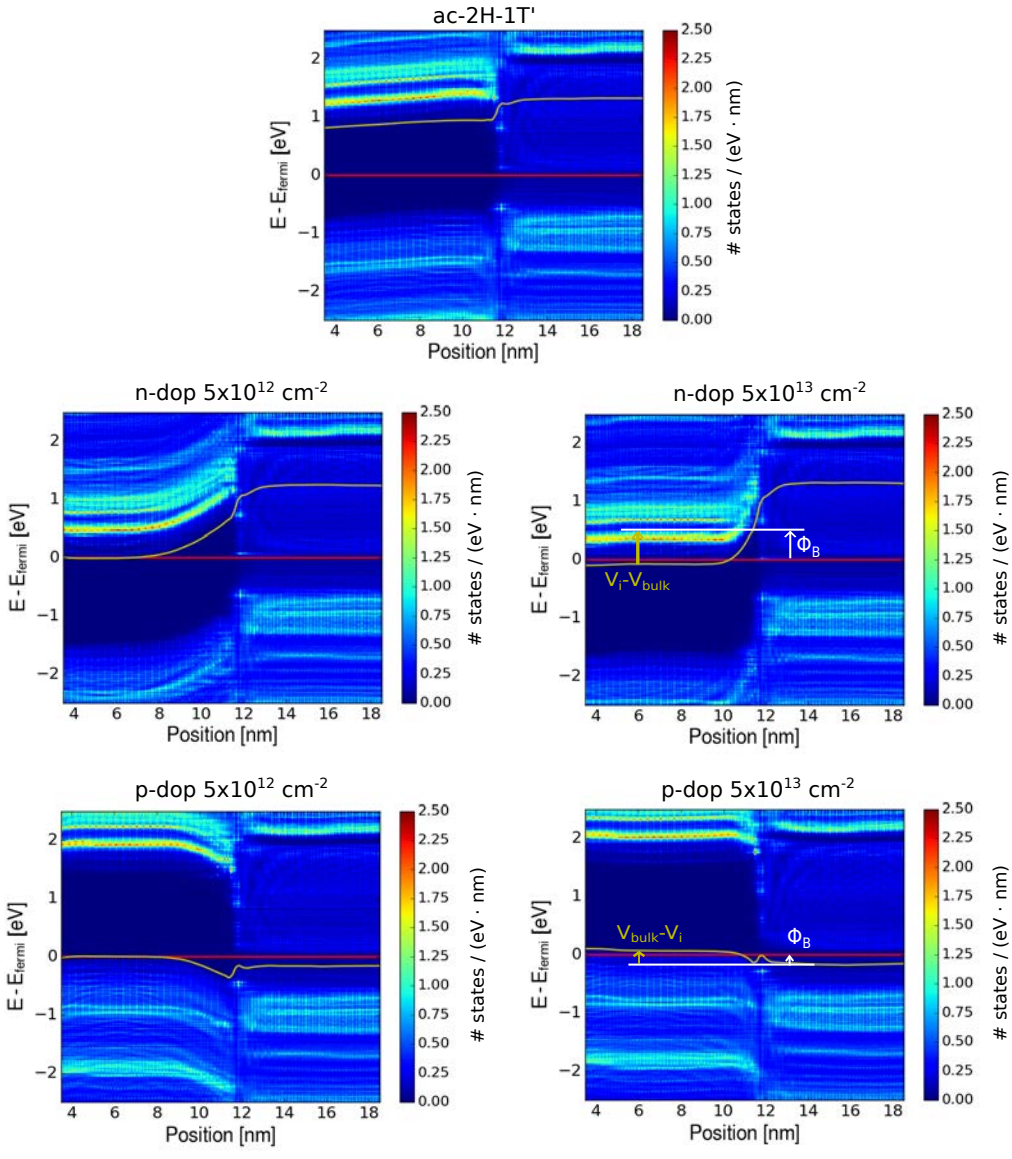

Figure 5.12: Energy-resolved local density of states (LDOS) of ac-2H-1T' structures with different p and n doping concentrations. The red and yellow lines denote the Fermi level and the average Hartree potential, respectively.

for the injection of holes is lower than for electrons, the values being 0.6 (0.7 eV) and 0.97 (1.0 eV), respectively. This result is in good agreement with other theoretical values reported in literature, where the height of the p and n-barriers

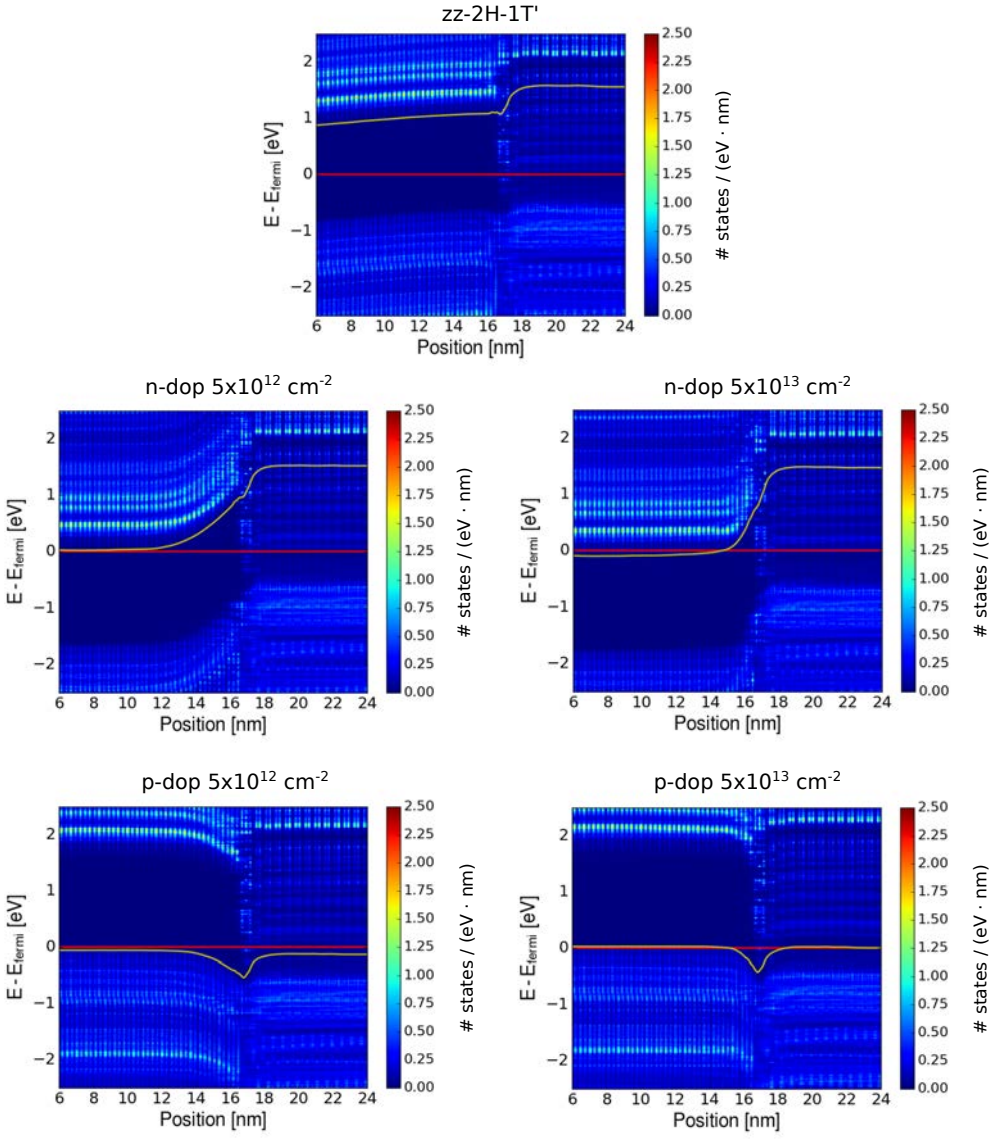

Figure 5.13: Energy-resolved local density of states (LDOS) of zz-2H-1T' structures with different p and n doping concentrations. The red and yellow lines denote the Fermi level and the average Hartree potential, respectively.

were found to be 0.71 eV and 0.96 eV, respectively [79]. We also observe that the Schottky barrier decreases when the electrostatic doping increases, and it slightly varies for ac and zz interfaces. This evidence indicates that Schottky-Mott Rule

δq [cm $^{-2}$]	n-doped		p-doped	
	$\Phi_{B,n}$ [eV]	W [nm]	$\Phi_{B,p}$ [eV]	W [nm]
0	0.97 (1.0)	>8.6 (8.6)	0.58 (0.7)	>8.6 (8.6)
5×10^{12}	0.78 (0.8)	4.5 (4.1)	0.39 (0.4)	2.9 (3.2)
5×10^{13}	0.60 (0.3)	1.3 (1.1)	0.04 (0.3)	0.9 (1.0)

Table 5.1: Schottky barriers Φ_B and depletion layer widths (W) for n and p-doped ac (zz) interfaces extracted from the LDOS shown in Fig. 5.12 (5.13).

does not apply in these highly doped 2H-1T' semiconductor-metal juctions, as expected for non-ideal systems [80]. A similar behavior was also observed in DFT studies of a Ag/Si 3D junction, where increase of the semiconductor doping level led to a reduction of the SBH [69] by similar amounts. Note that this dependence of the SBH on the doping level is qualitatively different from that reported in graphene-silicon contacts [81], because there the variation in electrostatic doping was applied to the graphene "metallic" component of the junction, thus changing the metal workfunction. Additionally, our results point to the possibility that the 2H-1T' junction is free from Fermi level pinning, a possibility already hinted at by Katagiri *et al.* [82], since the Fermi level position at the interface spans most of the semiconductor gap region (cf. the two 5×10^{13} cm^{-3} plots in Figure 5.12 for the two extreme cases). This is opposite to junctions with 3D metals, where pinning of the Fermi level was found [83, 84, 85]. This might open up the possibility of ambipolar injection into MoS_2, similarly to what has been observed in $MoTe_2$ under weak Fermi level pinning conditions [86].

To understand the effect of the applied voltage on the band alignment of the 2H-1T' interfaces, we also represented the LDOS of the ac structures under finite bias. In Figures 5.14 and 5.15 we show the results for n- and p-doped structures, respectively. The Φ_B calculated according to Eqs. (5.9) and (5.10) are presented in Table 5.2 for different biases.

In all cases we observe Φ_B slightly reduces (increases) when the 2H-1T' junction is reverse (forward) biased, again by amounts similar to what was

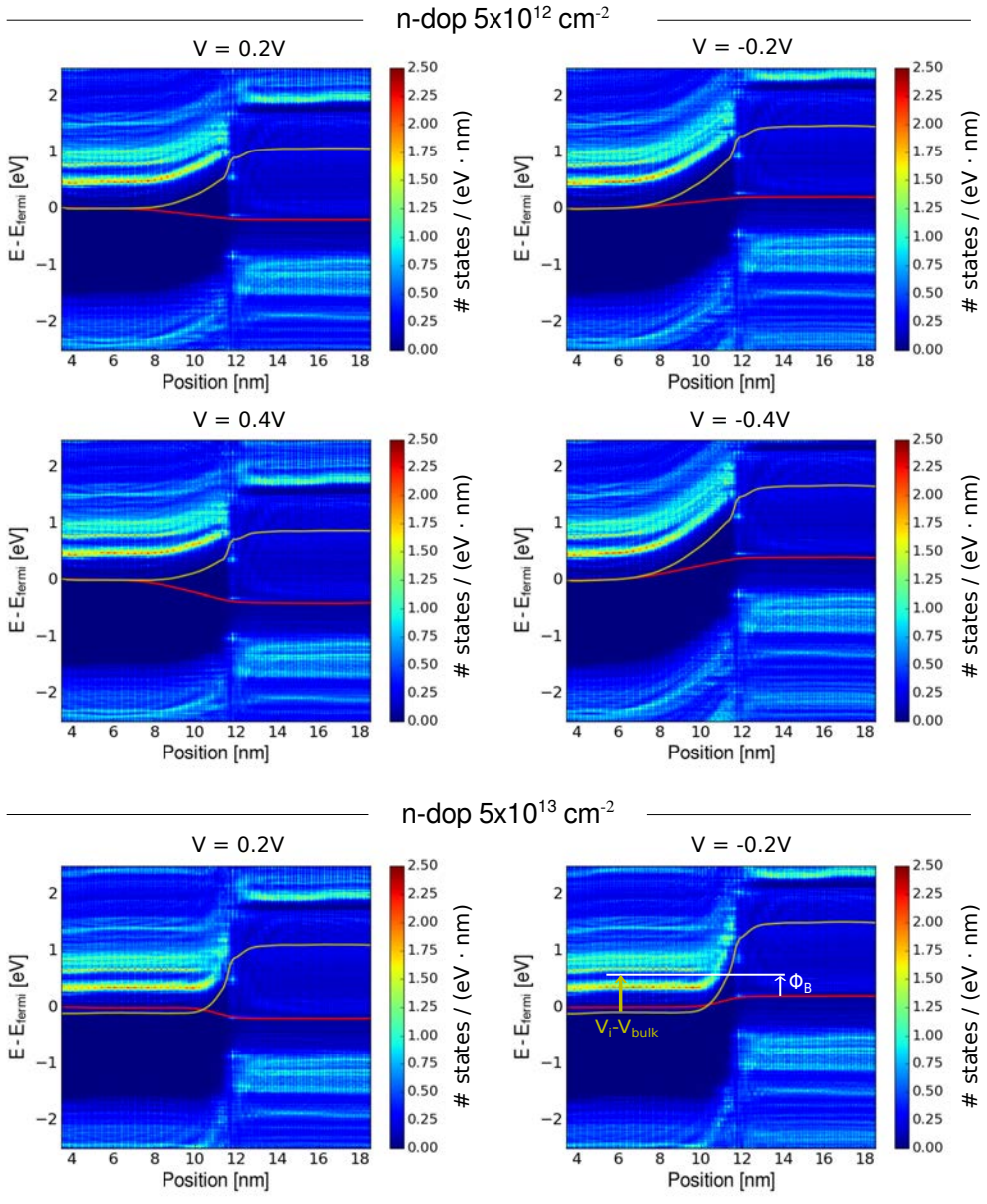

Figure 5.14: LDOS of n-doped ac-2H-1T' structures at different applied voltage. The colorbar indicates the density of states. The red line is the difference between the averaged potential at finite bias and zero bias. The yellow line is average potential of the structure with the applied voltage. Positive (negative) voltage indicates forward (reverse) bias.

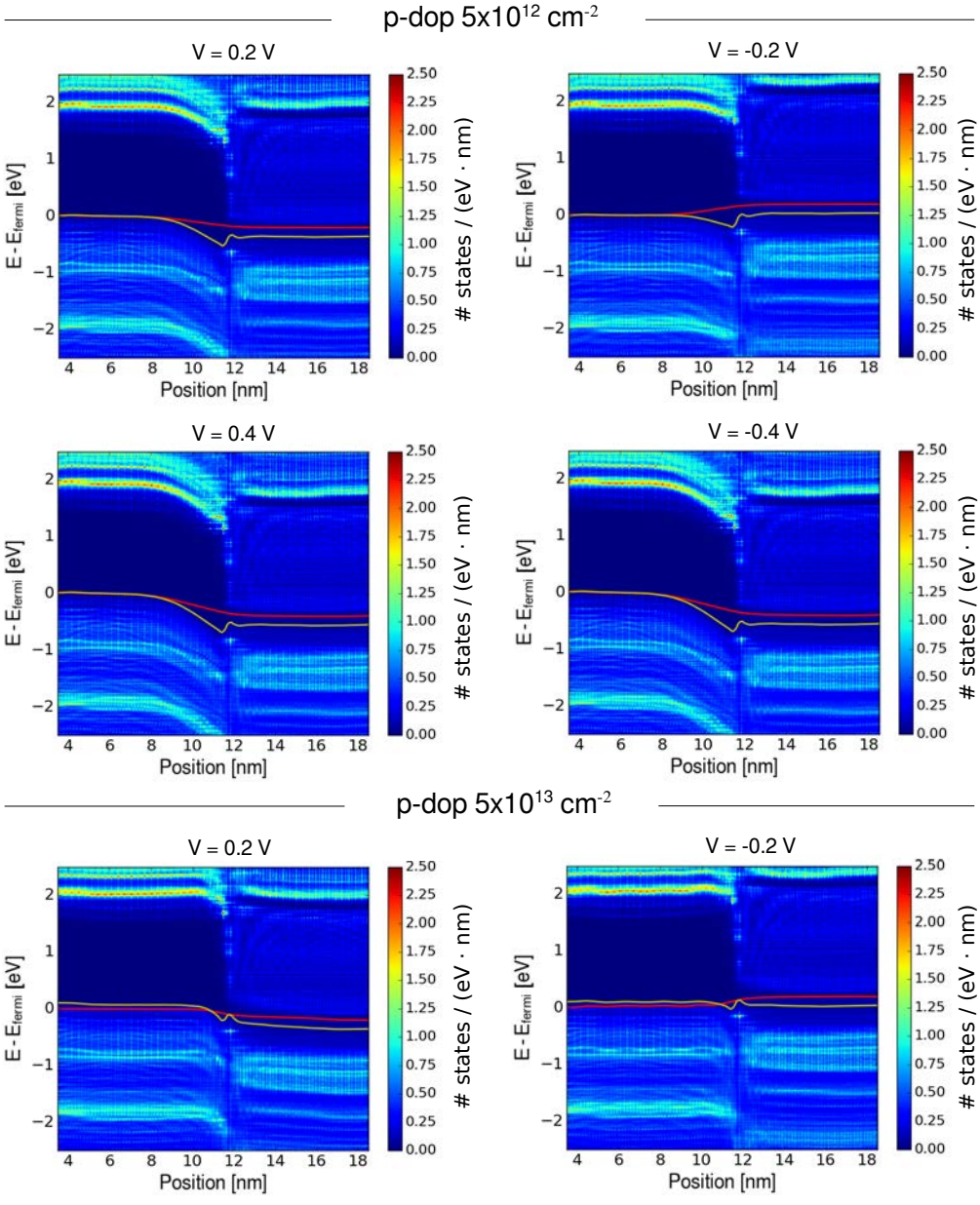

Figure 5.15: LDOS of p-doped ac-2H-1T' structures at different applied voltage. The colorbar indicates the density of states. The red line is the difference between the averaged potential at finite bias and zero bias. The yellow line is average potential of the structure with the applied voltage. Negative (positive) voltage indicates forward (reverse) bias.

μ_{1T}	n-dop 5×10^{12}	n-dop 5×10^{13}	p-dop 5×10^{12}	p-dop 5×10^{13}
-0.4 eV	0.85	–	0.32	–
-0.2 eV	0.82	0.64	0.35	0.03
0.0 eV	0.79	0.58	0.39	0.15
0.2 eV	0.77	0.53	0.44	0.27
0.4 eV	0.74	–	0.49	–

Table 5.2: Schottky barriers Φ_B for structures with different doping concentrations under finite bias, extracted from the LDOS plots shown in Figure 5.14 and Figure 5.15.

observed in the Ag/Si junction [69], where this variation was attributed to the effect of image forces [73]. For the case of intermediate n(p)-doping concentrations, 5×10^{12} cm^{-2}, when the 2H side is forward biased with respect to the 1T' phase, V>0 (V<0) in Figures 5.14 and 5.15, the 2H band edge raises (lowers) and the effective barrier is reduced, increasing the current. When the junction is reverse biased the band bending increases, and so does the depletion layer; as result, only a small leakage current flows. On the other hand, when the transport is ohmic (high doping concentrations 5×10^{13} cm^{-2}), the band bending is almost imperceptible and the current flows independently of the bias polarization in both types of doping.

5.5 Contact resistance of 2H-1T' interfaces

We calculate the large and small signal contact resistance (R_c), relevant for digital applications, of the 2H-1T' interfaces ($R_{2H-1T'}$) at 300 K using Eqs. (5.4) and (5.5), respectively, explained in Sec. 5.1.2:

$$R_{2H-1T'} = \frac{V_{tot}}{I} - \frac{1}{2}\frac{V_{2H-2H}}{I} - \frac{1}{2}\frac{V_{1T'-1T'}}{I}, \tag{5.11}$$

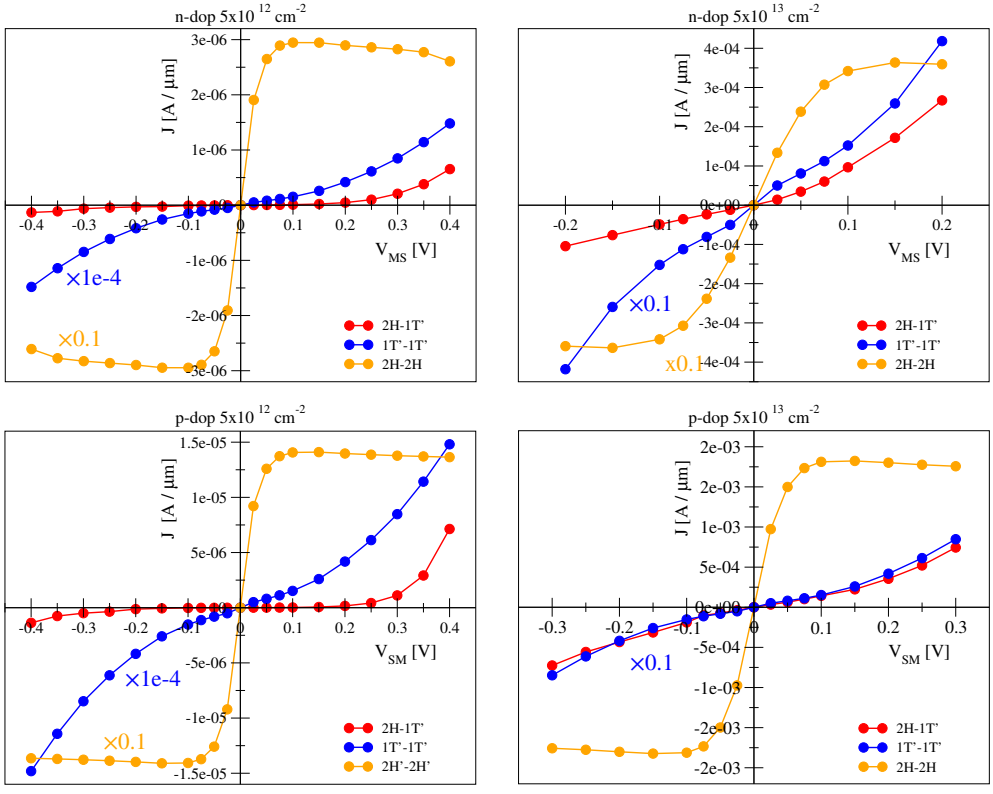

Figure 5.16: Current vs. voltage curve for the ac-2H-1T' device and reference devices (ac-2H-2H and ac-1T'-1T') with different doping concentration.

$$R^{small}_{2H-1T'}\Big|_{I_0} = \frac{\partial V_{tot}}{\partial I}\Big|_{I_0} - \frac{1}{2}\frac{\partial V_{2H-2H}}{\partial I}\Big|_{I_0} - \frac{1}{2}\frac{\partial V_{1T'-1T'}}{\partial I}\Big|_{I_0} \tag{5.12}$$

where the voltages V_{tot}, V_{2H-2H} and $V_{1T'-1T'}$ have been extracted from the I-V curves shown in Figure 5.16 at the same current value. Note that the deviations from linearity observed in the reference electrode I–V curves reflect features of the underlying density of states.

The resulting large- and small-signal contact resistances for different electrostatic dopings as a function of $V_{MS/SM}$ are shown in Figure 5.17, finding a qualitatively similar behavior for both cases.

As expected from the I–V curves in Figure 5.16, positive doping yields lower

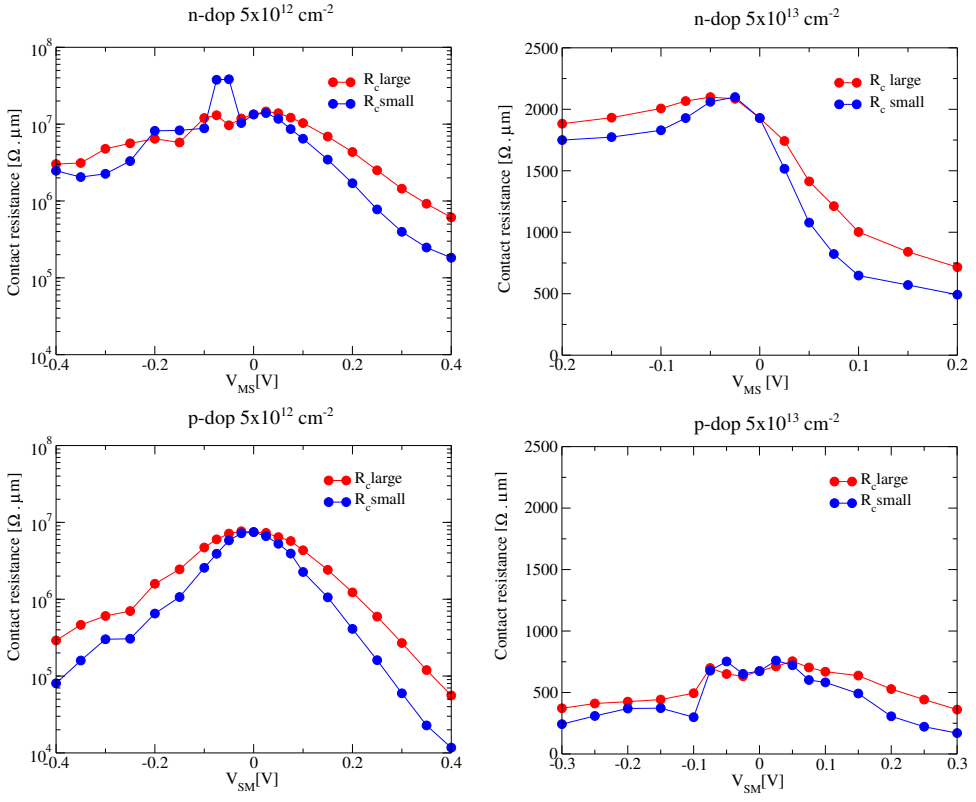

Figure 5.17: Small and large signal contact resistances as a function of V_{ds} for ac-2H'-1T' contacts with different doping concentration.

contact resistance than negative doping by a factor of ∼10 (∼4) in the intermediate (high) doping case. We also observe that in the intermediate-doping/Schottky case the contact resistance has an exponential dependence with V_{MS}, very clear at forward bias. Having established in Sec. 5.3 that the junction operates in the FE (TE) regime for the n (p) case, the exponential decrease of R_c at forward bias is due to the narrowing and lowering of the barrier seen from the semiconducting side (V_{bi}, see Figure 5.12). In the reverse bias, the lowering of $R_{2H-1T'}$ is due to the narrowing of the tunnel barrier for a fixed energy of the carrier coming from the metal side. In the high-doping/ohmic case, a linear drop in $R_{2H-1T'}$ is observed at forward bias. This is due to the (linearly) increased transmission as bias is raised.

Houssa *et al.* also performed calculations of contact resistances for 2H-1T—as opposed to 1T'—lateral heterojunctions but without including electrostatic doping. They obtained R_c values on the order of 40 and 30 $k\Omega \cdot \mu m$ for armchair and zigzag interfaces, respectively, using the transfer length method [87]. These values are much lower than our results for intermediate doping; however, the differences may be related to the procedure of computation of the R_c. They used the transfer length method, with semiconductor lengths up to 4.8 nm. As we can see in Figure 5.3, the depletion width for the undoped case is > 8 nm, meaning that they treated the fully depleted case, with some amount of indirect doping from the metal contacts.

We also compared our results to experimental measurements of MoS_2-based FETs with metal-semiconductor junctions. Nourbakhsh *et al.* reported R_c values of 1 $k\Omega \cdot \mu m$ at gate voltages of 3.5 V, i.e. for sufficiently high negative charge induced in the channel [88]. This result is in agreement with our calculations for negative $5{\times}10^{13}$ cm^{-2} doping concentration at forward bias. On the other hand, Kappera *et al.* reported R_c values of 0.24 $k\Omega \cdot \mu m$ at zero gate voltage [64]. This extreme low value, obtained without inducing any charge in the channel, has been explained by considering the functionalization of 1T' phase with chemical dopants (H, Li, or H_2O), present during the local transformation of semiconducting 2H phase into metallic 1T' phase [87].

5.6 Summary

We used non-equilibrium Green's function formalism to perform transport calculations at finite voltage of armchair and zigzag 2H-1T' interfaces, where an electrostatic doping was added to the semiconducting 2H phase to emulate the gate voltage on the channel. It was observed that armchair interfaces provide better conductance as result of the anisotropic transport behavior of the 1T' phase. Besides, from the I–V analysis it was found that (i) electronic transport follows ohmic and Schottky regimes in highly and intermediate doped structures, respectively, (ii) for the Schottky case, the transmission occurs by tunneling in the intermediate n-doped structure and by thermionic emission in the p-doped structure.

The Schottky barrier heights of structures under different doping concentration and finite bias were obtained through their LDOS, observing that the barrier heights in 2H-1T' structures are sensitive to the applied voltage, both at the gate and at the semiconductor, and there was no indication of the presence of Fermi level pinning. We also computed the contact resistance for different dopant types and concentrations as a function of the voltage applied across the junction, finding a lower 2H-1T' contact resistance for the *p*-doped 2H phase.

Finally, we have also pointed out a method that can be used to experimentally identify the emission regime (i.e. tunnel or thermoionic), prior to a possible use of the activation-energy method.

Chapter 6

Molecular dynamics simulations of HfO_2-based RRAM devices

Resistive random-access memories (RRAM) are considered the most promising candidates for the next generation of high scaling, ultrafast and low power consumption memories [89, 90, 91]. RRAM cells, that typically consist of a metal-insulator-metal (MIM) stack, store bits by reversibly changing the resistivity of the insulator between a high resistance state (HRS) and a low resistance state (LRS).

In most of RRAM devices the switching between LRS/HRS originates from the formation/rupture of a nanoscaled conductive filament (CF) in the dielectric layer. This is the case of memories operating through electrochemical metalization mechanism (ECM), where the CF consists of metallic atoms injected from an active electrode into the dielectric, and valence change mechanism (VCM), where the filament is a conductive region in the dielectric with a high concentration of oxygen vacancies [92]. In this thesis we focused on HfO_2-based RRAM devices that operate through a VCM.

In the valence change mechanism, the CF formation is triggered by the migration of oxygen anions from the oxide towards the active electrode, driven by an external electric field. The subsequent reduction of the oxide, expressed as a change in the valence of the Hf atoms, is responsible for the electronic

conductivity in the LRS [93, 94].

Depending on the choice of electrode materials, the devices can be operated through unipolar or bipolar switching mode. For a bipolar behaviour, metals with high oxygen affinity are chosen as the active electrode (AE), meanwhile inert metals are preferred for the inactive electrode (IE). The AE plays an important role in the operation of VCM cells because it acts as an oxygen exchange layer, creating a substoichiometric region at the oxide interface that contributes significantly to reduce the forming voltage and improve the endurance and retention of the cell [95, 96, 97]. The most used AE materials are Ti, Hf and Ta due to their oxygen scavenging ability and good electrical performance [96, 98].

In this chapter we present an atomistic study of the forming, reset and set processes in HfO_2-based RRAM cells through molecular dynamics (MD) simulations, using an extended charge equilibration method to describe the external electric field. We will start explaining the schemes used to perform the MD simulations, then the substoichiometric layer generated at the HfO_2/AE interface, and finally the operation of the RRAM cells.

6.1 Simulation details

The MD simulations have been performed using LAMMPS code [99], with a time step of 0.2 fs, which leads to good energy conservation under NVE conditions. For the NVT and NPT simulations we used Nose-Hoover [49, 50] thermostat and Parrinello-Rahman [100] barostat, with relaxation times of 10 fs and 100 fs, respectively.

6.1.1 Force field

The interatomic interactions are described with ReaxFF, explained in Sec. 4.1, parameterized for Hf-O systems. In this section we will detail the structural information predicted by the force field, such as lattice parameters of Hf/HfO_2 systems, atomic distances and oxygen coordination.

	DFT (this work)	ReaxFF (this work)	Experimental
a [Å]	3.19	3.1375	3.1964
c [Å]	5.05	5.1248	5.0511
Cohesive energy [eV]	-6.47	-6.33	-6.99

Table 6.1: Comparison of the lattice parameter and cohesive energy of hcp-Hf obtained in this work with experimental results and DFT calculations.

Structural parameters

We calculated the lattice parameters and cohesive energy of metallic hafnium (hcp-Hf), finding good agreement with experimental and first principle calculations results, as shown in Table 6.1. We also tested the parameters for amorphous hafnia ($aHfO_2$), obtained through melt/quench process. The Hf-Hf, Hf-O and O-O bond distances, were extracted from the radial distribution function (RDF) shown in Figure 6.1, and summarized in Table 6.2, where we compare the results with values from experiments, DFT calculations and other MD simulations.

Oxygen coordination

The coordination distribution of Hf and O in $aHfO_2$ was computed at 300 K. We determined the coordination number by counting the number of neighbour atoms of the opposite specie inside a cutoff radius equal to 2.7 Å, which corresponds

	Hf-Hf distance [Å]	Hf-O distance [Å]	Denisty [g/cm^3]
MD (this work)	2.0 and 2.5	3.3 and 3.9	10.44
Experimental [101]	2.13	3.38 and 3.89	7.69
DFT [102]	2.10	3.0 and 4.3	8.63
MD [103]	2.1	3.6	—-
MD [104]	2.112	3.41 and 3.86	8.60

Table 6.2: Comparison of amorphous HfO_2 parameters.

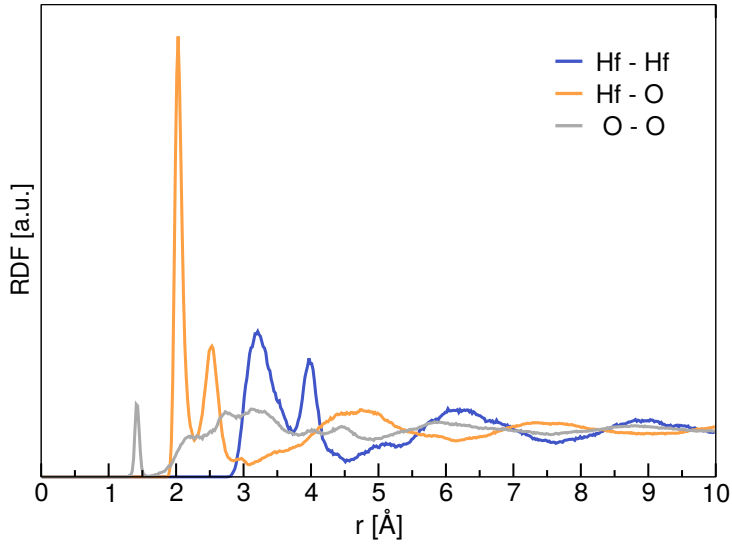

Figure 6.1: Radial function distribution of amorphous HfO2 at 300 K.

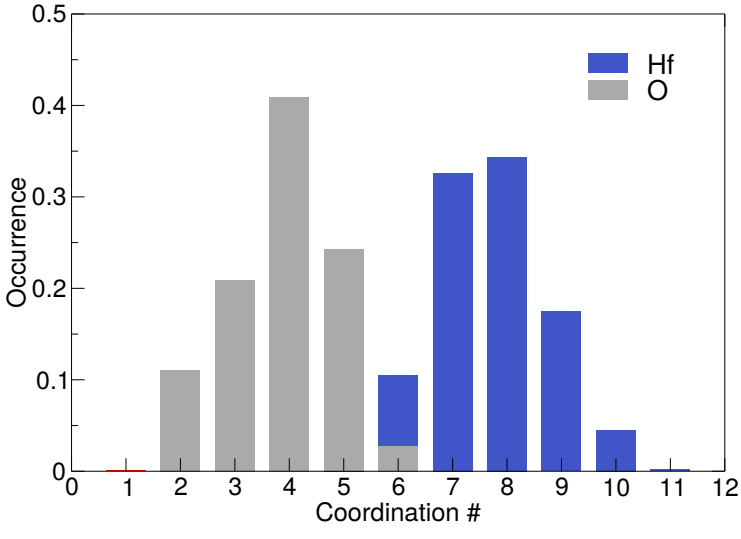

Figure 6.2: Coordination histogram of hafnium and oxygen atoms in amorphous HfO_2 at 300K.

to the minimum between the 2nd and the (very small) 3rd peak at 2.9 Å in the Hf-O RDF. The resulting histograms are shown in Figure 6.2, where it can be seen that Hf atoms are mainly seven and eight-fold coordinated, and O atoms are mostly 4-fold coordinated. These values are slightly higher than the obtained by Broglia et. al., who reported a coordination average of 6.92 for Hf and 3.07 for oxygen [104]. However, our results are in agreement with the expected coordination in monoclinic hafnia, where Hf atoms are seven-fold coordinated, and O atoms are three and four-fold coordinated.

6.1.2 Atomistic device model

The simulated RRAM cells consist of an amorphous HfO_2 layer sandwiched between an active and an inactive electrode. We use metallic Hf as active electrode to induce the formation of a substoichiometric HfO_x layer at the HfO_2/Hf interface. To simplify the simulations, the inert electrode is also described by Hf atoms, but the positions of these atoms are fixed throughout the simulation to mimic their unreactive character.

To consider the natural device-to-device variability of the real cells, five different aHfO_2 structures were obtained through a melt/quench process and attached to metallic electrodes. The melt was obtained by increasing the temperature up to 3300 K, corresponding to the melting point temperature of hafnia, and equilibrating the systems for 100 ps. To obtain statistically independent amorphous structures, we performed the quench of the liquid every 5 ps decreasing the temperature to 1 K in 100 ps. During the entire process, the volume was allowed to change in z axis to maintain the pressure at 1 atm. The cross section of amorphous samples is kept at 2.5×2.5 nm^2 to match the Hf electrodes. The system sizes were selected to result in an initial dielectric thickness of approximately 1.5 nm.

6.1.3 Filament description

In order to characterize the formation and dissolution of the CF, it is necessary to identify and track the oxygen vacancies and the related change in valence of the Hf atoms that allow electronic conductivity. In monoclinic hafnia (mHfO_2), vacancies are normally defined as point defects with respect to the perfect crystal

structure [105, 106, 107], since each atom has a specific atomic site, with a fixed number of bonds, or coordination. In aHfO_2 this is not possible because there is no reference structure, and the Hf atoms have a coordination distribution instead of a single value, as demonstrated in Figure 6.2. To overcome this issue, we study the evolution of the CF using as reference conductive Hf atoms, instead of oxygen vacancies.

First-principles transport calculations have demonstrated quantized conductance in metal/mHfO_2/metal structures with single vacancy filaments [108], consisting of Hf atoms bridging two oxygen vacancies (i.e. five-fold coordinated hafnium). Therefore, we define conductive Hf those atoms with an oxygen coordination number equal to or lower than 5.

In order to visualize the filament formation and disruption, we computed the oxygen coordination through the MD simulations using a cutoff for inclusion of 2.7 Å, corresponding to the minimum in the Hf-O RDF 6.1. Then, Hf atoms with coordination equal to or lower than 5 were considered for cluster analysis, using a cutoff radius of 3.9 Å to compute the connectivity between the metallic electrodes, which corresponds to 30% of the bond order for two isolated Hf atoms.

6.1.4 External electrochemical potential

The external electrochemical potential applied during forming, reset and set processes was simulated through EchemDID method, described in Sec 4.1. The diffusion equations were integrated 10 times per MD time step, while the atoms are maintained fixed, using a diffusion constant of 6 $Å^2$/fs and η=0. The cutoff radius used to determine the connectivity with the electrode was chosen of 3.9Å with a normalization factor (N) equal to 0.5.

Since the character of the atoms evolves during the reactive simulation, as conductive filaments form and break, and the coordination of Hf atoms changes, the group of metallic ions over which EchemDID propagates the potential was updated every 50 ps. Defining metallic ions as Hf atoms with coordination ≤ 5. Updating the electronegativity as the simulations proceeded is necessary to obtain robust reset events, or set events at all.

6.2 Generation of oxygen vacancy profiles

As mentioned in the introduction, a robust switching in VCM devices requires some amount of oxygen deficiency in the dielectric film. These vacancy profiles can be generated by an oxygen reactive electrode [94, 95, 98], or by other methods [97, 109]. In our simulations, the relaxation of the HfO_2/Hf interface naturally leads to the generation of a suboxide layer and a high concentration of vacancies in the initial stoichiometric dielectric. The interface relaxation was performed isothermal-isobaric (NPT) ensemble at 300 K and 1 atm for 100 ps, to generate a fully relaxed HfO_2/Hf interface. The time considered is enough to ensure that further oxygen migration towards the active electrode be negligible.

In our samples, the diffusion of oxygen atoms toward the active electrode increases the thickness of the oxide layer by approximately 0.5 nm. Although there are no experimental data for the thickness of the interlayer formed between Hf and HfO_2, our result is similar to the 1.3 nm measured with XRD for the TiOx layer at a HfO_2/Ti interface [110]. This provides an important, if indirect, validation of our approach.

Figures 6.3a) and 6.3b) show snapshots of the initial and relaxed structures of one of the samples generated through melt/quench process (sample A). In Figure 6.3c) we plot the planar average of the O/Hf ratio (stoichiometry) along the z axis, for the two states. Here, it can be seen that the initial stoichiometry, corresponding to HfO_2, evolves to a profile HfO_x, with x ranging from 2 at the inert electrode interface, to 0.5 at the active electrode interface. The stoichiometry plots for the five different samples generated are shown in Figure 6.4, obtaining similar results for all cases.

Figures 6.3d) and 6.3e) show the atomic charges corresponding to same initial and final structures mentioned above, and Figure 6.3f) displays the planar average of the hafnium charge along the z coordinate. The figures demonstrate how self-consistent charge equilibration results in neutral electrodes and positively charged Hf ions in the oxide and sub-oxide layer. The atomic charge evolution of Hf atoms after the relaxation clearly evidences the oxidation of Hf atoms at the active electrode, and the consequent reduction of the HfO_2.

The suboxide layer formed as consequence of the oxidation/reduction process results in a change of the Hf valence. Given the importance of the valence change

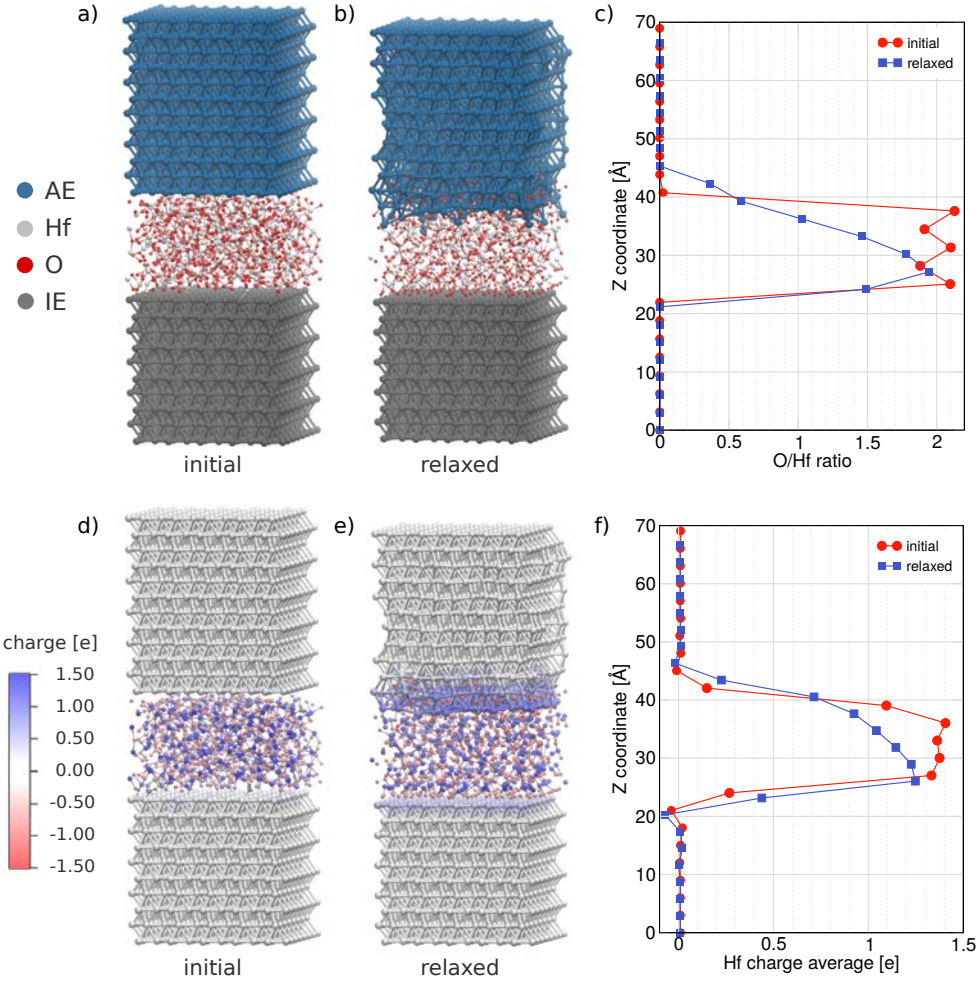

Figure 6.3: Atomic structure of MIM-1 at a) the initial state and b) after the interface relaxation. c) Stoichiometry profile of the cell along the z axis at time 0 and 100 ps. d) Initial charge distribution. e) Final charge distribution. f) Hf charge profile along the z coordinate for the initial and relaxed structures. The snapshots were generated with the VMD software [111, 112].

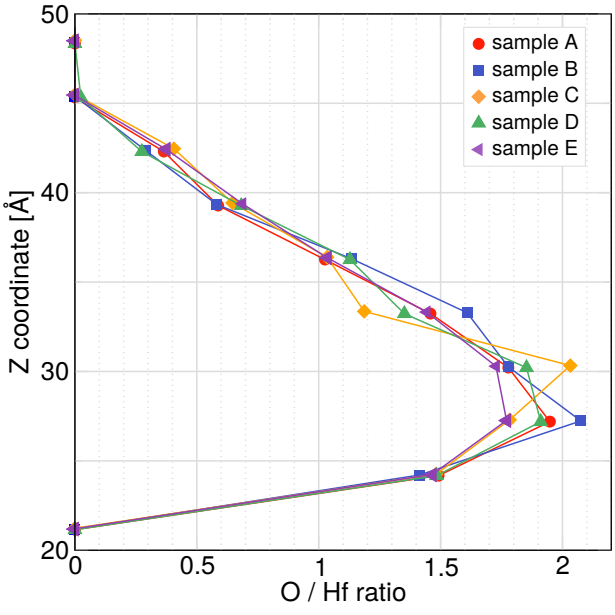

Figure 6.4: Stoichiometry profiles along the oxide thickness at the end of the interface relaxation.

in Hf ions during the switching of the devices, we characterized it through the oxygen coordination of Hf atoms, as explained in Sec. 6.1.3. The results are shown in Figure 6.5a) and Figure 6.5b) with the snapshots corresponding to the initial and fully relaxed state, respectively. In the images, the color code ranges from blue representing Hf atoms with no oxygen neighbors (i.e. 100% metallic hafnium) to red representing Hf atoms with at least 7 oxygen bonds (i.e. fully oxidized). Before relaxation, Hf atoms from the oxide are mostly seven-fold coordinated, as expected for the HfO_2 structure. When the interface relaxation occurs, this value reduces, generating high concentration of Hf with metallic behavior, mainly at the active electrode interface. This trend agrees with DFT calculations, which predict that the formation energy of an oxygen vacancy decreases towards the interface, suggesting that it is thermodynamically more favorable remove an oxygen atom from the interface region than from the bulk region [113]. In Figure 6.5c) we display only Hf atoms with coordination equal or lower than 5, considered as metallic. The representation of dynamic bonds shows that the interface relaxation does not lead to formation of the CF.

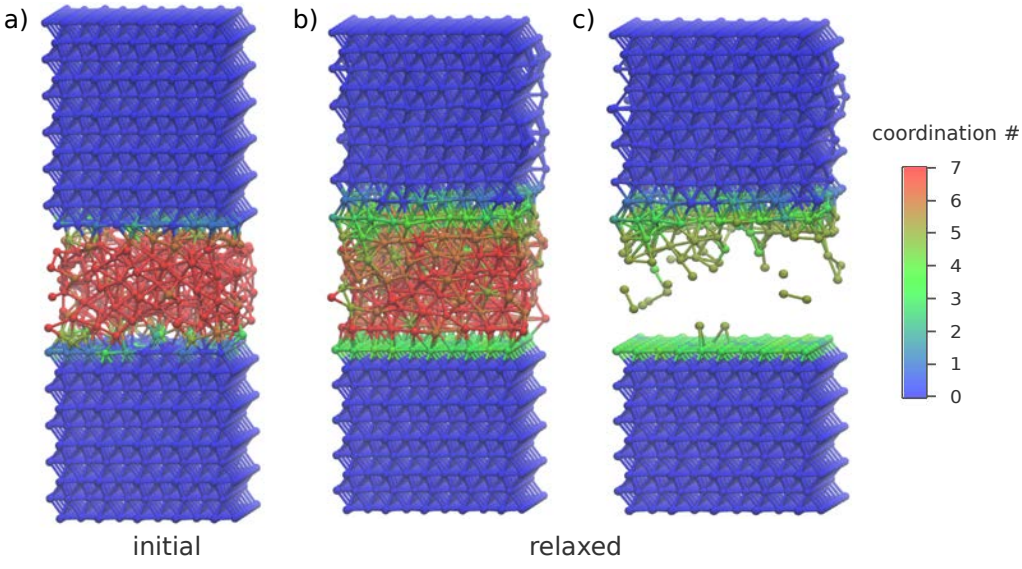

Figure 6.5: Snapshots of Hf atoms colored according their coordination number for a) the initial structure, b) the relaxed structure and c) the relaxed structure plotting only undercoordinated Hf atoms. The snapshots were generated with VMD software [111, 112].

6.3 Device operation

When operating RRAM cells, the resistivity of the oxide layer change between a HRS and LRS. The transition from the HRS to the LRS is called SET operation, and the reverse transition is called RESET. However, in order to enable a reversible change between these two states, the devices normally require an initial and irreversible process called electroforming, or simply FORMING, which is basically a current-controlled breakdown of the pristine highly resistive oxide layer [92, 114, 115]. In this section we present MD simulation of these three processes, aimed at contributing with an atomistic description of the mechanisms involved.

6.3.1 Forming

Simulating the forming process requires the application of an external field between the metallic electrodes. In the experiments, the magnitude of the field applied during the forming depends on the original amount of oxygen vacancies, i.e. the

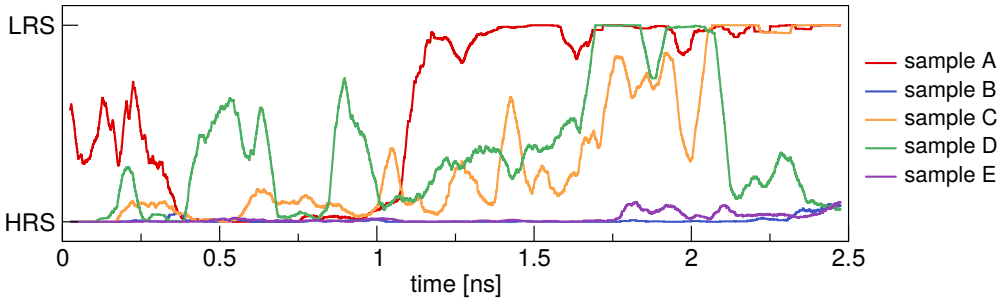

Figure 6.6: Switching dynamics of the five samples considered, performed through cluster analysis of conductive Hf atoms, using a cutoff of 3.9 Å. The switching state evolution has been averaged using a moving window of 0.02 ns for clarity

stoichiometry of the HfO_x oxide layer. For HfO_2/Hf cells, the values are few tens of meV/Å (0.04 eV/Å [98], 0.06 eV/Å [93]). We simulated the forming process by applying 4V difference between the electrodes, which corresponds to an external field equivalent to 0.2 eV/Å. The voltage was applied in isochoric-isothermal MD simulations (NVT ensemble) at 300 K, following the scheme described in Sec. 6.1.4. The voltage was chosen high enough to ensure the formation of the CF occurs within timescales accessible to MD simulations. The active electrode was polarized positively, with a potential of +2V, in order to attract the oxygen atoms, while the inert electrode was set to -2V. As it can be seen in Figure 6.6, from a total of five samples generated independently, only three were able to switch, and two formed a stable filament within the time considered of 2.5 ns. The relatively low switching probability of the simulated cells is related to the small cross section considered, compared to the real experimental values.

Figure 6.7a) displays snapshots of atomic charges in one of the samples that demonstrates a strong switch (sample A) at different stages of the forming. Here, it can be seen the active electrode further oxidizes with the applied potential, generating more oxygen vacancies in the oxide layer. Figure 6.7b) shows snapshots of Hf coordination, with value equal or lower than 5, corresponding to the conductive Hf atoms. Figure 6.7c) shows the electronegativity of metallic Hf assigned by EchemDID. Before the forming, EchemDID propagates the electronegativity over the metallic atoms according to their connectivity with the electrodes. When the

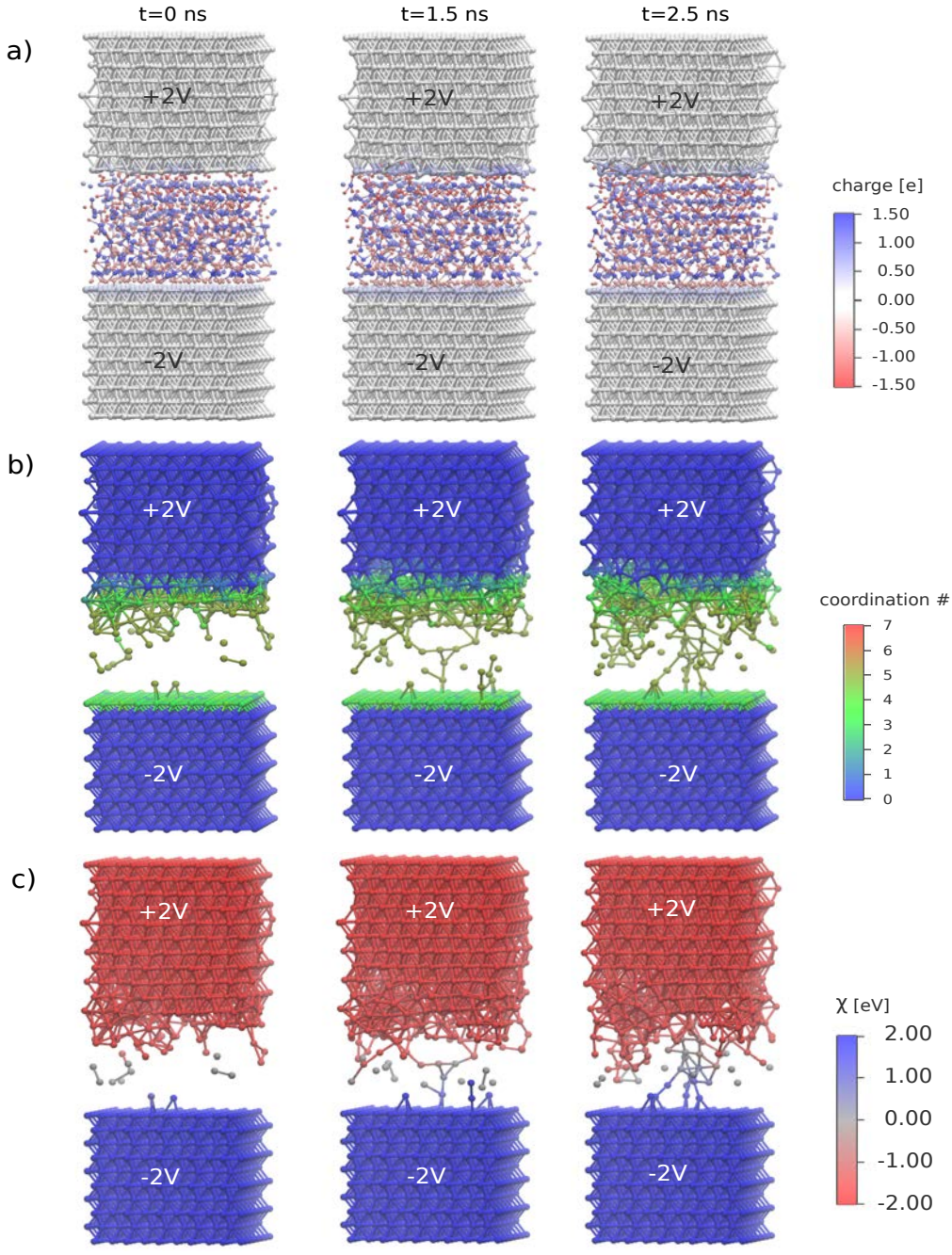

Figure 6.7: Snapshot of the a) atomic charges, b) coordination number of Hf atoms, and c) potential of Hf atoms, at the beginning (t=0 ns), just when the filament is fomed (t=1.5 ns) and at the end of the simulation (t=2.5 ns). The snapshots were generated with VMD software [111, 112].

CF forms, the electronegativity of the metallic ions varies linearly, according to the atomic position between the two electrodes. These plots provide an atomistic picture of the evolution of the CF, that starts as a single-atom chain, just after the switch, and grows while the potential is kept applied. According to the results, the forming starts from the active electrode towards the inactive electrode, while the narrowest constriction is observed near the inactive interface. These findings agree with the quantum point contact model, which states the CF consists of an atomic size chain, or constriction, that behaves as a quantum wire [116].

Discussion of the forming mechanism

In VCM cells two different forming mechanisms have been considered in literature over the last years [117]. The first one postulates the generation of anti Frenkel-pairs (an interstitial oxygen O_i and an oxygen vacancy V_O) when an external electric field is applied, followed by the migration of the interstitial oxygen towards the active electrode. In this model, oxygen vacancies are assumed to be immobile, providing conduction by trap-assisted tunneling. The other mechanism postulates the vacancies are generated as result of an oxygen exchange reaction at the anode (active electrode), followed by the migration of the oxygen vacancy to cathode (inert electrode). In this case, the vacancy migration occurs through successive oxygen exchanges between the empty space generated by the reaction with the active electrode and the adjacent oxygen atoms.

The mechanism based on anti-Frenkel pair generation/recombination is not applicable to amorphous structures due to the reasons explained in 6.1.3. Besides, MD simulations performed on cubic and monoclinic HfO_2 have demonstrated that this mechanism is neither possible in crystalline structures due to the considerably high electric field required to create O_i-V_O pairs (only sporadic defects are generated at 0.3 eV/Å) and short recombination times (1 to 4 ps) [118].

We analyzed the forming mechanism by plotting the migration of oxygen atoms as a function of time for two different kind of simulations: in one case the electronegativity was actualized periodically as described in Sec. 6.1.4, and in the other case, the electronegativity was modified only in 100% metallic Hf at the beginning and maintained fixed during the rest of the simulation. The aim of this last procedure is to maintain fixed the AE/HfO_2 interface during the forming process. The migration profiles for both cases are displayed in

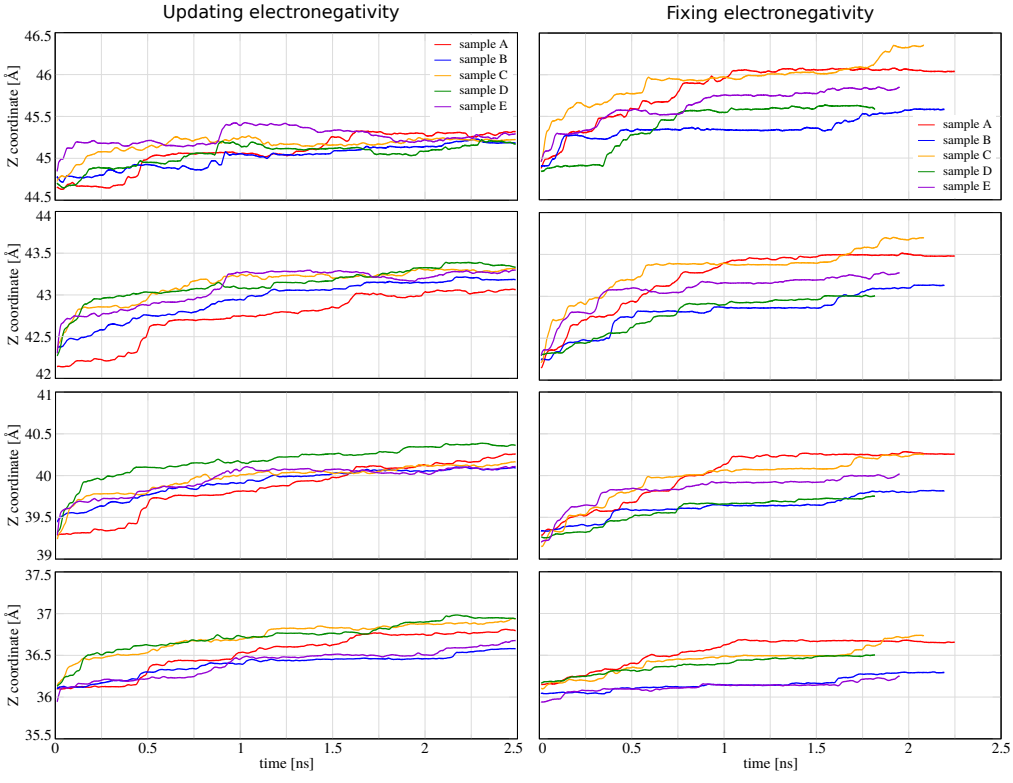

Figure 6.8: Center of mass of different oxygen layers along the dielectric thickness as a function of time.

Figure 6.8. For simulations with the electronegativity fixed, the plots display abrupt oxygen displacements that start at the upper oxygen layer, and are followed by displacements of the subsequent layers. Visual inspection of the trajectories shows that each abrupt displacement in the upper oxygen layers corresponds to a large displacement in z of a single oxygen atom. This result demonstrates that oxygen atoms from the first layer that diffuse towards the AE leave behind empty spaces that are occupied by oxygen atoms from the second layer, producing in this way a cascade of displacements that attenuate as the distance to interface increases. For the case where the electronegativity updates during the simulation, the results are quite similar. However, since there are Hf atoms from the oxide that become metallic as the filament evolves, the potential propagates inside the oxide, favoring the oxygen migration in the deeper layers. Our results are a clear evidence that the forming mechanism operating in amorphous HfO_2 is the oxygen exchange across AE/HfO_2 interface.

6.3.2 Reset process

To understand the nature of the reset mechanism, we ran simulations under different voltages and temperatures. We used Sample A for the studies since this is the MIM structure that demonstrated the stronger switch. Depending on the temperature imposed on the system, we observed bipolar or unipolar reset, both mechanisms will be explained bellow.

Reset at 300 K

The switching behavior for different applied voltages at 300 K is presented in Figure 6.9a). The results show that the filament remains stable while maintaining the forming polarity, i.e. positive potential in the AE and negative potential in the IE. When the voltage is removed, the filament destabilizes and, finally, it dissolves when the polarity is reversed, indicating a clear bipolar behavior.

The oxygen migration profiles shown in Figure 6.11 demonstrate that the motion of oxygen atoms along the field direction is almost negligible; only simulations with voltages of +4V (-4V) showed small displacements towards the AE (IE). These results indicate that the oxidation produced during the forming process is completely irreversible, and the filament rupture must occur by a reorganization

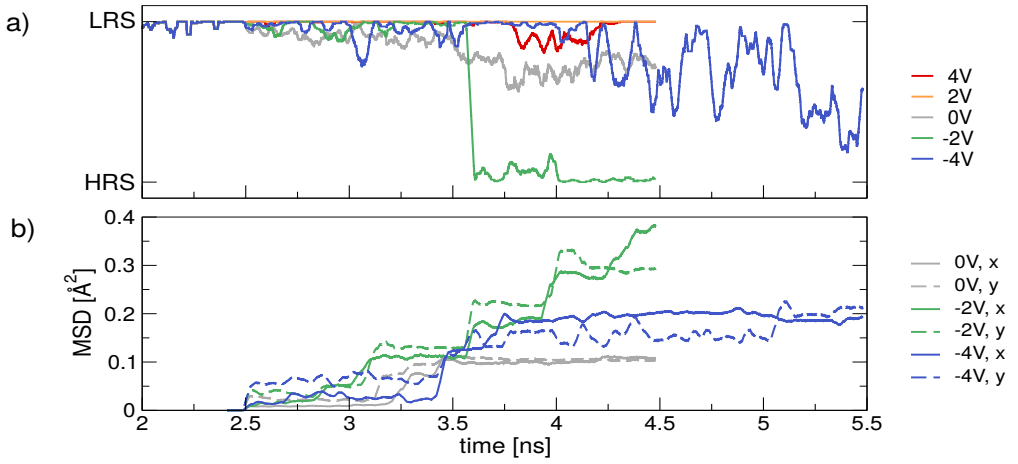

Figure 6.9: a) Switching dynamics of sample A under different voltages at 300 K, performed through cluster analysis of conductive Hf atoms, using a cutoff of 3.9 Å. The switching state evolution has been averaged using a moving window of 0.05 ns for clarity. b) Mean square displacement (MSD) of oxygen atoms in the constricted region (with z between 27 and 40Å)

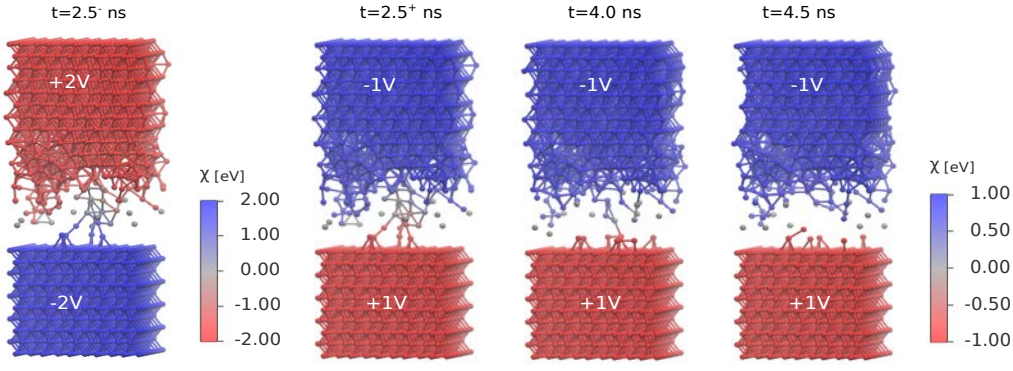

Figure 6.10: Snapshot of the reset process colored by potential of Hf atoms, for different times. The snapshots were generated with VMD software [111, 112].

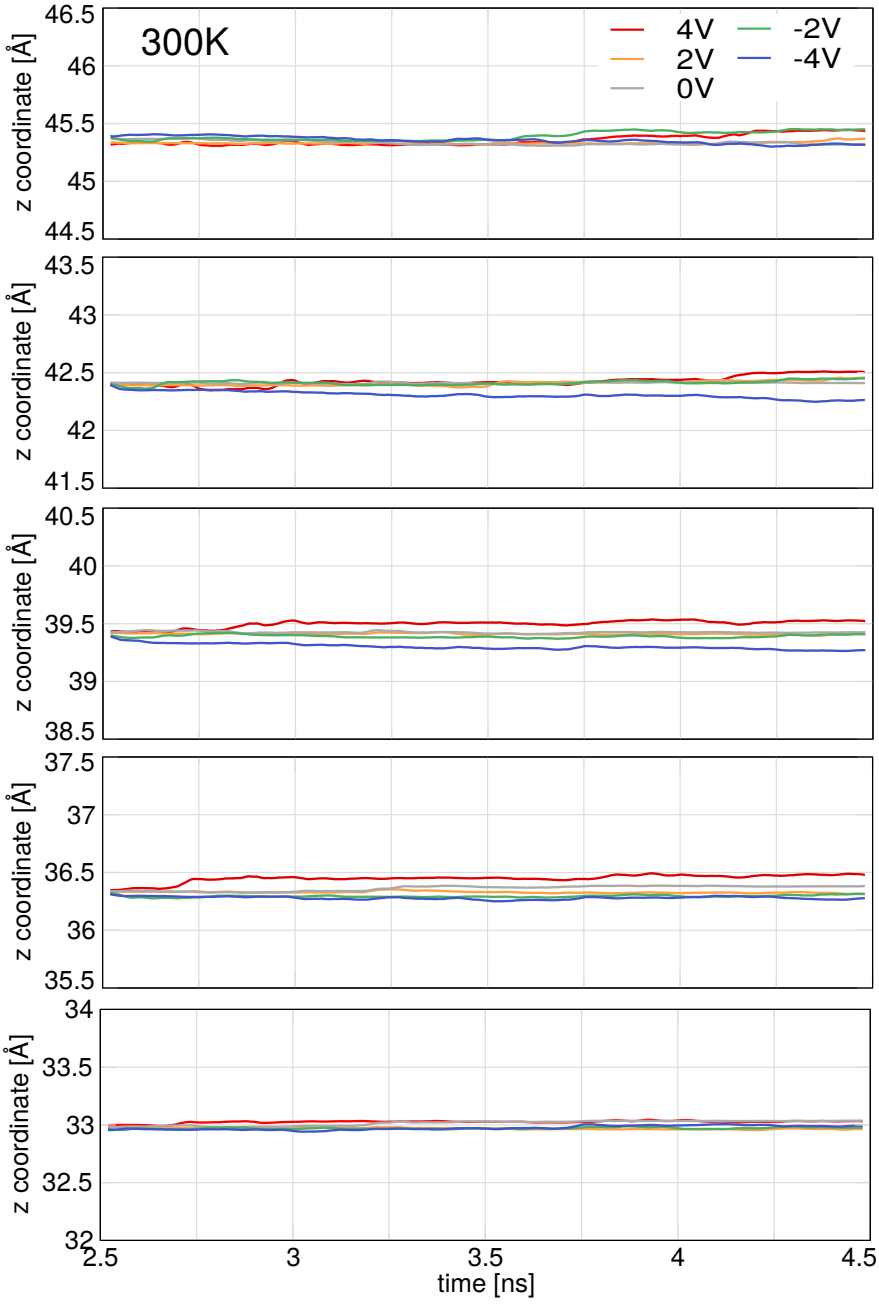

Figure 6.11: Center of mass of different oxygen layers along the dielectric thickness as a function of time for reset at 300 K.

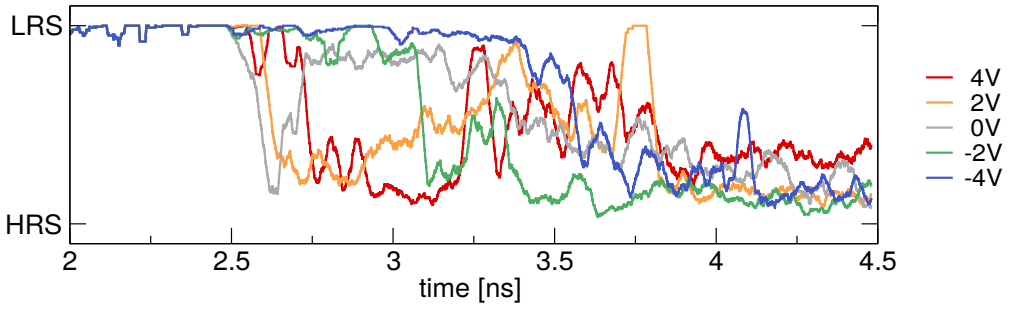

Figure 6.12: Switching dynamics of sample A under different voltages at 400 K, performed through cluster analysis of conductive Hf atoms, using a cutoff of 3.9 Å, and taking moving average of 0.05 ns.

of the oxygen atoms in the xy plane. Figure 6.9b) displays the xy mean square displacements (MSD) of the oxygen atoms in the constricted region (oxygen with z coordinate between 27 Å and 40 Å), showing a complete correlation with the filament stability. Based on the snapshots shown in Figure 6.10, we infer that the driving force for the localized xy oxygen migration is the positive potential (negative electronegativity) propagated over the filament that induces a local oxidation.

Reset at 400 K

When the temperature of the whole system is increased up to 400 K, the filament destabilizes and breaks in all cases, as it is shown in Figure 6.12. This is true even when applying a bias with the same forming polarity, and further oxygen migration towards the AE is observed (Figure 6.13). This is because increasing the temperature of the system favors diffusion, not only in the field direction, but also in the xy directions, which is the main cause of the filament dissolution, as observed previously for samples at 300K.

Our findings are in agreement with experiments where the current compliance is released during reset to produce the filament rupture by Joule heating [92], suggesting that reset in bipolar HfO_2-based cells can also be induced by thermal activation. Similar results where observed in bipolar TiO_2-based RRAM cells, where by setting a large compliance current value, the cell turned to unipolar switching [119].

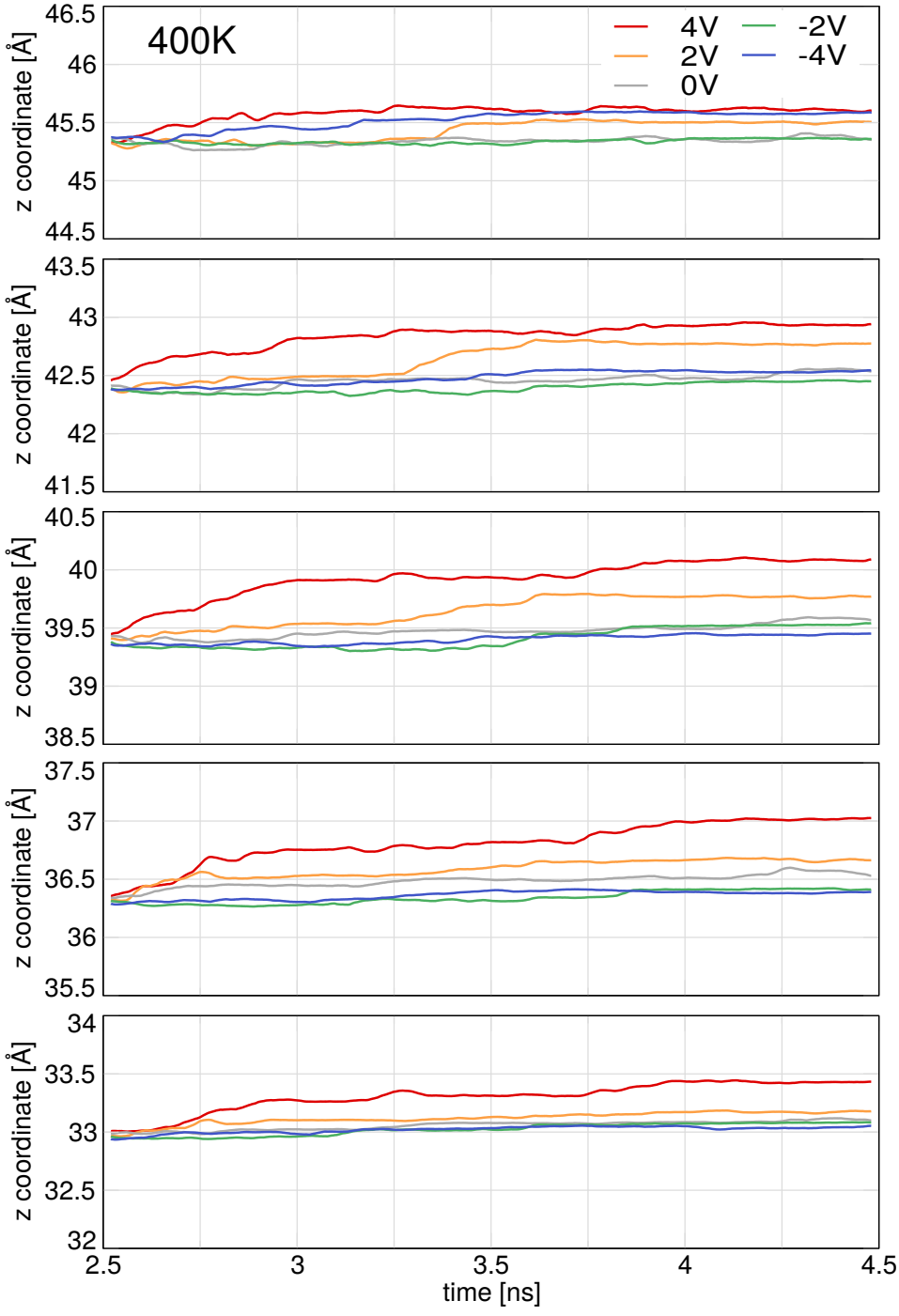

Figure 6.13: Centre of mass of different oxygen layers along the dielectric thickness as a function of time for reset process at 400 K.

6.3.3 Set process

The set was simulated by reversing again the polarity of the external field. In this case 4V were applied between the metallic electrodes to ensure that the filament formation occurs in time accessible to the dynamics. Since the characteristic time for oxygen jumps inside the oxide is relatively slow (∼0.5 ns), the set was simulated at 300 K and increasing slightly the temperature up to 325 K in order to see the filament formation in shorter times. In both cases, we used the MIM structure obtained after the bipolar reset at -2V and 300 K, which demonstrates a complete dissolution of the conductive filament.

The switching dynamics and the mean square displacement are shown in Figure 6.14, and the snapshots for different set times are displayed in Figure 6.15. From these results, it can be seen that for 325 K the filament start forming after 0.5 ns, and it remains stable during the rest of the simulation. Again, it was observed that there is no preferential migration in the field direction, as can be verified in the COM displacements of oxygen layers in Figure 6.16, which demonstrate low migration in z axis (below 0.5Å for T=325 K). Hence, the set process must occur through a reorganization of oxygen atoms in the xy plane (i.e. without involving redox process with the active electrode and increasing the oxide thickness), leading to a new filament.

The resulting filament differs from the initial one, obtained after forming process. However, since the cross section of the device considered here is relatively small, this finding is not indicative that the filament might form in a different region during the successive set.

6.4 Summary

In summary, we generated substoichiometric HfO_x profiles obtained during the fabrication of RRAM cells by relaxing hafnium/hafnia interfaces. The relaxed samples were used to simulate the forming, reset and set processes under operating conditions, i.e. applying an external potential in the metallic electrodes. With these reactive simulations, it was possible to describe the redox processes responsible for the switching of the cell.

The dynamics of the oxygen vacancies was successfully visualized by plotting conductive hafnium atoms on the fly during the simulation. With this scheme,

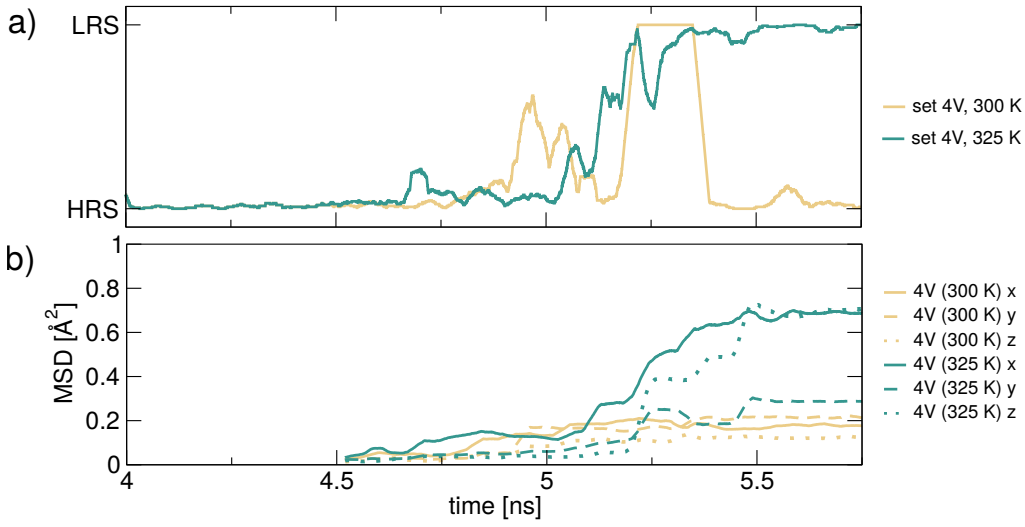

Figure 6.14: a) Switching dynamics of the set simulation at 4 V with temperatures of 300 K and 325 K. The starting structure corresponds to sample A after reset at 2 V and 300 K. See caption of Figure 6.9 for the description of how we obtain the switch curve. b) Mean square displacement of oxygen atoms with z between 27 and 40 Å.

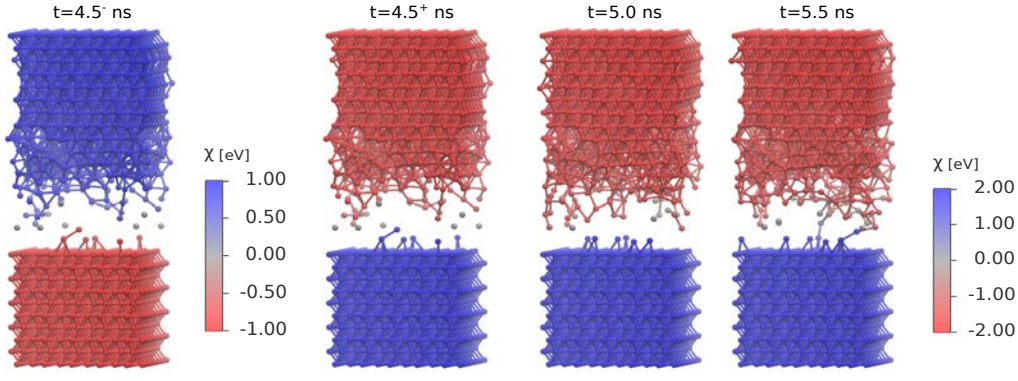

Figure 6.15: Snapshot of the set process colored by potential of Hf atoms for different times. The snapshots were generated with VMD software [111, 112].

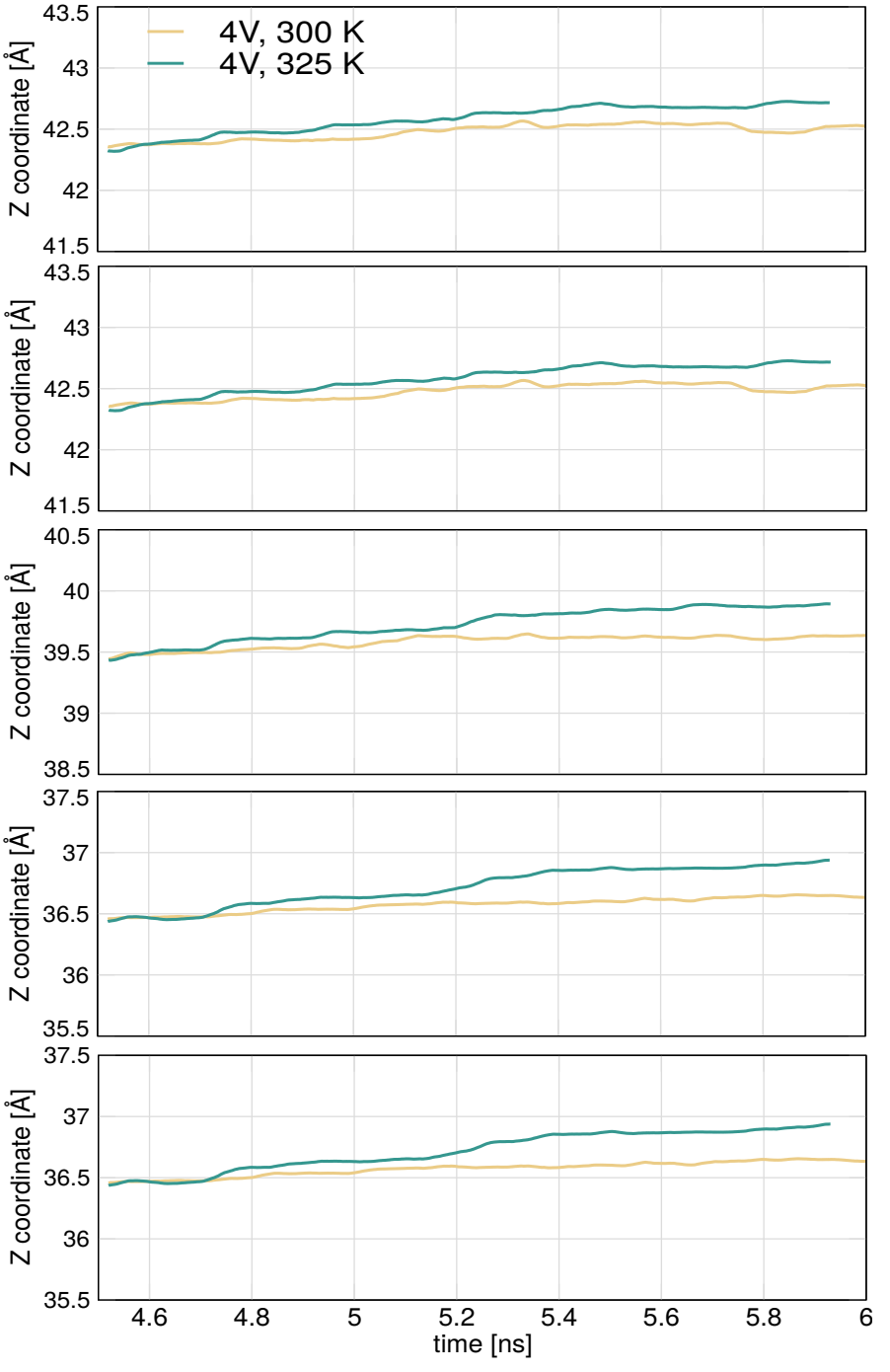

Figure 6.16: Center of mass of different oxygen layers along the dielectric thickness as a function of time for set process at 300 K and 325 K.

we identify the formation and rupture of an atomic conductive filament. Based on this dynamics, we propose an atomistic mechanism for the forming process in nanoscaled cells, consisting in a cascade of oxygen displacements initialized at the interface, similar to oxygen exchange mechanism proposed previously in experiments. We also found that the reset and set processes occur through a local reorganization of oxygen atoms in the filament region, without involving oxygen migration towards the active or inactive electrode. These simulations provide new insights in the switching mechanism operating in nanoscaled HfO_2 based cells.

Chapter 7

Oxygen vacancy formation and migration in monoclinic HfO_2

The previous chapter was dedicated to describe the microscopic mechanisms involved in the operation of RRAM cells using molecular dynamics technique. To complement these studies, besides the dynamics of the oxygen vacancies diffusion, it is also important to know the energies associated to the formation of oxygen vacancies and the activation barriers for their migration.

The formation and migration of neutral and charged oxygen vacancies in HfO_2 has been extensively studied from the computational point of view in monoclinic [120, 121, 122, 123, 124] and amorphous [125] structures. However, these studies were made at zero electric field, far from the operating conditions that we used previously, and of course, applied in experiments. In the case of aperiodic systems with periodic boundary conditions (PBCs), the application of net charge (introducing a charge compensating background) is non-trivial because the electric dipole in such case is ill-defined since it depends on the center of charge distribution, or which is the same, the position of the structure [126, 127]. This gives rise a problem when trying to study charged systems under electric fields using traditional DFT schemes.

Recently, the effect of the electric field on the diffusion barriers of oxygen vacancies and interstitial oxygen ions in oxide structures has been studied using the Berry phase operator, within the modern theory of polarization [128, 129, 130]. Other studies propose introducing a slab model with electron-accepting dopants

in the surface [131], to induce electron transfer from the oxygen vacancy to the dopant atom, and avoid using systems with net charge.

A much simpler alternative to study the combined effect of net charge and electric field could be the use of Poisson solvers that do not apply PBC in the aperiodic direction. To the best of our knowledge, there are no previous reports of these studies in literature. Therefore, the objective of this chapter is not only provide further validation on the vacancy migration mechanisms described in Chapter 6, but also propose a new scheme to study charge migration in slabs under an external electric field.

7.1 Methods

7.1.1 Computational details

DFT calculations have been performed with VASP [27] code, based on plane waves, and CP2K [29] code, which is based on a combination of Gaussian functions and plane waves (GPW). With VASP, we obtained highly converged calculations used as a reference for the activation and formation energies in periodic systems, and for comparing with other theoretical results, while CP2K was used to perform non periodic calculations including the effect of electric field. In both cases, the exchange correlation functional was described with Generalized Gradient Approximation (GGA) using the Perdew-Burke-Ernzerhof (PBE) parametrization [24]. The cutoff energy for the plane waves expansion was set to 400 eV and 816 eV for VASP and CP2K calculations, respectively. In the case of CP2K code, a double-ζ Gaussians basis set was used [132].

The calculations were performed on 324-atom monoclinic HfO_2 supercells (3×3×3 unit cells), with converged lattice parameters of a=5.11 Å, b=5.19 Å and c=5.31 Å (a=5.14 Å, b=5.16 Å and c=5.30 Å) for VASP (CP2K), as can be seen in Figure 7.1. We focused on crystal structures because they are computationally cheaper than amorphous structures, which require many more unit cells to reproduce the properties of the system. In order to apply an electric field the system must be set as a slab, so a vacuum of 15Å was added to the 3×3×3 supercell in the c-axis.

The Brillouin zone was sampled with 2×2×2 (2×2×1) $\mathbf{k}$ points for bulk (slab) m-HfO_2 calculations. All structures were relaxed until the force on each atom

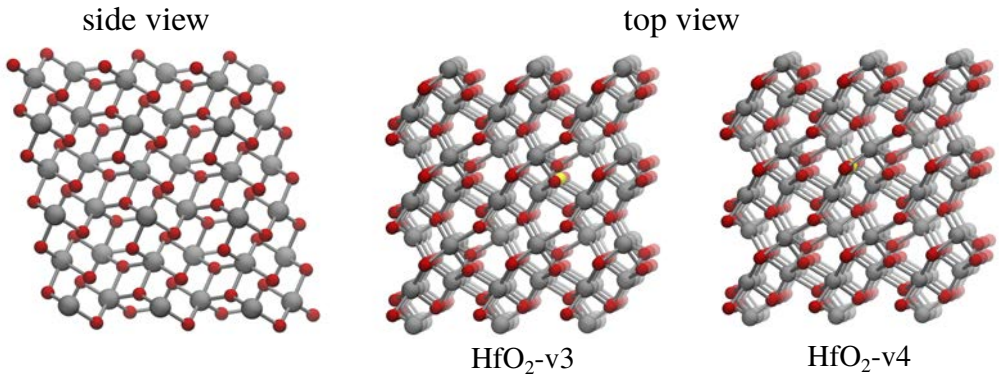

Figure 7.1: Structure of monoclinic HfO_2 with an oxygen vacancy in 3-fold (v3) and 4-fold (v4) coordinated sites. Red: oxygen atoms, gray: hafnium atoms and yellow: oxygen vacancy.

became lower than 0.02 eV/Å.

7.1.2 Modeling charged systems under external field

Performing calculations of slabs with large dipole moment or external electric field requires the implementation of dipole corrections [126, 127] to avoid interaction between periodic images, where the electric dipole is calculated as:

$$\mathbf{d} = \int (\mathbf{r} - \mathbf{R}_c)\rho(\mathbf{r})\ d\mathbf{r} \tag{7.1}$$

Here $\mathbf{R}_c$ are the coordinates of the center of the charge distribution, which is chosen as the reference point for computation of the dipole. Although these corrections work properly for neutral systems, they are not suitable for systems with net charge since for this case the electric dipole would depend on the center of the charge distribution $\mathbf{R}_c$. Therefore, to avoid dealing with dipole corrections, we decided to study the movement of ions or charged defects under the effect of an external electric field using a DFT code that supports Poisson solvers without PBC, such as CP2K. For the HfO_2 slab calculations, the electrostatics was solved applying PBCs in the xy directions, while the non-periodic direction and electric field was set along the z axis.

7.1.3 Nudged Elastic Band Method

A common problem in theoretical chemsitry and condensed matter is the identification of a minimum energy path (MEP) for the transition from a stable configuration to another one in a given system. The maximum energy along the MEP, corresponding to the saddle point in the energy profile, gives the activation energy (AE) barrier of the process involved. One of the most used methods for finding MEPs between an initial and a final state is the nudged elastic band (NEB) method [133]. The basic idea of the NEB method consist of generating a chain of images of the system (also called replicas or states) between the initial and final configurations, and optimize them all at the same time using two forces: the gradient of the potential in the perpendicular direction to the reaction coordinate, which brings the band to the MEP, and an spring force that controls the spacing between images along the band:

$$\mathbf{F}_i^{NEB} = -\nabla V(\mathbf{R}_i)_\perp + \mathbf{F}_{i\|}^s \tag{7.2}$$

where $\mathbf{R}_i$ are the coordinates for an image i. The perpendicular component of the true force,$\nabla V(\mathbf{R}_i)_\perp$, is calculated as:

$$\nabla V(\mathbf{R}_i)_\perp = \nabla V(\mathbf{R}_i) - \nabla V(\mathbf{R}_i)_\| \quad , \tag{7.3}$$

and the spring force, $\mathbf{F}_{i\|}^s$, is given by:

$$\mathbf{F}_{i\|}^s = k[(\mathbf{R}_{i+1} - \mathbf{R}_i) - (\mathbf{R}_i - \mathbf{R}_{i-1})] \cdot \hat{\tau}_{i\|} \tag{7.4}$$

with k being the spring constant and $\hat{\tau}_{i\|}$ the unit vector in the direction tangent to the reaction path. In order to decompose the forces into parallel and perpendicular components, it is necessary to estimate the tangent to the path at each image, and every iteration during the minimization. In improved NEB schemes, the parallel direction vector, $\hat{\tau}_{i\|}$, is defined as the tangent between the image i and the image with higher energy [134].

In order to obtain a rigorous convergence of saddle point in the MEP, a modified version of NEB, called climbing image NEB (CI-NEB) [135] can be used. In this method the image with the highest energy is identified and its potential is moved up to make the image climb up along the elastic band. Besides, this scheme also introduces variable spring constants to increase the density of images near the top of the MEP.

Example: activation barriers for NH_3 flipping

To validate the scheme explained in Sec. 7.1.2, we performed NEB calculations in a test system, consisting on the flipping of a negatively charged ammonia molecule (NH_3^-). Figure 7.2 shows the activation barriers obtained with VASP code (top), which implements full periodic boundary conditions, and CP2K (bottom), without PBCs at all.

The calculations for the neutral molecule (red curve) predict an activation barrier of 0.21 eV (0.22 eV) for VASP (CP2K), which is in agreement with the non-relativistic, no zero-point motion result of 0.22 eV obtained by coupled-cluster theory [136]. It is to be noted that, when the non-relativistic, no zero-point motion approximations are released, coupled-cluster theory [136] obtains a result of 0.25 eV, in perfect agreement with the experimental results [137]. When the molecule is negatively charged (orange curve), the barrier increases up to 0.25 and 0.27 eV for VASP and CP2K, respectively.

If an external field of 0.1 eV/Å is applied along the z axis to the charged molecule with PBCs, the barrier remains almost the same and so do the initial and final energies, demonstrating that there is a failure when computing the effect of field. Besides, the energies of the images depend on the center of charge distribution defined for the dipole correction, as can be seen when comparing turquoise and brown curves.

In the case of calculations without PBC, the effect of the electric field modifies strongly the stability of the initial structure with respect to final, lowering the barrier to 0.23 eV for the forward process, and increasing it to 0.32 eV for the reverse process. These energies are completely independent on the position of the molecule. Since the difference in the z coordinate of the nitrogen atom between the initial and final state is 1.01 Å, we would expect an energy difference of 0.101 eV, but instead we obtain 0.09 eV. The deviation can be explained considering the screening of the molecular dipole when it points aligned or antialigned with the field.

7.2 Vacancy formation energies

During the fabrication of RRAM devices, it is common to perform a high-temperature annealing (up to ∼1000 K) to crystallize the HfO_2 to the monoclinic

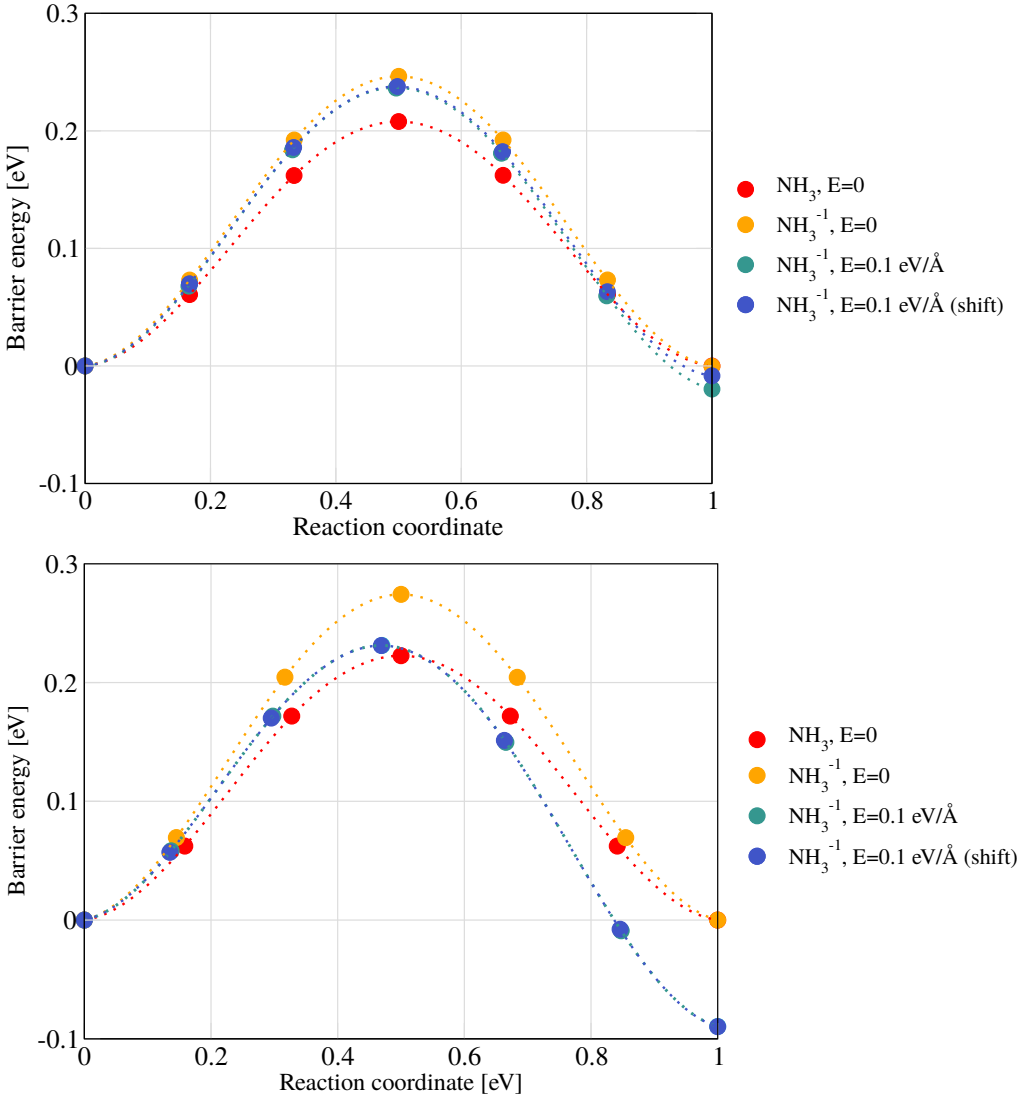

Figure 7.2: Activation barriers for ammonia flipping with different charge states (0 and -1), top: calculated with VASP and applying dipole corrections with the center of charge distribution placed on the N atom, or on the H atoms(shift=0.75), and bottom: calculated with CP2K without PBC, since we do no apply dipole corrections, we shifted the molecule coordinates in the field direction.

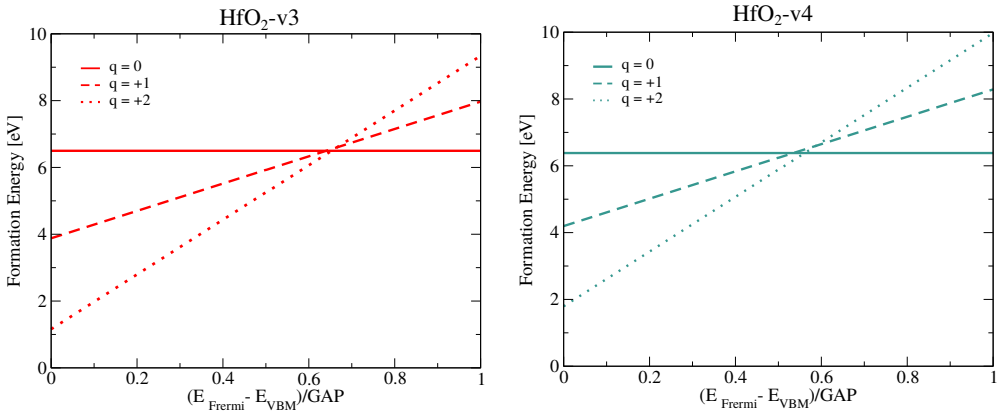

Figure 7.3: Formation energies as a function of the Fermi level for threefold (left) and fourfold (right) coordinated oxygen vacancies in m-HfO_2 at different charge states, calculated with VASP.

phase (m-HfO2), which is the most stable phase below ∼2000 K. During this process, high concentration of oxygen vacancies are generated in the crystal structure, so it is important to know the energy associated with this process and the most stable charge states.

The formation energy (E_{form}) of single oxygen vacancy were calculated through the following equation:

$$E_{form} = E_{\mathrm{HfO_2\text{-}v}} + 1/2\ \mu_{O_2} + q\ (E_F + E_{VBM}) - E_{\mathrm{HfO_2}} \tag{7.5}$$

where the oxygen vacancy can be a threefold (v_3) or fourfold (v_4) coordinated site with charge (q) equal to 0, +1, +2. The energies $E_{\mathrm{HfO_2\text{-}v}}$ and $E_{\mathrm{HfO_2}}$ correspond to the defective and pristine monoclinic hafnia structures, respectively. E_F is the Fermi level imposed externally, and VBM the valence band maximum of the defective structure. The oxygen chemical potential μ_{O_2} was obtained through a spin polarized calculation of an isolated oxygen molecule. For the case of systems with net charge, Madelung corrections were applied to discount interaction between periodic images [138].

The resulting energy plots are presented in Figure 7.3, showing a detailed description of each charge state, and Figure 7.4, where only the most stable charge state as a function the Fermi energy is displayed, for VASP and CP2K calculations. As can be seen in Figure 7.4 the thermodynamically preferred

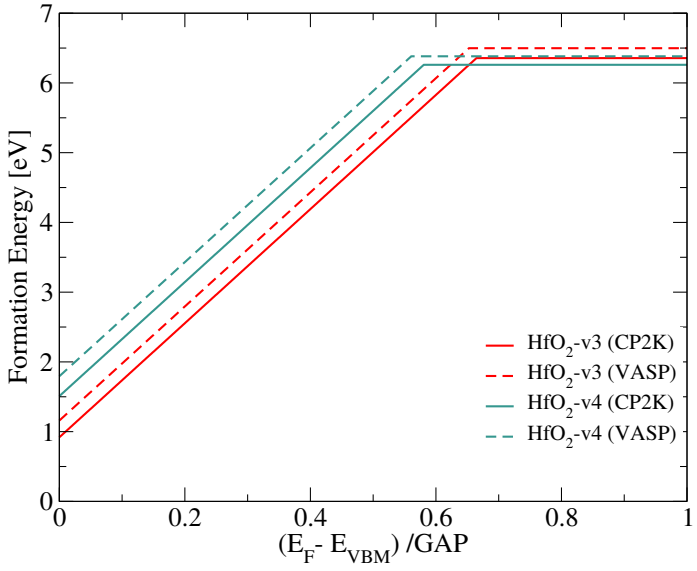

Figure 7.4: Oxygen vacancy formation energies as a function of the Fermi level for the most stable charged states (q=+2 and q=0) calculated with VASP and CP2K.

System	VASP	CP2K	Ref. [120] (VASP w/o Madelung)
HfO_2-v3-q0	6.50	6.36	6.76
HfO_2-v3-q1	3.78	—	3.98
HfO_2-v3-q2	0.76	0.52	0.81
HfO_2-v4-q0	6.38	6.26	6.63
HfO_2-v4-q1	4.10	—	4.25
HfO_2-v4-q2	1.40	1.11	1.44

Table 7.1: Formation energies in eV calculated with VASP and CP2K without including Madelung corrections.

charge state for E_F near the VBM is +2, in both threefold and fourfold vacancies, while for high E_F, the most stable state is 0, in agreement with previous results [121, 120]. The transition from +2 to 0 takes place at 3.41 eV and 2.95 eV above

the VBM in HfO_2-v3 and HfO_2-v4 structures, respectively, when considering experimental band gap for mHfO2 of 5.25eV [139].

Finally, the energies calculated with VASP and CP2K at $E_F = E_{VBM}$ (without considering Madelung corrections) are compared with literature in Table 7.1. In the table it can be seen that the lowest formation energy is obtained for the threefold coordinated vacancies with charge +2, hence we used this structure for further studies of the activation barriers.

7.3 Vacancy migration energies

As mentioned in Chapter 6, during the normal operation of RRAM devices, the dielectric layer is subject to an external electric field that induces the migration of oxygen atoms (or their respective vacancies), facilitating the creation of new defects. Hence, understanding the effect of the electric fields on the activation barrier for the vacancy diffusion, is fundamental to complement our previous studies.

The activation barriers were calculated for the diffusion of an oxygen vacancy along the *c*-axis, from a threefold coordinated site to an equivalent adjacent point, as can be seen in Figure 7.5. The values obtained for neutral and charged defects in HfO_2 bulk are displayed in Figure 7.6, comparing the results calculated with VASP and CP2K codes. Here it can be seen a notably reduction of the barrier (from 1.76/1.83 eV to 0.84/0.76 eV) when the defect is doubly charged, in good agreement with other DFT calculations [124].

Finally, the activation barriers for the migration of neutral and charged defects under an external field of 0.05 eVÅ are showed in Table 7.2, where we also compare with the bulk values in order to verify our method. The results demonstrate only a small reduction of the barrier due to the external field. This might be indicative that the dipole moment induced by the migration of the charged defect could screen the external field, modifying in this way the energy of the images. Therefore, deeper studies must be performed on this systems considering different external field and charge states.

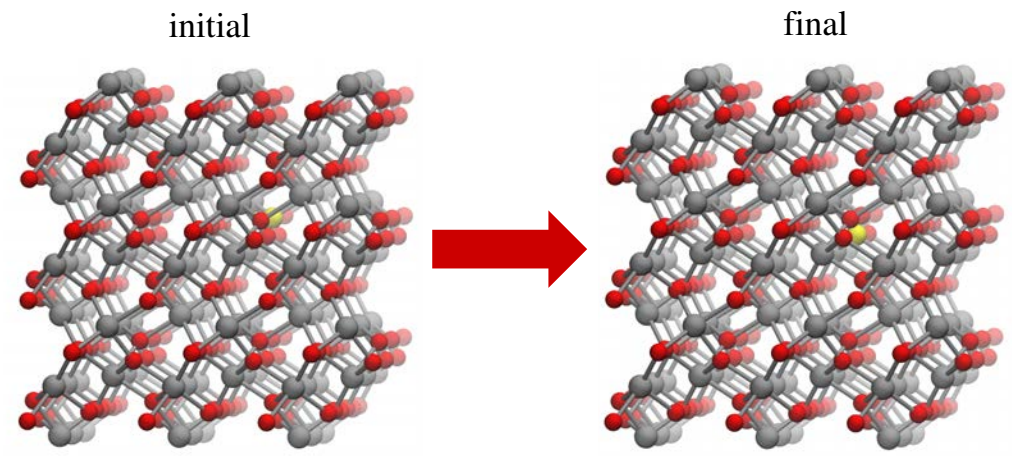

Figure 7.5: Initial and final structures of HfO_2 with a threefold coordinated oxygen vacancy. In the snapshots, Hf atoms are represented in grey, O atoms in red and the vacancy is plotted in yellow.

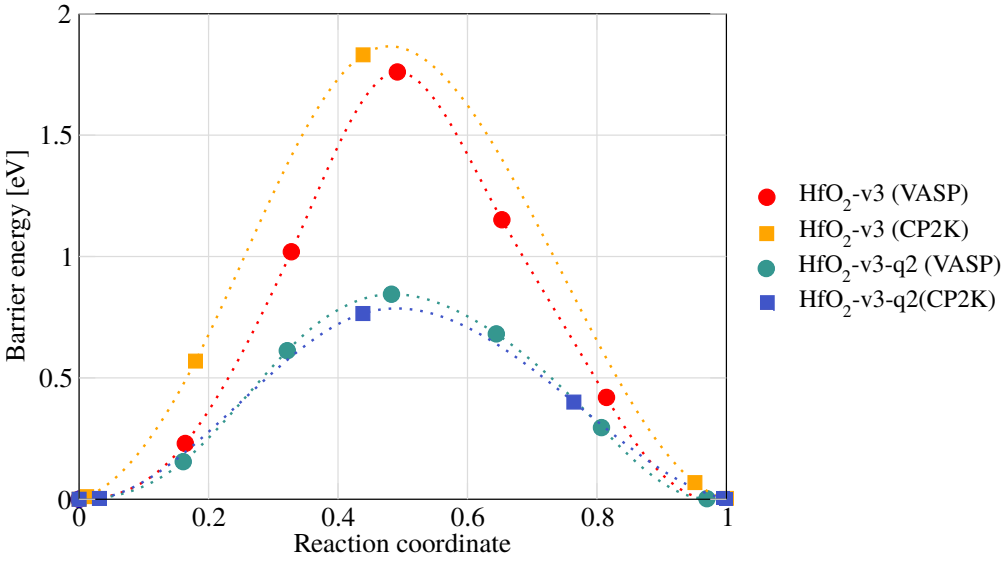

Figure 7.6: Activation barriers for the diffusion of a neutral or positively charged (+2) oxygen vacancies calculated with VASP and CP2K codes.

System	Barriers bulk [eV]			Barriers slab [eV]
	VASP	CP2K	Ref. [124]	CP2K
HfO_2-v3-q0 (E=0)	1.76	1.83	1.84	1.83
HfO_2-v3-q2 (E=0)	0.84	0.76	0.96	0.72
HfO_2-v3-q2 (E=0.05 eV/Å)	—	—	—	0.69

Table 7.2: Activation barriers corresponding to oxygen vacancies diffusion along the *c*-axis from a threefold coordinated site to an equivalent adjacent point, considering different charge states and the effect of an external electric field.

7.4 Summary

In this chapter we studied the application of an external electric field to systems with net charge through DFT calculations, in order to understand the migration of charged defects in monoclinic HfO_2, relevant for the operation of RRAM devices. We used a slab setup without periodic boundary conditions in the field direction to avoid implementing dipole corrections, which brings issues when the system has a net charge. The results where systematically compared with other slabs and bulk calculations using standard PBC, in order to validate our approach.

The activation barriers were successfully obtained for neutral and charged vacancies, demonstrating good agreement with values reported in literature. The same calculations performed under an electric field demonstrate a slight barrier lowering when the migration is in favor of the field. However more studies must be done in this direction to complete the understanding of the coupling between possible dipoles generated by the excess of charge and the field.

The scheme used in this work opens up an alternative to the use of the modern theory of polarization for the study of charged defects under external fields.

Chapter 8

Preliminary studies of MoS_2-based RRAM devices

Recently, nonvolatile resistive switching (RS) phenomena, commonly studied in oxide structures as described in Chapters 6, has been observed in a variety of 2D materials, such as transition metal dihcalcogenides (TMDs) [12, 140, 141, 142], hexagonal boron nitride (h-BN) [143], and others [144].

Among 2D TMDs, MoS_2 is again the most explored layered semi-conductor, with atomically thin memristors with planar [145, 146] and vertical [12, 140] geometries, as well as, transparent and flexible multilayer devices [147, 148] having been successfully fabricated. In the case of vertical cells, the atomically thin layer sandwiched between two electrodes is responsible for the change in the resistance, for this reason such devices are also known as atomirstors. Although there are some ideas as to the factors that might cause the low resistance state, the switching mechanism operating in this kinds of cells is still not clear. The most recent evidence indicates that the RS behavior could be due to Schottky emission in HRS and localized direct tunneling in LRS, probably because of the formation/rupture of CFs based on the sulfur vacancies [12, 149]. However, a detailed elucidation of the mechanisms at atomistic level is still missing.

In order to link the previous studies of MoS_2 structures and HfO_2-based RRAM cells, this chapter is dedicated to the study of RRAM cells based on atomically thin MoS_2 layers. Specifically, we performed DFT transport calculations of Au/MoS2/Au cells using different Au surfaces and MoS_2 phases (2H and 1T').

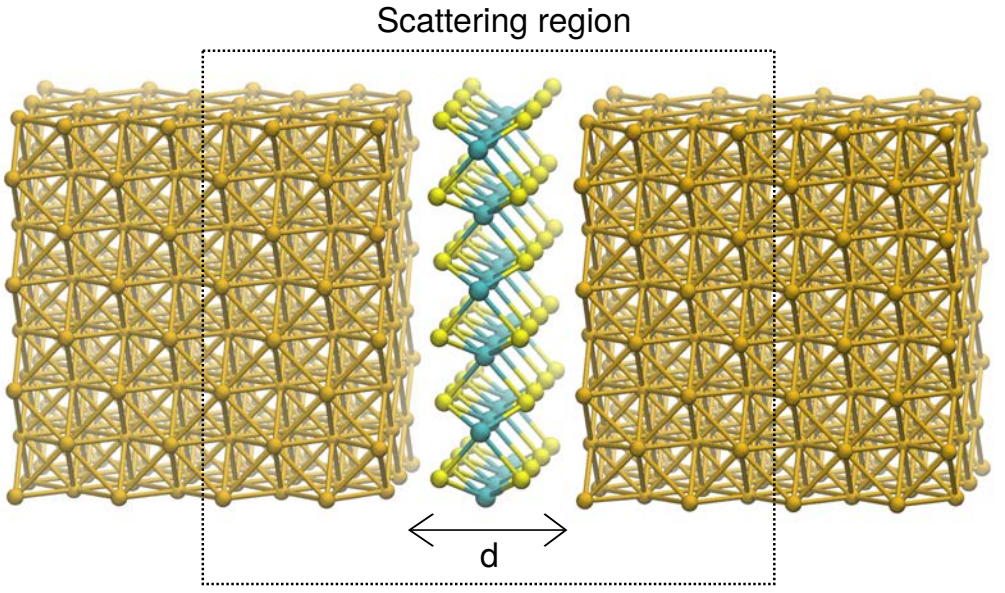

Figure 8.1: Device setup for transport calculations. The structure shown corresponds to a Au(100)-MoS_2-Au(100) stack.

To determine whether the resistance change is associated to vacancy defects, we also introduced simple and double sulfur vacancies in the MoS_2 layer. This work is still in development, and only preliminary results will be presented here.

8.1 Computational details

Density functional theory calculations were performed with the SIESTA code [28], using the generalized gradient approximation with the PBE functional [24]. The core electrons are described with norm-conserving pseudopotentials [68], while the valence electrons are explicitly treated with a double-ζ polarized basis set.

The MIM cells studied consist of Au-MoS_2-Au stacks, with different interface configurations. The details of the structures are summarized in Table 8.1. The lattice parameter for the MoS_2 is 3.197 Å, which corresponds to fully relaxed structure, while all the strains necessary to have commensurate lattice parameters between the metal and MoS_2 are applied to the fcc-Au electrodes, under the assumption that this strain will not qualitatively alter the metal electrode transport properties. The cell was relaxed in z direction to optimize the distance

	Au (100)	Au (110)	Au (111)
a [Å]	4.156	4.156	4.156
Au unit cells	3x4x4	3x4x6	2x4x4
MoS_2 unit cells	4x3x1	4x2x1	3x2x1
Strain x [%]	-2.56	-2.56	5.79
Strain y [%]	0.08	5.79	5.79
c relaxed [Å]	4.209	3.001	7.736
d [Å]	8.054	7.826	8.647
Surface atoms	24	12	16
Area [nm^2]	1.279×1.661	1.279×1.107	0.959×1.107
Surface density [atoms/nm^2]	11.297	8.475	15.071

Table 8.1: Lattice parameters and structure information for Au-MoS_2-Au RRAM cells. In all cases the strain in Au surfaces was set to match with the fully relaxed lattice parameters of MoS_2 monolayer, corresponding to 3.197Å.

between the electrodes and the MoS_2 layer, and the Au c parameter, using a force and stress tolerance of 0.03 eVÅ and 0.1 GPa, respectively. The reciprocal space was sampled with a number of **k**-points equivalent to 24x24x24 per fcc unit cell with a single Au atom. Long-range van der Waals forces were included, using Grimme semi-empirical dispersion corrections [150].

The transport calculations were performed using NEGF formalism as described in Chapter 3. The setup for the calculations is shown in Figure 8.1.

8.2 Effect of MoS_2 phase and sulfur vacancies

In order to determine the origin of the resistance change observed in MoS_2-based RRAM cells, we performed transport calculations of MIM structures with pristine 2H and 1T'-MoS_2 layers, as well as, 2H-MoS_2 layers with single sulfur vacancies at different positions, sandwiched between two Au(100) electrodes. We chose the 100 surface because it has been observed in experimental cells through atomically resolved STM images [12].

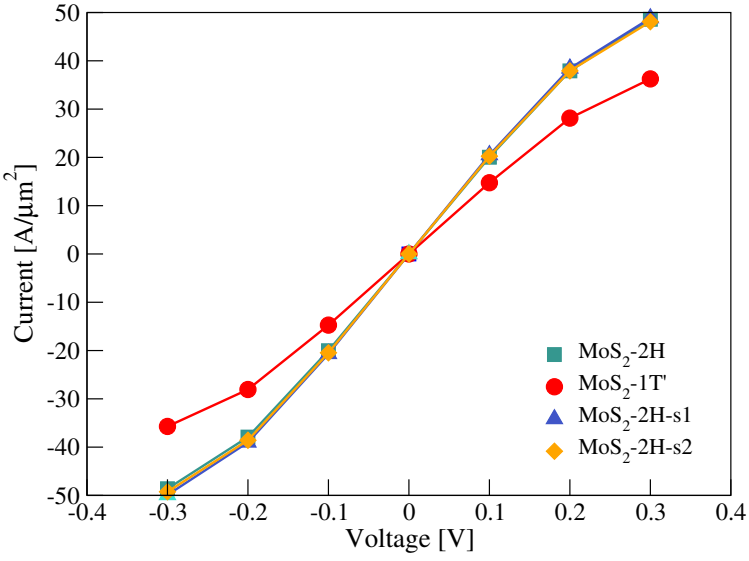

Figure 8.2: Current vs. voltage curves for MIM structures with different MoS_2 phases and defects.

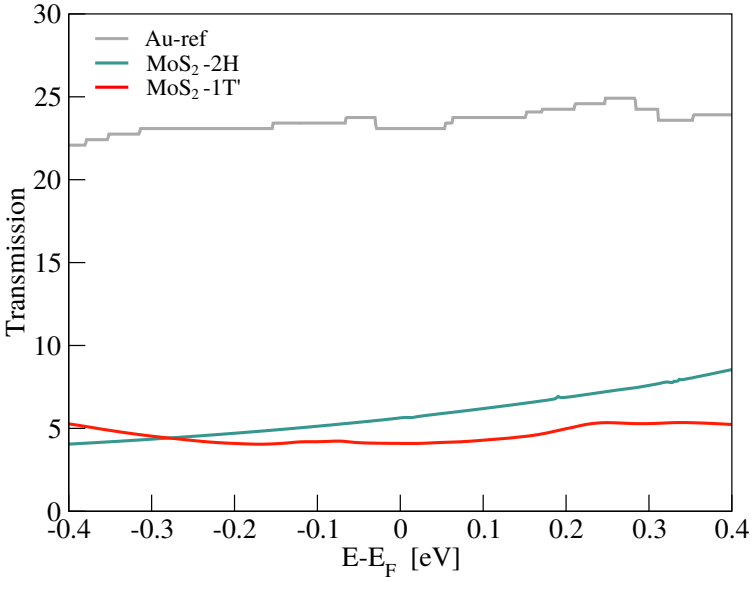

Figure 8.3: Transmission coefficients for Au(100)-MoS_2-Au(100) structures with different MoS_2 phases, compared with a reference Au(100) . the highest

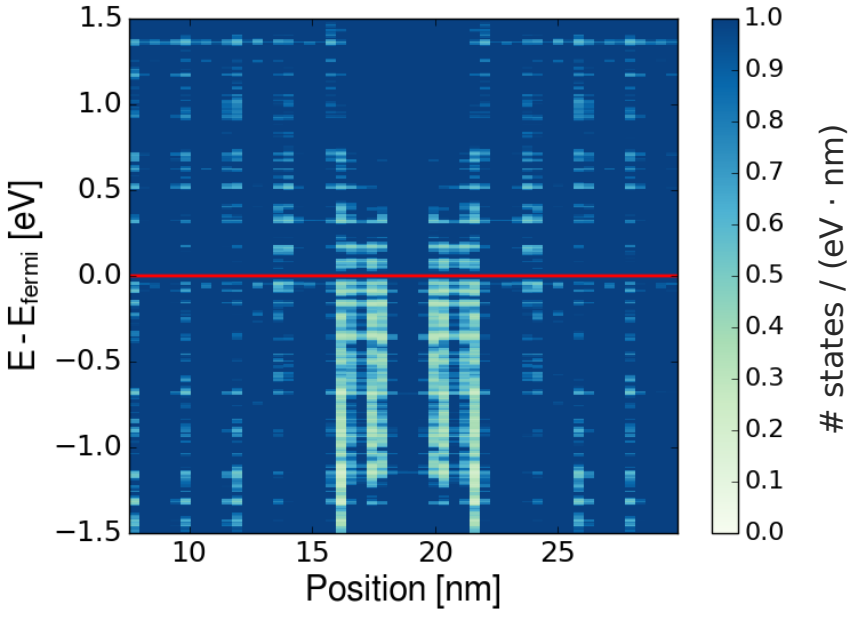

Figure 8.4: Energy-resolved local density of states (LDOS) of Au(100)/MoS_2(2H)/Au(100) structure. In the plot, the red and line denote the Fermi level. For clarity reasons, the scale bar was set to a maximum value of 1.0 $eV^{-1} \cdot nm^{-1}$.

The resulting current vs. voltage (I–V) curves are displayed in Figure 8.2, where it can be seen that both MoS_2 phases give similar results, and introducing vacancy defects does not affect the conductance at all. Besides, the extremely high current obtained in all cases are indicative of a LRS. Although these values are much higher than experimental results, the difference comes from the fact that our calculations are performed within a purely ballistic regime. Therefore, as far as the resulting conductance does not exceed the one predicted by the Landauer formula ($G_0 = \frac{2e^2}{h}T$), our result is reasonable. To verify this we analyzed the transmission coefficients for the MIM structures with pristine 2H and 1T'-MoS_2 phases and compared with reference bulk Au structures (without the active 2D layer nor vacuum), which provides the maximum attainable transmission. The results are shown in Figure 8.3, where it can be seen that the insertion of the MoS_2 layer results in a lowering of the coefficients only by a factor of $\sim$4.

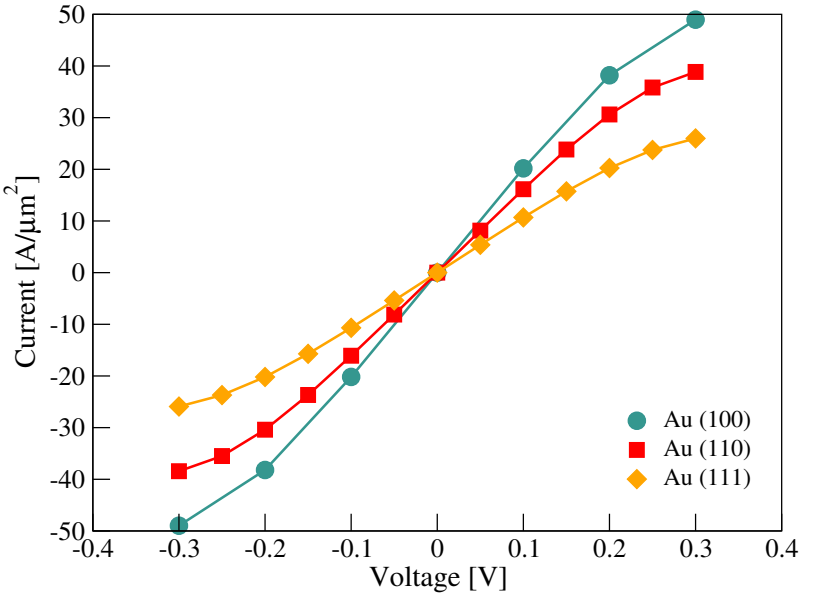

Figure 8.5: Current vs. voltage curves for MIM structures considering different Au surfaces

Since experiments have determined that current in HRS corresponds to Schottky emission, we plotted energy-resolved local density of states (LDOS), in order to extract the Schottky barriers heights, as shown in Figure 8.4. The 0.20 eV obtained for Au(100)/MoS_2(2H)/Au(100) structure is considerably lower than the 0.67 eV reported for Au-MoS_2 top contacts from DFT calculations considering vdW dispersion forces [56]. We speculate that the difference might be caused by changes in the band alignment due to the presence of a second Au electrodebellow.

As a result of the relatively low barrier height and the short barrier width of 0.81 nm (which is in good agreement with experimental value of 0.7 nm [12]), the structure shows strong tunneling transport.

8.3 Evaluation of different Au surfaces

In order to identify the structure corresponding to the HRS, we extended the transport studies to other Au surfaces [(110) and (111)], and the resulting I–V curves are displayed in Figure 8.5. Although there is a slight increase on the

resistance for (110) and (111) surfaces respect to the (100) surface, the values obtained still correspond to a LRS.

Notice that the changes in the conductance are related to two factors: i) the main one is the distance (d) between the two Au electrodes, and ii) the density of surface Au atoms also has some effect. Table 8.1 summarizes this information for each case. The (111) interface has the highest d, hence the lowest conductance; the (110) surface has the shortest d, but it has the lowest Au atom surface density, so it shows an intermediate conductance. Finally (100) would show the highest conductance because it has a large atomic surface density, and at the same time there is a short distance d.

8.4 Discussion and outlook

As a summary, transport calculations of Au/MoS_2/Au RRAM cells were performed in order to identify structural features responsible for LRS and HRS. The analysis of different phases of MoS_2, as well as sulfur defects in the 2H-MoS_2 layer demonstrated high current values, characteristic of a LRS. Besides, the evaluation of different contacting Au surfaces did not affect the conductance high enough to produce a switch in the resistance state. Therefore, we deduce that tunneling through the 2D layer dominates in all cases, and in order to observe HRS, structures with higher Schottky barriers must be considered.

The first step towards the understanding of the RS phenomena in 2D atomristors is the identification of structures with Schottky barriers high enough to limit electronic transport. Once this information is determined, the structural changes that give rise a reduction on the resistance can be addressed. Based on our results and the analysis of literature, we believe that some factors to be considered are:

- Include molybdenum vacancy defects, to determine whether there are changes in the band alignment and the Schottky barrier height increases.
- Study chromium contacts to evaluate the effect of this metal in the Schottky barrier formation. We propose Cr because several memristive devices based on 2D materials include an adhesion layer of approximately 2 nm between the Au electrode and the MoS_2 layer [12, 140, 143, 151].

- Contact the MoS_2 layer with different Au top and bottom surface orientations to reduce the coupling between electrode states.

Chapter 9

Conclusions

This thesis is focused on theoretical studies of 2D lateral metal-semiconducting interfaces and RRAM devices using non-equilibrium Green's functions, within density functional theory formalism and molecular dynamics simulations. The main contributions of this work are summarized in the following points:

- Transport properties of MoS_2 heterostructures were described in order to predict Schottky barriers, emission regimes and the contact resistances across metal/semiconductor interfaces.

- The analysis of current vs. voltage curves, as well as transmission coefficients, led us to a method for identifying emission regimes (i.e. tunnel vs. thermoionic) in Schottky contacts. The same analysis can be performed in experimental studies, prior to a possible use of the activation-energy method for the extraction of activation barriers.

- Molecular dynamics studies of RRAM devices conducted under an external field provided deep insights into the physics of the switching mechanism of filamentary HfO_2 based structures. In particular, the results indicate that reset/set processes take place by in plane oxygen atom diffusion as opposed to vertical diffusion.

- Through DFT combined with NEB calculations, it was possible to calculate formation energies and activation barriers involved in the migration of ions under external electric fields.

- The resistive switching phenomena was studied in MoS_2 single layers, sandwiched between Au electrodes, in order to determine the structural changes corresponding to high and low resistance states. The results demonstrate transport dominated by tunneling, indicative of LRS.

The work here presented may be extended by:

- Further analysis of the electrostatics in the lateral MoS_2 junctions: although the MoS_2 heterostructure transport studies were carried out with a large amount of vacuum between the periodic boundary condition replicas, the potential profile at distances from the interface larger than the vacuum separation might be influenced by the periodic replicas. This might be addressed with the use of a transport capable DFT code feturing a non-periodic Poisson solver.

- Further studies on the possibility of Fermi level pinning in lateral MoS_2 junctions by artificially doping the metallic (1T') phase, and subsequent Fermi level shifting on the metal side.

- Introducing a model for local Joule heating in the MD simulation of LRS RRAM devices, to better capture filament breakup in RESET events.

- Investigate the reason for the reduced lowering of the oxygen migration barrier under the action of an external electric field, by attempting a larger range of values.

- Exploring different configurations and electrode materials to elucidate the structure corresponding to the HRS in 2D-material based atomristors.

Bibliography

[1] W. H. Brattain, Bell Labs logbook (1947), pp. 7–8, 24.

[2] J. Bardeen and W. H. Brattain, "The Transistor, A Semi-Conductor Triode", Phys. Rev. **74**, 230 (1948).

[3] *International Roadmap for Devices and Systems 2020 Edition*, Tech. Rep. (IEEE).

[4] K. S. Novoselov, A. K. Geim, S. V. Morozov, D. Jiang, Y. Zhang, S. V. Dubonos, I. V. Grigorieva, and A. A. Firsov, "Electric Field Effect in Atomically Thin Carbon Films", Science **306**, 666 (2004).

[5] S. Z. Butler, S. M. Hollen, L. Cao, Y. Cui, J. A. Gupta, H. R. Gutiérrez, T. F. Heinz, S. S. Hong, J. Huang, A. F. Ismach, E. Johnston-Halperin, M. Kuno, V. V. Plashnitsa, R. D. Robinson, R. S. Ruoff, S. Salahuddin, J. Shan, L. Shi, M. G. Spencer, M. Terrones, W. Windl, and J. E. Goldberger, "Progress, Challenges, and Opportunities in Two-Dimensional Materials Beyond Graphene", ACS Nano **7**, 2898 (2013).

[6] P. Miró, M. Audiffred, and T. Heine, "An atlas of two-dimensional materials", Chem. Soc. Rev. **43**, 6537 (2014).

[7] J.-H. Chen, C. Jang, S. Xiao, M. Ishigami, and M. S. Fuhrer, "Intrinsic and extrinsic performance limits of graphene devices on SiO2", Nat. Nanotechnol. **3**, 206 (2008).

[8] C. R. Dean, A. F. Young, I. Meric, C. Lee, L. Wang, S. Sorgenfrei, K. Watanabe, T. Taniguchi, P. Kim, K. L. Shepard, and J. Hone, "Boron nitride

substrates for high-quality graphene electronics", Nat. Nanotechnol. **5**, 722 (2010).

[9] K. S. Novoselov, D. Jiang, F. Schedin, T. J. Booth, V. V. Khotkevich, S. V. Morozov, and A. K. Geim, "Two-dimensional atomic crystals", Proc. Natl. Acad. Sci. U.S.A. **102**, 10451 (2005).

[10] B. Radisavljevic, A. Radenovic, J. Brivio, V. Giacometti, and A. Kis, "Single-layer MoS_2 transistors", Nat. Nanotech. **6**, 147 (2011).

[11] S. Wachter, D. K. Polyushkin, O. Bethge, and M. Thomas, "A microprocessor based on a two-dimensional semiconductor", Nat. Commun **8**, 14948 (2017).

[12] R. Ge, X. Wu, M. Kim, J. Shi, S. Sonde, L. Tao, Y. Zhang, J. C. Lee, and D. Akinwande, "Atomristor: Nonvolatile Resistance Switching in Atomic Sheets of Transition Metal Dichalcogenides", Nano Lett. **18**, 434 (2018).

[13] D. Veksler, G. Bersuker, A. W. Bushmaker, P. R. Shrestha, K. P. Cheung, and J. P. Campbell, "Switching Variability Factors in Compliance-Free Metal Oxide RRAM", in *2019 IEEE International Reliability Physics Symposium (IRPS)* (2019) pp. 1–5.

[14] E. G. Marin, M. Perucchini, D. Marian, G. Iannaccone, and G. Fiori, "Modeling of Electron Devices Based on 2-D Materials", IEEE Trans. Electron Devices **65**, 4167 (2018).

[15] P. Hohenberg and W. Kohn, "Inhomogeneous Electron Gas", Phys. Rev. **136**, B864 (1964).

[16] W. Kohn and L. J. Sham, "Self-Consistent Equations Including Exchange and Correlation Effects", Phys. Rev. **140**, A1133 (1965).

[17] L. H. Thomas, "The calculation of atomic fields", Math. Proc. Camb. Philos. Soc. **23**, 542–548 (1927).

[18] E. Fermi, "Un Metodo Statistico per la Determinazione di alcune Prioprietà dell'Atomo", Rend. Accad. Naz. Lincei. **6**, 602 (1927).

[19] R. Martin, *Electronic Structure: Basic Theory and Practical Methods* (Cambridge University Press, 2004).

[20] E. Engel and R. Dreizler, *Density Functional Theory: An Advanced Course*, Theoretical and Mathematical Physics (Springer Berlin Heidelberg, 2011).

[21] C. Fiolhais, F. Nogueira, and M. A. L. Marques, *A Primer in Density Functional Theory*, Lecture Notes in Physics (Springer Berlin Heidelberg, 2003).

[22] A. D. Becke, "Perspective: Fifty years of density-functional theory in chemical physics", J. Chem. Phys. **140**, 18A301 (2014).

[23] M. Born and R. Oppenheimer, "Zur Quantentheorie der Molekeln", Ann. Phys. **389**, 457 (1927).

[24] J. P. Perdew, K. Burke, and M. Ernzerhof, "Generalized Gradient Approximation Made Simple", Phys. Rev. Lett. **77**, 3865 (1996).

[25] R. P. Feynman, "Forces in Molecules", Phys. Rev. **56**, 340 (1939).

[26] C. Kittel, *Introduction to Solid State Physics*, 8th ed. (John Wiley & Sons, 2004).

[27] G. Kresse and J. Furthmüller, "Efficiency of ab-initio total energy calculations for metals and semiconductors using a plane-wave basis set", Comput. Mater. Sci. **6**, 15 (1996).

[28] J. M. Soler, E. Artacho, J. D. Gale, A. García, J. Junquera, P. Ordejón, and D. Sánchez-Portal, "The SIESTA method for ab initio order-N materials simulation", J. Phys. Condens. Matter **14**, 2745 (2002).

[29] J. VandeVondele, M. Krack, F. Mohamed, M. Parrinello, T. Chassaing, and J. Hutter, "Quickstep: Fast and accurate density functional calculations using a mixed Gaussian and plane waves approach", Comput. Phys. Commun. **167**, 103 (2005).

[30] R. Landauer, "Electrical Resistance of Disordered One-Dimensional Lattices", Phil. Mag. **21**, 863 (1970).

[31] S. Datta, *Electronic Transport in Mesoscopic Systems*, Cambridge Studies in Semiconductor Physics and Microelectronic Engineering (Cambridge University Press, 1995).

[32] J. Cuevas and E. Scheer, *Molecular Electronics: An Introduction to Theory and Experiment*, World Scientific Series in Nanoscience and Nanotechnology (World Scientific, 2010).

[33] D. S. Fisher and P. A. Lee, "Relation between conductivity and transmission matrix", Phys. Rev. B **23**, 6851 (1981).

[34] J. E. Lennard-Jones, "Cohesion", Proc. Phys. Soc. **43**, 461 (1931).

[35] R. A. Buckingham, "The classical equation of state of gaseous helium, neon and argon", Proc. R. Soc. Lond. **168**, 264 (1938).

[36] G. V. Lewis and C. R. A. Catlow, "Potential models for ionic oxides", J. Phys. C: Solid State Phys. **18**, 1149 (1985).

[37] J. P. Trinastic, R. Hamdan, Y. Wu, L. Zhang, and H.-P. Cheng, "Unified interatomic potential and energy barrier distributions for amorphous oxides", J. Chem. Phys. **139**, 154506 (2013).

[38] S. J. Stuart, A. B. Tutein, and J. A. Harrison, "A reactive potential for hydrocarbons with intermolecular interactions", J. Chem. Phys. **112**, 6472 (2000).

[39] J. Tersoff, "Modeling solid-state chemistry: Interatomic potentials for multicomponent systems", Phys. Rev. B **39**, 5566 (1989).

[40] T. Iwasaki, "Molecular-Dynamics Analysis of Interfacial Diffusion Between High-Permittivity Gate Dielectrics And Silicon Substrates", J. Mater. Res. **19**, 1197–1202 (2004).

[41] T.-R. Shan, B. D. Devine, T. W. Kemper, S. B. Sinnott, and S. R. Phillpot, "Charge-optimized many-body potential for the hafnium/hafnium oxide system", Phys. Rev. B **81**, 125328 (2010).

[42] A. C. T. van Duin, S. Dasgupta, F. Lorant, and W. A. Goddard, "ReaxFF: A Reactive Force Field for Hydrocarbons", J. Phys. Chem. A **105**, 9396 (2001).

[43] N. Onofrio and A. Strachan, "Voltage equilibration for reactive atomistic simulations of electrochemical processes", J. Chem. Phys. **143**, 054109 (2015).

[44] G. O. A. Janssens, B. G. Baekelandt, H. Toufar, W. J. Mortier, and R. A. Schoonheydt, "Comparison of Cluster and Infinite Crystal Calculations on Zeolites with the Electronegativity Equalization Method (EEM)", J. Phys. Chem. **99**, 3251 (1995).

[45] W. J. Mortier, S. K. Ghosh, and S. Shankar, "Electronegativity-equalization method for the calculation of atomic charges in molecules", J. Am. Chem. Soc. **108**, 4315 (1986).

[46] F. H. Streitz and J. W. Mintmire, "Electrostatic potentials for metal-oxide surfaces and interfaces", Phys. Rev. B **50**, 11996 (1994).

[47] M. P. Allen and D. J. Tildesley, *Computer Simulation of Liquids* (Clarendon Press, USA, 1989).

[48] D. Frenkel and B. Smit, *Understanding Molecular Simulation*, second edition ed., edited by D. Frenkel and B. Smit (Academic Press, San Diego, 2002).

[49] S. Nosé, "A unified formulation of the constant temperature molecular dynamics methods", J. Chem. Phys. **81**, 511 (1984).

[50] W. G. Hoover, "Canonical dynamics: Equilibrium phase-space distributions", Phys. Rev. A **31**, 1695 (1985).

[51] Q. H. Wang, K. Kalantar-Zadeh, A. Kis, J. N. Coleman, and M. S. Strano, "Electronics and optoelectronics of two-dimensional transition metal dichalcogenides", Nat. Nanotech. **7**, 699 (2012).

[52] L. Gwan-Hyoung, Y. Young-Jun, C. Xu, P. Nicholas, L. Chul-Ho, C. Min Sup, L. Dae-Yeong, L. Changgu, Y. Won Jong, W. Kenji, T. Takashi,

N. Colin, K. Philip, and H. James, "Flexible and Transparent MoS_2 Field-Effect Transistors on Hexagonal Boron Nitride-Graphene Heterostructures", ACS Nano **7**, 7931 (2013).

[53] A. Allain, J. Kang, K. Banerjee, and A. Kis, "Electrical contacts to two-dimensional semiconductors", Nat. Mater. **14**, 1195 (2015).

[54] S. Das, H.-Y. Chen, A. V. Penumatcha, and J. Appenzeller, "High Performance Multilayer MoS2 Transistors with Scandium Contacts", Nano Lett. **13**, 100 (2013).

[55] S. Das, H.-Y. Chen, A. V. Penumatcha, and J. Appenzeller, "High-Performance Few-Layer-MoS_2 Field-Effect-Transistor with Record Low Contact-Resistance", IEDM , 499 (2013).

[56] J. Kang, W. Liu, D. Sarkar, D. Jena, and K. Banerjee, "Computational Study of Metal Contacts to Monolayer Transition-Metal Dichalcogenide Semiconductors", Phys. Rev. X **4**, 1 (2014).

[57] L. Yang, K. Majumdar, Y. Du, H. Liu, H. Wu, M. Hatzistergos, P. Hung, R. Tieckelmann, W. Tsai, C. Hobbs, and P. Ye, "High-Performance MoS_2 Field-Effect Transistors Enabled by Chloride Doping: Record Low Contact Resistance ($0.5\,\mathrm{k\Omega}\cdot{}^{-}\mathrm{m}$) and Record High Drain Current ($460\,\mu\mathrm{A}\cdot\mu\mathrm{m}$)" (2014) pp. 1–2.

[58] D. Voiry, A. Mohite, and M. Chhowalla, "Phase engineering of transition metal dichalcogenides", Chem. Soc. Rev. **44**, 2702 (2015).

[59] M. Calandra, "Chemically exfoliated single-layer MoS_2: Stability, lattice dynamics, and catalytic adsorption from first principles", Phys. Rev. B **88**, 245428 (2013).

[60] G. Gao, Y. Jiao, F. Ma, Y. Jiao, E. Waclawik, and A. Du, "Charge Mediated Semiconducting-to-Metallic Phase Transition in Molybdenum Disulfide Monolayer and Hydrogen Evolution Reaction in New 1T′ Phase", J. Phys. Chem. C **119**, 13124 (2015).

[61] X. Qian, J. Liu, L. Fu, and J. Li, "Quantum spin Hall effect in two-dimensional transition metal dichalcogenides", Science **346**, 1344 (2014).

[62] G. Eda, T. Fujita, H. Yamaguchi, D. Voiry, M. Chen, and M. Chhowalla, "Coherent Atomic and Electronic Heterostructures of Single-Layer MoS_2", ACS Nano **6**, 7311 (2012).

[63] Y.-C. Lin, D. O. Dumcenco, Y.-S. Huang, and K. Suenaga, "Atomic mechanism of the semiconducting-to-metallic phase transition in single-layered MoS_2", Nat. Nanotech. **9**, 391 (2014).

[64] R. Kappera, D. Voiry, S. E. Yalcin, B. Branch, G. Gupta, D. M. Aditya, and M. Chhowalla, "Phase-engineered low-resistance contacts for ultrathin MoS_2 transistors", Nat. Mater. **13**, 1128 (2014).

[65] N. Papior, N. Lorente, T. Frederiksen, A. García, and B. Mads, "Improvements on non-equilibrium and transport reen function techniques: The next-generation TRANSIESTA", Comput. Phys. Commun. **212**, 8 (2017).

[66] M. M. Ugeda, A. J. Bradley, S.-F. Shi, F. H. da Jornada, Y. Zhang, D. Y. Qiu, W. Ruan, S.-K. Mo, Z. Hussain, Z.-X. Shen, F. Wang, S. G. Louie, and M. F. Crommie, "Giant bandgap renormalization and excitonic effects in a monolayer transition metal dichalcogenide semiconductor", Nat. Mater. **13**, 1091 (2014).

[67] G. P. Das, P. Blöchl, O. K. Andersen, N. E. Christensen, and O. Gunnarsson, "Electronic structure and Schottky-barrier heights of (111) $NiSi_2$/Si A- and B-type interfaces", Phys. Rev. Lett. **63**, 1168 (1989).

[68] N. Troullier and J. L. Martins, "Efficient pseudopotentials for plane-wave calculations", Phys. Rev. B **43**, 1993 (1991).

[69] D. Stradi, U. Martinez, A. Blom, M. Brandbyge, and K. Stokbro, "General atomistic approach for modeling metal-semiconductor interfaces using density functional theory and nonequilibrium Green's function", Phys. Rev. B **93**, 155302 (2016).

[70] J.-T. Lü, R. B. Christensen, G. Foti, T. Frederiksen, T. Gunst, and M. Brandbyge, "Efficient calculation of inelastic vibration signals in electron transport: Beyond the wide-band approximation", Phys. Rev. B **89**, 081405 (2014).

[71] N. Papior, T. Gunst, D. Stradi, and M. Brandbyge, "Manipulating the voltage drop in graphene nanojunctions using a gate potentia", Phys. Chem. Chem. Phys **18**, 1025 (2016).

[72] F. A. Padovani and R. Stratton, "Field and thermionic-field emission in Schottky barriers", Sol. Stat. Electron. **9**, 695 (1966).

[73] S. M. Sze and K. K. Ng., *Physics of semiconductor devices* (John Wiley & Sons, Ltd, 2006).

[74] X. Li, R. Grassi, S. Li, T. Li, X. Xiong, T. Low, and Y. Wu, "Anomalous Temperature Dependence in Metal–Black Phosphorus Contact", Nano Lett. **18**, 26 (2018).

[75] L. D. N. Mouafo, F. Godel, G. Froehlicher, S. Berciaud, B. Doudin, M. Venkata Kamalakar, and J.-F. Dayen, "Tuning contact transport mechanisms in bilayer $MoSe_2$ transistors up to Fowler–Nordheim regime", 2D Mater. **4**, 015037 (2016).

[76] N. Ankur, J. Sirisha, B. Abhinandan, and T. James T., "Electrostatics of lateral p-n junctions in atomically thin materials", J. Appl. Phys. **122**, 194501 (2017).

[77] F. A. Padovani, "The Voltage-Current Characteristic of Metal-Semiconductor Contacts", in *Semiconductors and Semimetals*, Vol. 7, edited by R. K. Willardson and A. C. Beer (Academic Press, Inc., New York, 1971) pp. 75–146.

[78] Y. S. Ang, H. Y. Yang, and L. K. Ang, "Universal Scaling Laws in Schottky Heterostructures Based on Two-Dimensional Materials", Phys. Rev. Lett. **121**, 056802 (2018).

[79] D. Saha and S. Mahapatra, "Asymmetric Junctions in Metallic–Semiconducting–Metallic Heterophase MoS_2", IEEE Trans. Electron Dev. **64**, 2457 (2017).

[80] R. T. Tung, "The physics and chemistry of the Schottky barrier height", Appl. Phys. Rev. **1**, 011304 (2014).

[81] H. Yang, J. Heo, S. Park, H. J. Song, D. H. Seo, K.-E. Byun, P. Kim, I. Yoo, H.-J. Chung, and K. Kim, "Graphene Barristor, a Triode Device with a Gate-Controlled Schottky Barrier", Science **336**, 1140 (2012).

[82] Y. Katagiri, T. Nakamura, A. Ishii, C. Ohata, M. Hasegawa, S. Katsumoto, T. Cusati, A. Fortunelli, G. Iannaccone, G. Fiori, S. Roche, and J. Haruyama, "Gate-Tunable Atomically Thin Lateral MoS_2 Schottky Junction Patterned by Electron Beam", Nano Lett. **16**, 3788 (2016).

[83] Y. Guo, D. Liu, and J. Robertson, "3D Behavior of Schottky Barriers of 2D Transition-Metal Dichalcogenides", ACS Appl. Mater. Interfaces **7**, 25709 (2015).

[84] C. Gong, L. Colombo, R. M. Wallace, and K. Cho, "The Unusual Mechanism of Partial Fermi Level Pinning at Metal-MoS_2 Interfaces", Nano Lett. **14**, 1714 (2014).

[85] C. Kim, I. Moon, D. Lee, M. S. Choi, F. Ahmed, S. Nam, Y. Cho, H.-J. Shin, S. Park, and W. J. Yoo, "Fermi Level Pinning at Electrical Metal Contacts of Monolayer Molybdenum Dichalcogenides", ACS Nano **11**, 1588 (2017).

[86] S. Nakaharai, M. Yamamoto, K. Ueno, and K. Tsukagoshi, "Carrier Polarity Control in α-$MoTe_2$ Schottky Junctions Based on Weak Fermi-Level Pinning", ACS Appl. Mater. Interfaces **8**, 14732 (2016).

[87] M. Houssa, K. Iordanidou, A. Dabral, A. Lu, G. Pourtois, V. Afanasiev, and A. Stesmans, "Contact Resistance at MoS_2-Based 2D Metal/Semiconductor Lateral Heterojunctions", ACS Appl. Nano Mater. **2**, 760 (2019).

[88] A. Nourbakhsh, A. Zubair, R. N. Sajjad, A. Tavakkoli K. G., W. Chen, S. Fang, X. Ling, J. Kong, M. S. Dresselhaus, E. Kaxiras, K. K. Berggren, D. Antoniadis, and T. Palacios, "MoS_2 Field-Effect Transistor with Sub-10 nm Channel Length", Nano Lett. **16**, 7798 (2016).

[89] B. Govoreanu, G. S. Kar, Y. Chen, V. Paraschiv, S. Kubicek, A. Fantini, I. P. Radu, L. Goux, S. Clima, R. Degraeve, N. Jossart, O. Richard, T. Vandeweyer, K. Seo, P. Hendrickx, G. Pourtois, H. Bender, L. Altimime, D. J.

Wouters, J. A. Kittl, and M. Jurczak, "10x10nm^2 Hf/HfOx crossbar resistive RAM with excellent performance, reliability and low-energy operation", in *2011 International Electron Devices Meeting* (2011) pp. 31.6.1–31.6.4.

[90] H. Y. Lee, P. S. Chen, T. Y. Wu, Y. S. Chen, C. C. Wang, P. J. Tzeng, C. H. Lin, F. Chen, C. H. Lien, and M. . Tsai, "Low power and high speed bipolar switching with a thin reactive Ti buffer layer in robust HfO2 based RRAM", in *2008 IEEE International Electron Devices Meeting* (2008) pp. 1–4.

[91] Y. C. Yang, F. Pan, Q. Liu, M. Liu, and F. Zeng, "Fully Room-Temperature-Fabricated Nonvolatile Resistive Memory for Ultrafast and High-Density Memory Application", Nano Lett. **9**, 1636 (2009).

[92] R. Waser, R. Dittmann, G. Staikov, and K. Szot, "Redox-Based Resistive Switching Memories – Nanoionic Mechanisms, Prospects, and Challenges", Adv. Mater. **21**, 2632 (2009).

[93] U. Celano, L. Goux, R. Degraeve, A. Fantini, O. Richard, H. Bender, M. Jurczak, and W. Vandervorst, "Imaging the Three-Dimensional Conductive Channel in Filamentary-Based Oxide Resistive Switching Memory", Nano Lett. **15**, 7970 (2015).

[94] S. Privitera, G. Bersuker, B. Butcher, A. Kalantarian, S. Lombardo, C. Bongiorno, R. Geer, D. Gilmer, and P. Kirsch, "Microscopy study of the conductive filament in HfO2 resistive switching memory devices", Microelectron. Eng. **109**, 75 (2013).

[95] B. Traoré, P. Blaise, E. Vianello, L. Perniola, B. De Salvo, and Y. Nishi, "HfO2-Based RRAM: Electrode Effects, Ti/HfO2 Interface, Charge Injection, and Oxygen (O) Defects Diffusion Through Experiment and Ab Initio Calculations", IEEE Trans. Electron Devices **63**, 360 (2016).

[96] A. Kindsmüller, A. Meledin, J. Mayer, R. Waser, and D. J. Wouters, "On the role of the metal oxide/reactive electrode interface during the forming procedure of valence change ReRAM devices", Nanoscale **11**, 18201 (2019).

[97] W. He, H. Sun, Y. Zhou, K. Lu, K. Xue, and X. Miao, "Customized binary and multi-level HfO_{2-x}-based memristors tuned by oxidation conditions", Sci. Rep. **7**, 10070 (2017).

[98] Y. Y. Chen, L. Goux, S. Clima, B. Govoreanu, R. Degraeve, G. S. Kar, A. Fantini, G. Groeseneken, D. J. Wouters, and M. Jurczak, "Endurance/Retention Trade-off on HfO_2/Metal Cap 1T1R Bipolar RRAM", IEEE Trans. Electron Devices **60**, 1114 (2013).

[99] S. Plimpton, "Fast Parallel Algorithms for Short-Range Molecular Dynamics", J. Comp. Phys. **117**, 1 (1995).

[100] M. Parrinello and A. Rahman, "Polymorphic transitions in single crystals: A new molecular dynamics method", J. Appl. Phys. **52**, 7182 (1981).

[101] L. C. Gallington, Y. Ghadar, L. B. Skinner, J. K. R. Weber, S. V. Ushakov, A. Navrotsky, A. Vazquez-Mayagoitia, J. C. Neuefeind, M. Stan, J. J. Low, and C. J. Benmore, "The Structure of Liquid and Amorphous Hafnia", Mater. (Basel, Switzerland) **10**, 10.3390/ma10111290 (2017).

[102] T.-J. Chen and C.-L. Kuo, "First principles study of the oxygen vacancy formation and the induced defect states in hafnium silicates", J. Appl. Phys. **111**, 074106 (2012).

[103] M. P. Mueller and R. A. De Souza, "SIMS study of oxygen diffusion in monoclinic HfO2", Appl. Phys. Lett. **112**, 051908 (2018).

[104] G. Broglia, G. Ori, L. Larcher, and M. Montorsi, "Molecular dynamics simulation of amorphous HfO2for resistive RAM applications", Model. Simul. Mater. Sci. Eng. **22**, 065006 (2014).

[105] S. R. Bradley, A. L. Shluger, and G. Bersuker, "Electron-Injection-Assisted Generation of Oxygen Vacancies in Monoclinic HfO_2", Phys. Rev. Appl. **4**, 064008 (2015).

[106] A. S. Foster, F. Lopez Gejo, A. L. Shluger, and R. M. Nieminen, "Vacancy and interstitial defects in hafnia", Phys. Rev. B **65**, 174117 (2002).

[107] J. X. Zheng, G. Ceder, T. Maxisch, W. K. Chim, and W. K. Choi, "First-principles study of native point defects in hafnia and zirconia", Phys. Rev. B **75**, 104112 (2007).

[108] X. Cartoixà, R. Rurali, and J. Suñé, "Transport properties of oxygen vacancy filaments in metal/crystalline or amorphous HfO_2/metal structures", Phys. Rev. B **86**, 165445 (2012).

[109] S. U. Sharath, T. Bertaud, J. Kurian, E. Hildebrandt, C. Walczyk, P. Calka, P. Zaumseil, M. Sowinska, D. Walczyk, A. Gloskovskii, T. Schroeder, and L. Alff, "Towards forming-free resistive switching in oxygen engineered HfO_2", Appl. Phys. Lett. **104**, 063502 (2014).

[110] M. Sowinska, T. Bertaud, D. Walczyk, S. Thiess, M. A. Schubert, M. Lukosius, W. Drube, C. Walczyk, and T. Schroeder, "Hard x-ray photoelectron spectroscopy study of the electroforming in Ti/HfO2-based resistive switching structures", Appl. Phys. Lett. **100**, 233509 (2012).

[111] W. Humphrey, A. Dalke, and K. Schulten, "VMD: Visual molecular dynamics", J. Mol. Graph. **14**, 33 (1996).

[112] J. Stone, An Efficient Library for Parallel Ray Tracing and Animation, Master's thesis, Computer Science Department, University of Missouri-Rolla (1998).

[113] A. O'Hara, G. Bersuker, and A. A. Demkov, "Assessing hafnium on hafnia as an oxygen getter", J. Appl. Phys. **115**, 183703 (2014).

[114] S. Menzel, U. Böttger, M. Wimmer, and M. Salinga, "Physics of the Switching Kinetics in Resistive Memories", Adv. Funct. Mater. **25**, 6306 (2015).

[115] F. Pan, S. Gao, C. Chen, C. Song, and F. Zeng, "Recent progress in resistive random access memories: Materials, switching mechanisms, and performance", Mater. Sci. Eng. R Rep. **83**, 1 (2014).

[116] S. Long, X. Lian, C. Cagli, X. Cartoixà, R. Rurali, E. Miranda, D. Jiménez, L. Perniola, M. Liu, and J. Suñé, "Quantum-size effects in hafnium-oxide resistive switching", Appl. Phys. Lett. **102**, 183505 (2013).

[117] S. Menzel and R. Waser, *Advances in Non-Volatile Memory and Storage Technology (Second Edition)*, second edition ed., edited by B. Magyari-Köpe and Y. Nishi, Woodhead Publishing Series in Electronic and Optical Materials (Woodhead Publishing, 2019) pp. 137 – 170.

[118] M. Schie, S. Menzel, J. Robertson, R. Waser, and R. A. De Souza, "Field-enhanced route to generating anti-Frenkel pairs in HfO_2", Phys. Rev. Mater. **2**, 035002 (2018).

[119] D. S. Jeong, H. Schroeder, and R. Waser, "Coexistence of Bipolar and Unipolar Resistive Switching Behaviors in a $Pt/TiO_2/Pt$ Stack", Electrochem. Solid-State Lett. **10**, G51 (2007).

[120] J. X. Zheng, G. Ceder, T. Maxisch, W. K. Chim, and W. K. Choi, "First-principles study of native point defects in hafnia and zirconia", Phys. Rev. B **75**, 104112 (2007).

[121] A. S. Foster, F. Lopez Gejo, A. L. Shluger, and R. M. Nieminen, "Vacancy and interstitial defects in hafnia", Phys. Rev. B **65**, 174117 (2002).

[122] Y. Dai, Z. Pan, F. Wang, and X. Li, "Oxygen vacancy effects in HfO2-based resistive switching memory: First principle study", AIP Adv. **6**, 085209 (2016).

[123] R. Öttking, S. Kupke, E. Nadimi, R. Leitsmann, F. Lazarevic, P. Plänitz, G. Roll, S. Slesazeck, M. Trentzsch, and T. Mikolajick, "Defect generation and activation processes in HfO2 thin films: Contributions to stress-induced leakage currents", phys. stat. sol. (a) **212**, 547 (2015).

[124] N. Capron, P. Broqvist, and A. Pasquarello, "Migration of oxygen vacancy in HfO_2 and across the HfO_2/SiO_2 interface: A first-principles investigation", Appl. Phys. Lett. **91**, 192905 (2007).

[125] C. Tang and R. Ramprasad, "Point defect chemistry in amorphous HfO_2: Density functional theory calculations", Phys. Rev. B **81**, 161201 (2010).

[126] G. Makov and M. C. Payne, "Periodic boundary conditions in ab initio calculations", Phys. Rev. B **51**, 4014 (1995).

[127] J. Neugebauer and M. Scheffler, "Adsorbate-substrate and adsorbate-adsorbate interactions of Na and K adlayers on Al(111)", Phys. Rev. B **46**, 16067 (1992).

[128] A.-M. El-Sayed, M. B. Watkins, T. Grasser, and A. L. Shluger, "Effect of electric field on migration of defects in oxides: Vacancies and interstitials in bulk MgO", Phys. Rev. B **98**, 064102 (2018).

[129] J. W. Strand, J. Cottom, L. Larcher, and A. L. Shluger, "Effect of electric field on defect generation and migration in HfO_2", Phys. Rev. B **102**, 014106 (2020).

[130] N. Salles, L. Martin-Samos, S. de Gironcoli, L. Giacomazzi, M. Valant, A. Hemeryck, P. Blaise, B. Sklenard, and N. Richard, "Collective dipole effects in ionic transport under electric fields", Nat. Commun. **11**, 3330 (2020).

[131] S. H. Jeon, W.-J. Son, B. H. Park, and S. Han, "Multiscale simulation on electromigration of the oxygen vacancies in metal oxides", Appl. Phys. A **102**, 909 (2011).

[132] J. VandeVondele and J. Hutter, "Gaussian basis sets for accurate calculations on molecular systems in gas and condensed phases", J. Chem. Phys. **127**, 114105 (2007).

[133] H. Jonsson, G. Mills, and K. W. Jacobsen, "Nudged elastic band method for finding minimum energy paths of transitions", in *Classical and Quantum Dynamics in Condensed Phase Simulations*, pp. 385–404.

[134] G. Henkelman and H. Jónsson, "Improved tangent estimate in the nudged elastic band method for finding minimum energy paths and saddle points", J. Chem. Phys. **113**, 9978 (2000).

[135] G. Henkelman, B. P. Uberuaga, and H. Jónsson, "A climbing image nudged elastic band method for finding saddle points and minimum energy paths", J. Chem. Phys. **113**, 9901 (2000).

[136] W. Klopper, C. C. M. Samson, G. Tarczay, and A. G. Császár, "Equilibrium inversion barrier of NH3 from extrapolated coupled-cluster pair energies", J. Comput. Chem. **22**, 1306 (2001).

[137] J. D. Swalen and J. A. Ibers, "Potential Function for the Inversion of Ammonia", J. Chem. Phys. **36**, 1914 (1962).

[138] R. Rurali and X. Cartoixà, "Theory of Defects in One-Dimensional Systems: Application to Al-Catalyzed Si Nanowires", Nano Lett. **9**, 975 (2009).

[139] M. C. Cheynet, S. Pokrant, F. D. Tichelaar, and J.-L. Rouvière, "Crystal structure and band gap determination of HfO2 thin films", J. Appl. Phys. **101**, 054101 (2007).

[140] M. Kim, R. Ge, X. Wu, X. Lan, J. Tice, J. C. Lee, and D. Akinwande, "Zero-static power radio-frequency switches based on MoS2 atomristors", Nat. Commun. **9**, 2524 (2018).

[141] P. Cheng, K. Sun, and Y. H. Hu, "Memristive Behavior and Ideal Memristor of 1T Phase MoS2 Nanosheets", Nano Letters **16**, 572 (2016).

[142] R. Xu, H. Jang, M.-H. Lee, D. Amanov, Y. Cho, H. Kim, S. Park, H.-j. Shin, and D. Ham, "Vertical MoS2 Double-Layer Memristor with Electrochemical Metallization as an Atomic-Scale Synapse with Switching Thresholds Approaching 100 mV", Nano Letters **19**, 2411 (2019).

[143] X. Wu, R. Ge, P.-A. Chen, H. Chou, Z. Zhang, Y. Zhang, S. Banerjee, M.-H. Chiang, J. C. Lee, and D. Akinwande, "Thinnest Nonvolatile Memory Based on Monolayer h-BN", Advanced Materials **31**, 1806790 (2019).

[144] L. Zhang, T. Gong, H. Wang, Z. Guo, and H. Zhang, "Memristive devices based on emerging two-dimensional materials beyond graphene", Nanoscale **11**, 12413 (2019).

[145] V. K. Sangwan, D. Jariwala, I. S. Kim, K.-S. Chen, T. J. Marks, L. J. Lauhon, and M. C. Hersam, "Gate-tunable memristive phenomena mediated by grain boundaries in single-layer MoS2", Nat. Nanotechnol. **10**, 403 (2015).

[146] V. K. Sangwan, H.-S. Lee, H. Bergeron, I. Balla, M. E. Beck, K.-S. Chen, and M. C. Hersam, "Multi-terminal memtransistors from polycrystalline monolayer molybdenum disulfide", Nature **554**, 500 (2018).

[147] A. A. Bessonov, M. N. Kirikova, D. I. Petukhov, M. Allen, T. Ryhänen, and M. J. A. Bailey, "Layered memristive and memcapacitive switches for printable electronics", Nat. Mater. **14**, 199 (2015).

[148] M. Wang, S. Cai, C. Pan, C. Wang, X. Lian, Y. Zhuo, K. Xu, T. Cao, X. Pan, B. Wang, S.-J. Liang, J. J. Yang, P. Wang, and F. Miao, "Robust memristors based on layered two-dimensional materials", Nature Electronics **1**, 130 (2018).

[149] S. M. Hus, R. Ge, P.-A. Chen, L. Liang, G. E. Donnelly, W. Ko, F. Huang, M.-H. Chiang, A.-P. Li, and D. Akinwande, "Observation of single-defect memristor in an MoS2 atomic sheet", Nat. Nanotechnol. 10.1038/s41565-020-00789-w (2020).

[150] S. Grimme, "Semiempirical GGA-type density functional constructed with a long-range dispersion correction", J. Comput. Chem. **27**, 1787 (2006).

[151] L. Yin, R. Cheng, Z. Wang, F. Wang, M. G. Sendeku, Y. Wen, X. Zhan, and J. He, "Two-Dimensional Unipolar Memristors with Logic and Memory Functions", Nano Lett. **20**, 4144 (2020).